ROTARY BED REACTOR FOR CHEMICAL-LOOPING COMBUSTION WITH CARBON CAPTURE

By
ZHENLONG ZHAO
B.S. COLLEGE OF ENGINEERING
PEKING UNIVERSITY, BEIJING (2010)

SUBMITTED TO THE DEPARTMENT OF MECHANICAL ENGINEERING IN PARTIAL FULFILLMENT OF THE REQUIREMENTS FOR THE DEGREE OF

MASTER OF SCIENCE IN MECHANICAL ENGINEERING
AT THE
MASSACHUSETTS INSTITUTE OF TECHNOLOGY

JUNE 2012

Signature of Author: _____
Department of Mechanical Engineering
May 31, 2012

Certified by: _____
Prof. Ahmed F. Ghoniem – Thesis Supervisor
Ronald C. Crane (1972) Professor of Mechanical Engineering

Accepted by: _____
David E. Hardt
Chairman, Department Committee on Graduate Students

Page left intentionally blank

ROTARY BED REACTOR FOR CHEMICAL-LOOPING COMBUSTION WITH CARBON CAPTURE

By Zhenlong Zhao

Submitted to the Department of Mechanical Engineering on May 31, 2012 in partial fulfillment of the requirements for the degree of Master of Science in Mechanical Engineering

Abstract

Chemical-looping combustion (CLC) is a novel and promising technology for power generation with inherent CO_2 capture. Currently almost all the research has been focused on developing CLC based inter-connected fluidized bed reactors. A new rotating reactor concept for gas fueled CLC is proposed. In the reactor, a solid wheel rotates between the fuel and the air streams at the reactor inlet and exit. Two purging sectors are used to avoid the mixing between the fuel stream and the air stream. The rotating wheel consists of a large number of channels with copper oxide coated on the inner surface of the channels. The support material is boron nitride which has high specific heat and thermal conductivity. Gas flows through the reactor at elevated pressure and it is heated from 823K to 1245K by fuel combustion. The rotary reactor design for a thermal capacity of 1MW has been performed using a simplified model that was developed to predict the performances of the reactor. Preliminary analysis shows that both the fuel conversion efficiency and the carbon separation efficiency are close to unity. The wheel temperature flucatuation is small. There is great potential for further improvement of the construction and operating conditions, which will be followed up in the future.

Thesis Supervisor: Ahmed F. Ghoniem

Title: Ronald C. Crane (1972) Professor of Mechanical Engineering

Page left intentionally blank

Acknowledgements

I would like to express my sincere thanks to Professor Ghoniem, my supervisor, who gave me the opportunity to work on such an interesting project and provided me with all the necessary support. His excellent technical advices, encouraging discussions and valuable times are highly appreciated. His sensible and professional approach made this study challenging and enjoyable.

I am also grateful to my colleagues in RGD, Lei Chen, Guang Wu, Patrick Kirchen, Tianjiao Chen, Simcha Singer, Richard Bates, Cristina Botero, etc. for providing essential information and support whenever I needed.

I am truly thankful for the friends I have from all the places I have lived. To my teachers and mentors from MIT, I thank them for their generosity and for developing a drive in me to make a difference.

Most of all, I appreciate the love and support of my family. They have been with me every step of the way.

Page left intentionally blank

TABLE OF CONTENTS

List of Figures

List of Tables

Nomenclature

Symbols

A	cross-sectional area
a	pressure coefficient
C_i	concentration of species i
D	reactor diameter
D_a	effective diffusivity
d	size of particle, or channel side
E_a	activation energy
E_g, E_s	energy of gas or solid
f	drag coefficient
H	channel length
H_g	enthalpy of gas
h_{gs}	heat transfer coefficient between phases
$J_{g,j}$	diffusive mass flux
K_p	equilibrium constant
k, k_p	reaction rate constant
k_s	thermal conductivity of solid phase
k_0	pre-exponential factor
$h_{m,i}$	external mass transfer coefficient
m_{ox}	mass of fully oxidized oxygen carrier
m_{red}	mass of fully reduced oxygen carrier
n	reaction order
P	operating pressure
P_c	inner perimeter of the channel
$p_{i,out}$	partial pressure of species i
Q_{gs}	heat flux from gas phase to solid phase
R_o	oxygen capacity
Re_d	Reynolds number
R_u	gas universal constant

$\dot{r}$	reaction rate
T	temperature
u	velocity
$\dot{W}$	work
X	conversion of oxygen carrier
X_i	molar fraction of species i

Greek letters

β_B	drag force coefficient
δ_{bulk}	thickness of the bulk support layer
δ_{oc}	thickness of the porous oxygen carrier layer
δ_{s}	thickness of the solid phase (including the porous layer and the bulk layer)
ε_i	volume fraction of phase (or species) i
ε_s	porosity of the solid
γ	conversion yield of fuels
η_e	thermal efficiency for only electricity generation
η_{H2}	thermal efficiency for only hydrogen generation
η_{II}	second law efficiency
η_{th}	thermal efficiency for power generation
μ_g	viscosity of gas
ν	stoichiometric coefficient
θ_i	size of sector i
ρ	density
$\hat{\rho}$	molar density
τ	cyclic period time
$\boldsymbol{\tau}_i$	stress tensor of phase i
ω	overall molar reaction rate

Acronyms

AR	air reactor
BN	boron nitride

CC	combined cycle
CCS	carbon capture and sequestration
CFzB	circulating fluidized-bed reactors
CLC	chemical-looping combustion
CP	co-precipitation
CSIC	Instituto de Carboquı´mica
DCFB	dual circulating fluidized bed
DI	dry impregnation, incipient wet impregnation
DM	dissolution method
DP	deposition-precipitation
FG	freeze-granulation
FR	fuel reactor
FxB	fixed-bed reactors
FzB	fluidized-bed reactors
IGCC	integrated gasification combined cycle
MM	mechanical-mixing
MvB	moving-bed reactors
NG	natural gas
OC	oxygen carrier
PcB	packed-bed reactors
RoB	rotating bed reactor
SCL	syngas chemical looping
SD	spray-drying
SG	sol-gel
SOFC/GC	solid oxide fuel cell/gas turbine
TGA	thermo-gravimetric analyzer
TIT	turbine inlet temperature
WI	wet impregnation
YSZ	yttria-stabilized zirconia

Page left intentionally blank

Chapter 1

Introduction

1.1 Carbon Capture Technologies

During the last decade, significant progress has been made towards a better understanding of the world climate and of the long-term impact of climate change. More and more evidence showed that the mean annual temperature at the earth's surface increased over the past 200 years [1]. It has been widely acknowledged that emission of greenhouse gases is the main contributor to global warming, and CO_2 is the most prevalent of these gas emissions. Statistics [1] showed that the concentration of atmospheric CO_2 increased from a pre-industrial level of 280 ppm to the current level of 380 ppm due to human reactivity. Thus, the CO_2 emission control is critical to the mitigation of global climate change.

Currently, combustion of fossil fuels provides around 80% of primary energy production [2]. This releases a massive amount of carbon dioxide into the atmosphere. The main source of CO_2 emissions fossil fuels combustion is from large fossil- or biomass fueled power plants, cement- and steel industries, refineries and natural gas processing facilities. These account for nearly 60% of the global CO_2 emissions [3]. Power generation accounts for over one-third of the overall emissions [4]. Thus it is necessary to control the CO_2 emissions from power generation.

One possible approach to reducing CO_2 emissions is to expand the utilization of alternative energy, such as solar energy, hydro-energy, wind energy, nuclear energy, biomass energy, etc. However, due to current technology limitation and infrastructure, in the near term, these renewable energy sources cannot replace fossil fuel power generation completely. Technology options that allow for the continuing utilization of fossil fuels with substantial carbon capture and sequestration (CCS) would be desirable.

Technologies for capturing CO_2 from combustion in power plants can be divided into three main categories: post-combustion capture, pre-combustion capture, and oxy-fuel combustion. In post-combustion capture, CO_2 is separated from the nitrogen rich flue gases after normal combustion. A chemical sorbent would normally be used to accomplish this. The method

used today is scrubbing the flue gases using an amine solution [5]. The advantage of post-treatment is that the CO_2 separation equipment can be added to an existing plant without significant modifications of the system.

Pre-combustion capture refers to decarbonization of the fuel by producing hydrogen. Oxygen and/or steam are used to convert fuel to a synthesis gas of carbon monoxide and hydrogen. The carbon monoxide is then reacted with steam in a catalytic reactor to generate CO_2 and additional hydrogen. Next, CO_2 is separated, usually by a physical or chemical absorption process, resulting in a hydrogen-rich fuel which can be used in many applications. The major drawback of this process is that the equipment for pre-combustion capture is rather complex and expensive. However, the hydrogen produced in this way can be directly used in a wide range of applications.

Oxy-fuel combustion is based on a combustion process using pure oxygen instead of air to obtain a flue gas stream containing mostly CO_2 and H_2O, where the water can easily be removed by condensation. Part of the flue gas needs to be recycled into the combustion chamber, in order to control the flame temperature [5]. Compared to post- or pre-combustion captures, oxy-fuel combustion can achieve almost complete carbon separation. However, the separation of oxygen from nitrogen prior to combustion is an energy demanding step.

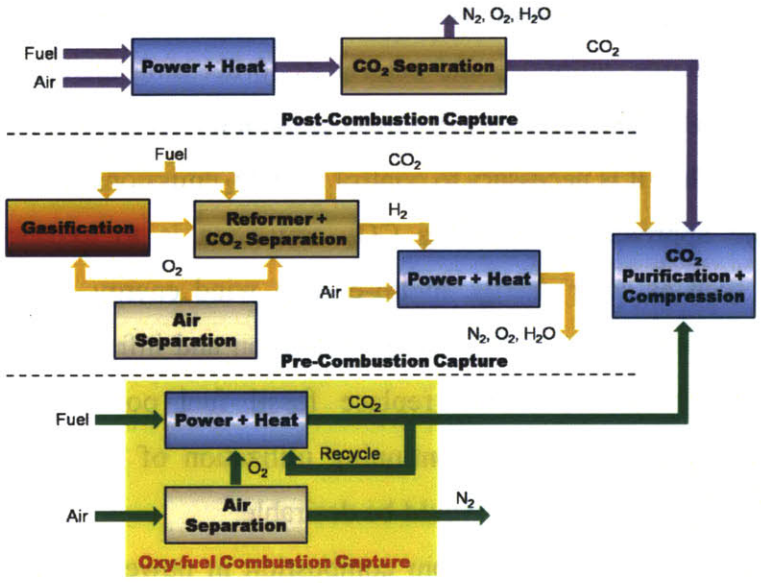

Figure 1-1 A comparison of three carbon capture technologies.

A preliminary comparison between these three carbon capture procedures is shown in

Figure 1-1. The overall plant efficiency of nine carbon capture concepts from the three categories described above are compared in Figure 1-2, in which the technology availability decreases from left to right [6]. As seen in Figure 1-2, with complete CO_2 capture, the efficiency of pre-combustion capture is up to 50% when membrane H_2 separation method is used, while post-combustion capture can only reach an efficiency of 48%. Solid oxide fuel cell method could offer as high as 67% conversion efficiency. However, this method remains an experimental concept and it's still far from large-scale application.

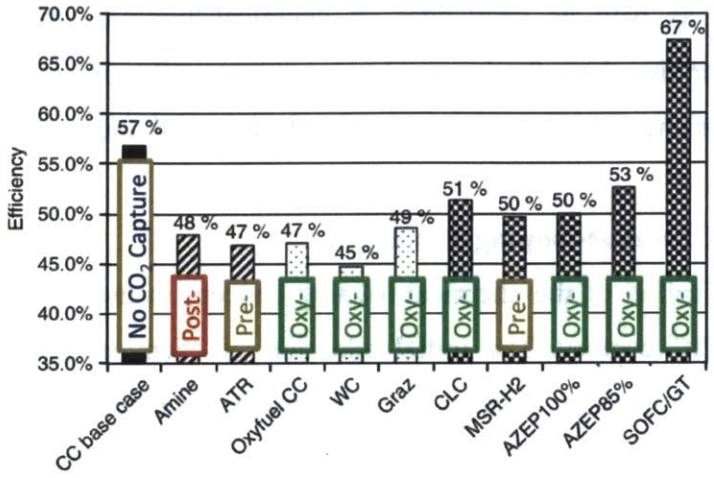

Figure 1-2 Net plant efficiency of the nine concepts and a CC concept in % of fuel LHV [6].
ATR: auto-thermal reforming; WC: water cycle; CLC: chemical looping combustion; MSR-H2: membrane H_2 separation; AZEP: advanced zero emission process (ion transport membrane) 100% CO_2 capture, 85% CO_2 capture; SOFC/GC: solid oxide fuel cell/gas turbine

Chemical-looping combustion (CLC) belongs to the oxy-fuel combustion category, in which pure oxygen rather than air is supplied by a metal oxide for combustion such that the mixing between CO_2 and N_2 in the combustion flue gas is inherently avoided. CLC is also referred to as unmixed-combustion. As seen in Figure 1-2, the efficiency of CLC is 51%, higher than any pre- or post-combustion CCS method. A complete carbon conversion can be achieved when CLC is used for CCS. In addition, since CLC prototypes with power output up to 145kW and over 4000 operation hours have already been reported in the literature (detailed review is presented in Section 2.2), this method is more feasible than SOFC/GC method.

Considering the potential efficiency enhancement compared to current available CCS technologies, experiment work has been carried out towards characterizing CLC, including looping material testing, reactor design, cyclic process analysis of CLC integrated with gas/steam

turbines. Previous studies have reviewed the preliminary experimental results of various looping media [7-9], the development of various pilot-scale prototypes [9, 10] as well as the process design with extension of chemical-looping concept to coal-gasification or steam-reforming processes [11]. While successful, CLC technology still faces many challenges from different aspects, e.g. desirable materials with high oxygen capacity, fast reactivity, and robust regenerability; optimized reactor system design with high efficiency, good commercial feasibility and compatibility with current power plants as well as limited risk of failures. In this work, the current development as well as challenges of chemical-looping combustion is thoroughly reviewed. By understanding these fundamental processes as well as the intrinsic complexities, an alternative solution for chemical-looping combustion is proposed and examined.

1.2 Brief History of Chemical-looping Strategy

The first application of the chemical-looping concept in industry may date back to the late 19th and early 20th century. The initial adoption of chemical-looping strategy was not concerned with climate change. Instead, it was mainly prompted by the lack of effective chemical conversion/separation techniques in the generation of products. For instance, Howard Lane designed and commercialized the steam-iron process for hydrogen production by reducing syngas using iron oxide as an intermediate based on the following reaction scheme: [11, 12]

$$Fe_3O_4(s) + 4CO(g) \text{ (or } H_2(g)) \rightarrow 3Fe(s) + 4CO_2(g) \text{ (or } H_2O(g)) \quad (1.1)$$

$$3Fe(s) + 4H_2O(g) \rightarrow 4H_2(g) + Fe_3O_4(s) \quad (1.2)$$

However, this steam-iron process only partially converts the syngas. Moreover, the iron-based looping medium has poor recyclability, especially in the presence of sulfur [11]. Therefore, it was gradually replaced by less costly hydrogen production methods using oil and natural gas as feedstock (steam reforming, partial oxidation, etc).

In 1954, chemical looping was proposed in a patent by Lewis and Gilliland from Massachusetts Institute of Technology to produce pure CO_2 for the beverage industry [13]. The Lewis and Gilliland CO_2 production process made use of two inter-connected fluidized-bed reactors with copper- or iron-oxides as looping medium, as seen in Figure 1-3. Solid fuel is converted by metal oxides into CO_2 and steam in the CO_2 generator and air is used to regenerate the metal oxides. This has been widely acknowledged as the first application of chemical-looping strategy. Alternative reactor designs, e.g. moving beds, or fixed beds, were also considered by

Lewis and Gilliland.

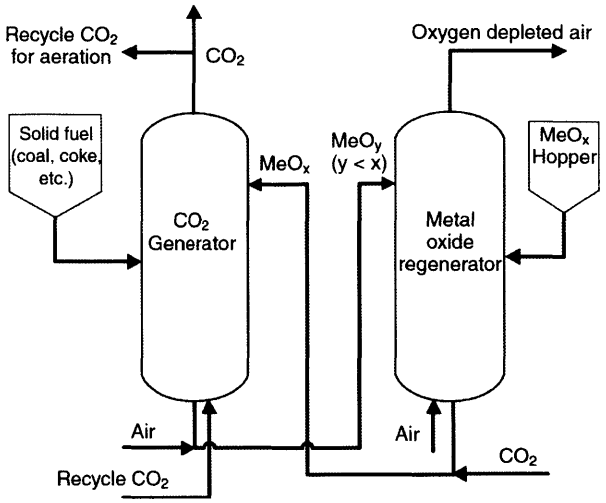

Figure 1-3 Schematic representation of Lewis and Gilliland CO_2 production process [13]

In 1980s, the name "chemical-looping" was proposed by Richter and Knoche [14, 15] for the first time, although the application of chemical-looping strategy was proposed far earlier. The research by Richter and Knoche was prompted by the need to increase the reversibility of combustion processes and therefore increase the thermal efficiency of power plants [14, 15]. The idea was to supply low-temperature heat to the endothermic reaction in the fuel reactor, thereby increasing the amount of heat produced in the high-temperature air reactor. However, at that time, this technology did not attract much attention because of the high costs associated with the inter-connected two-reactor system.

In 1994, Ishida and Jin [16] suggested that chemical-looping combustion could be used as a way to separate and thus capture CO_2 in a power plant. Since then, the developments of chemical-looping technology have focused on the chemical-looping combustion of carbonaceous fuels (e.g., natural gas, syngas, petroleum coke, coal, and biomass), in which the CO_2 is separated inherently. With growing interests in environmental issues and the impact of greenhouse gas emissions on climate change, the inherent CO_2 separation that CLC offers has drawn more and more attention such that it has been acknowledged as one of the most promising carbon capture techniques.

Since the beginning of the 21st century, research on chemical-looping combustion has grown exponentially with more and more research institutes all over the world playing important roles in facilitating CLC development. Among them, Chalmers University of Technology in

Sweden, Instituto de Carboquı´mica (CSIC) in Spain, Vienna University of Technology in Austria, Korean Institute of Energy Research in Korea, and Southeast University in China have designed and successfully operated different sub-pilot scale prototypes using gaseous or solid fuels to illustrate the behaviors of this promising technology. The successful applications in these demonstrations are expected to lead to a wider commercial deployment of CLC.

1.3 Chemical-looping Combustion

Chemical-looping combustion is an unmixed combustion process. Combustion is split into two reactions: reduction and oxidation. Hence, the system is composed of two reactors, an air reactor (AR) and a fuel reactor (FR), as seen in Figure 1-4. Fuel is introduced in the fuel reactor, which contains metal oxide, Me_xO_y. The fuel and the metal oxide react according to reaction:

$$(2n+m)\ Me_xO_y + C_nH_{2m} \rightarrow (2n+m)\ Me_xO_{y-1} + mH_2O + nCO_2 \qquad (1.3)$$

The exit gas stream contains only CO_2 and water. After condensation of water, pure CO_2 can be obtained.

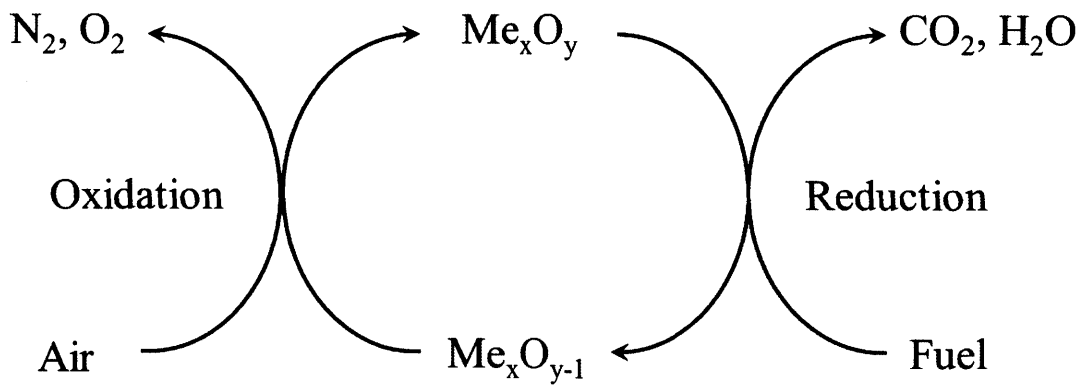

Figure 1-4 Schematic representation of the chemical-looping combustion process.

The reduced metal oxide, Me_xO_{y-1}, is then transferred into the air reactor where it is oxidized. The oxidation reaction is according to:

$$Me_xO_{y-1} + \text{air} \rightarrow Me_xO_y + N_2 + \textit{unreacted}\ O_2 \qquad (1.4)$$

The outlet gas stream of the air reactor contains nitrogen and unreacted oxygen.

The reduction is often endothermic if methane is used, and always exothermic if syngas is used. The oxidation reaction is always highly exothermic. The heats of reaction depend on fuel

type and on the metal oxide used as OC, and it can be calculated using classic thermodynamics analysis (as seen in Section 2.1). The summation of energy released from these two reactions gives exactly the same amount as the direct combustion:

$$C_nH_{2m} + \text{air} \rightarrow mH_2O + nCO_2 + N_2 + \textit{unreacted}\ O_2 \qquad (1.5)$$

Although there is no net enthalpy gain from chemical looping combustion, it has several merits over conventional combustion:

- *Complete combustion in the fuel reactor produces CO_2 and water vapor only. Therefore CO_2 is captured simply by condensing water, reducing the need of an additional energy intensive process of CO_2 separation as in post-combustion capture or fuel de-carbonization as in pre-combustion capture.*

- *The outlet gas stream of the air reactor contains nitrogen and unreacted oxygen. Since the fuel burns in the fuel reactor in an air free environment and the reduced OC is re-oxidized in the air reactor in the absence of a fuel, at comparatively low temperatures, CLC also minimizes NO_x formation. NO_x formation usually occurs well above 1200°C which is potentially the maximum temperature for CLC.*

- *Exergy analysis shows that it is theoretically possible to achieve a higher efficiency of energy conversion through strategic energy management using CLC [17, 18]. This is mainly due to three reasons:* (i) *CLC could reduce the exergy destruction within combustion as compared to conventional direct combustion since the reaction occurs close to the equilibrium temperature;* (ii) *CLC could incorporate the integration of two stages of combustion, which could favor a better energy utilization through proper management; and* (iii) *CLC could minimize the exergy loss associated with heat transfer since the operating temperature range of 800-1200°C is close to the current power generation cycles, and thus the large temperature difference and hence large irreversibility work loss in the heat exchanger for the conventional power generation cycles could be avoided.*

The inherent CO_2 separation makes CLC one of the most attractive technology for CCS, and almost all the current research has been mainly focused on this aspect. Hence the global process optimization and strategic energy management study which concentrate on the

enhancement of the operation efficiency will be the next-step research in the future.

1.4 Research Objective

The objective of this thesis is to review the development and challenges related to chemical-looping combustion and propose a new rotary design. A comprehensive review of the state of the art of chemical-looping combustion is carried out, covering experimental work on oxygen carriers, reactor design and prototype construction as well as the numerical tools for modeling and optimization. By understanding these fundamental processes as well as the intrinsic challenges associated with the chemical-looping combustion, an alternative rotary design concept is proposed. The novel rotary reactor could be able to make the most of the chemical-looping concept to create intrinsically separated reactions and hence capture the carbon dioxide, but avoid the multi-phase, multi-scale complexities associated with the conventional chemical-looping reactor designs. The approach to modeling focuses on the periodic state considering the thermal, chemical, and physical performances in repeated cycles. The preliminary analysis can then inform the feasibility of the rotary reactor designs and operation.

1.5 Outline of the Thesis

The thesis is broken into six chapters. Chapter 2 provides a comprehensive literature review of the chemical-looping combustion. This chapter is broken into three main sections. The first section discussed the oxygen carrier preparation methods, and the important results obtained from thermodynamics analysis as well as from experiments. Next, various reactor candidates are illustrated and prototypes are introduced. Lastly, the three levels of modeling for CLC are reviewed following the sequence of particle modeling, reactor simulation and cyclic process analysis.

Chapter 3 proposes the concept of the novel reactor based on the rotary bed reactor. In addition to describing the reactor design, functionality, it also details the selection criteria for the operating conditions. The advantages as well as potential issues associated with the design are also discussed.

Chapter 4 details the development, assumptions, and framework of the simplified model. The model mainly focuses on the one dimensional periodic performances of the reactor. Models are implemented and validated with respect to analytical results.

Chapter 5 discusses the results from the modeling. The feasibility of the rotary reactor is discussed based on the preliminary analysis from the simplified model, and recommendations for reactor design and operating conditions are made.

Chapter 6 presents conclusions and recommendations for the future work in the detailed modeling as well as experimental work for the rotary reactor.

Page left intentionally blank

Chapter 2

Literature Review

2.1 Oxygen Carriers

The looping medium in chemical-looping combustion absorbs oxygen from air in the air reactor and releases oxygen in the fuel reactor. It acts as an "oxygen carrier" (OC) to transport oxygen while it is looping between reactors. Thus it is often referred to as the oxygen carrier in the literature. Since first proposed by Richter and Knoche in 1983 [14], the selection of the OC has been acknowledged as one of the most important aspects in chemical-looping combustion. The characteristics of OCs determine the size and configuration of the reactors, bed inventory, power output, pre-, post-CLC processing, the overall cyclic efficiency and the economic cost. Most of the work on CLC so far has been focused on the development and investigation of OCs configured in particle form using fixed or fluidized bed reactors. Basic criteria for a good candidate of an OC have been acknowledged as follows [7, 9, 11, 19]:

1) *Reactivity*: Reactivity measures the reaction kinetics of chemical-looping combustion. OCs selected for chemical-looping combustion should exhibit high reactivity in both the reduction and oxidation cycles. Higher reactivity means shorter residence time, smaller reactor and hence lower capital cost. The reactivity depends greatly on the type of metal oxides, and it is a function of the preparation method, support materials, promoters, as well as reaction conditions.

2) *Oxygen capacity*: The oxygen capacity describes the maximum amount of oxygen that can be transferred with the looping medium. A higher oxygen-carrying capacity gives rise to a high thermal capacity of the reactor. Oxygen capacity of the looping oxygen carrier is mainly determined by the properties of the metal oxides and the extent of support materials used for preparation.

3) *Conversion of fuels:* Conversion of fuels reflects the ability of OCs to convert fuel to products. High conversion means high energy utilization efficiency. The conversion of fuels

is restricted primarily by the thermodynamics equilibrium of the fuel and the OC. In addition, it can also be affected by the fuel and particle residence time, reactor design, as well as solid-gas contact patterns.

4) *Selectivity*: Selectivity measures the reaction affinities. Some OCs have high selectivity to complete combustion products, i.e. CO_2, H_2O, while some might be selective towards CO, or H_2. For chemical-looping combustion, it is desirable to use OCs with high selectivity to complete combustion products while for reforming it is desirable to use OC with high selectivity towards CO or H_2.

5) *Physical properties matching*: The OCs should exhibit desirable physical characteristics matching the reactor system. This includes the heat of reaction, either endothermic or exothermic, matching the reactor heat balance, the density, size and the conductivity with operation compatible with the operation regimes, the mechanical strength and the melting temperature being high enough for the operating pressures and temperatures.

6) *Stability*: Stability means that the operation of chemical-looping combustion be continuous and stable. This requires the OC to circulate continuously in the reactors without significant changes in the behaviors (criteria as listed from 1 to 5). Furthermore, OCs should be resistant to agglomeration, attrition, as well as contaminant species and carbon formation, especially if the fuel has some impurity. Stability directly determines the maintenance costs of commercial application.

7) *Costs & safety*: The cost of raw material is critical for the commercialization of chemical-looping combustion. This means that the raw material should be abundant in nature; the fabrication procedures should be feasible for large-scale operations. Besides, the safety issues should also be considered since for large scale application, a large quantity of oxygen carrier needs to be disposed of. Therefore, OCs with low health and environment impacts are desirable.

Some of the above selection criteria of OCs may be contradictory. For example, an OC with higher reactivity is often more expensive; good stability of particles often means a higher extent of support material, and harder and less porous structure, and thus lower reactivity and lower oxygen capacity. Thus, the selection of the optimum OCs should depend on the specific design of the reactor and the CLC system, and it is a trade-off between capital and maintenance

costs.

2.1.1 Thermodynamics Analysis

Thermodynamics analysis is the first step for the analysis of potential OC candidates. The results obtained using thermodynamics analysis can provide theoretical support and guide for experiment. Lyngfelt and Mattisson in 2001 [19] were among the first to give a brief report on screening a small group of OC candidates based on thermodynamics analysis. They suggested that NiO/Ni, CuO/Cu_2O, Fe_2O_3 and Mn_3O_4/MnO are good candidates since almost complete conversion can be obtained with high equivalent constants. Later, a more comprehensive analysis was carried out by Jerndal et al. [20] in which 27 OC systems for CLC were analyzed, including Ni-, Cu-, Fe-, Cd-, Mn-, Co-, Zn-, Ce-, W-based oxides, and Ba-, Sr, and Ca-based sulphates. Twelve groups of these were concluded to be good candidates for CLC with the consideration of fuel conversion, decomposition, melting point, carbon formation and sulfur formation: NiO/Ni, CuO/Cu, Cu_2O/Cu, Fe_2O_3/Fe_3O_4, Mn_2O_3/MnO, Mn_3O_4/MnO, Co_3O_4/Co, CoO/Co, $WO_3/WO_{2.722}$, $BaSO_4/BaS$. $SrSO_4/SrS$, $CaSO_4/CaS$. As will be seen in Section 2.1.3 and in Appendix A, six of them have been tested extensively by various research groups: NiO/Ni, CuO/Cu, Fe_2O_3/Fe_3O_4, Mn_3O_4/MnO, Co_3O_4/Co, $CaSO_4/CaS$. The thermodynamics analysis of the above six OC systems [19, 20] was summarized in this section.

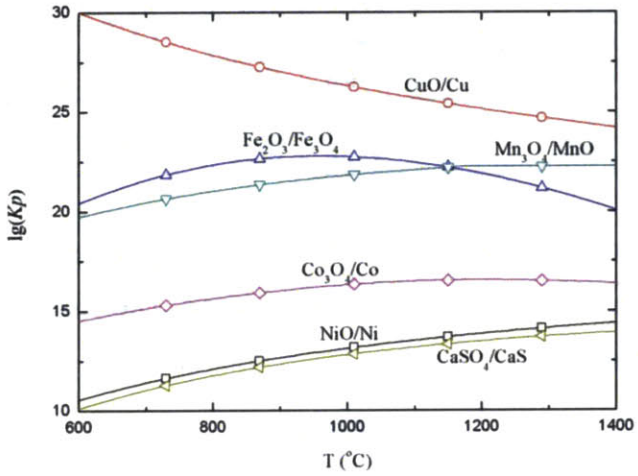

Figure 2-1 The equilibrium constant (K_p) of CH_4 oxidation reaction as a function of temperature (per mole CH_4)

Table 2-1 Properties of the twelve most promising oxygen carriers

Oxygen carrier	γ_{H2}(800/1000/1200°C)	γ_{CO}(800/1000/1200°C)	γ_{CH4}(800/1000/1200°C)	melt point (°C)	R_0
NiO/Ni	0.9946/0.9931/0.9915	0.9949/0.9883/0.9788	0.9949/0.9883/0.9788	1955/1455	0.2142
CuO/Cu	1.0000/1.0000/0.9999	1.0000/1.0000/0.9997	1.0000/1.0000/0.9997	1446/1085	0.2011
Cu_2O/Cu	1.0000/0.9999/0.9998	1.0000/0.9999/0.9996	1.0000/0.9999/0.9996	1235/1085	0.1118
Fe_2O_3/Fe_3O_4	1.0000/1.0000/0.9999	1.0000/1.0000/0.9997	1.0000/1.0000/0.9997	1565/1597	0.0334
Mn_2O_3/MnO	1.0000/1.0000/0.9999	1.0000/1.0000/0.9997	1.0000/1.0000/0.9997	1347[1)]/1842	0.1013
Mn_3O_4/MnO	1.0000/1.0000/0.9999	1.0000/0.9999/0.9997	1.0000/0.9999/0.9997	1562/1842	0.0699
Co_3O_4/Co	0.9993/0.9989/0.9984	0.9993/0.9981/0.9959	0.9993/0.9981/0.9959	895[2)]/1496	0.0664
CoO/Co	0.9674/0.9574/0.9486	0.9691/0.9299/0.8793	0.9691/0.9299/0.8793	1830/1496	0.2135
$CaSO_4$/CaS	0.9921/0.9902/0.9881	0.9925/0.9835/0.9704	0.9925/0.9835/0.9704	1460/2525	0.4701

[1)] Mn_2O_3 will generally decompose into Mn_3O_4 around 900°C. [2)] Co_3O_4 will decompose into CoO at this temperature.

Table 2-2 Properties of twelve oxidation reactions at 1000°C

Oxidation reaction	ΔH_o(kJ)	lg(K)	$\Delta H_o/\Delta H_{CH4}$	$\Delta H_o/\Delta H_{H2}$	$\Delta H_o/\Delta H_{CO}$
$O_2(g) + 0.5CH_4(g) = 0.5CO_2(g) + H_2O(g)$	-401.7	16.41	1.00	-	-
$O_2(g) + 2H_2(g) = 2H_2O(g)$	-498.5	14.57	-	1.00	-
$O_2(g) + 2CO(g) = 2CO_2(g)$	-562.9	14.11	-	-	1.00
$O_2(g) + 2Ni = 2NiO$	-468.5	10.26	1.17	0.94	0.83
$O_2(g) + 2Cu = 2CuO$	-295.9	3.58	0.74	0.59	0.53
$O_2(g) + 4Cu = 2Cu_2O$	-331.7	6.25	0.83	0.67	0.59
$O_2(g) + 4Fe_3O_4 = 6Fe_2O_3$	-478.8	4.29	1.19	0.96	0.85
$O_2(g) + 4MnO = 2Mn_2O_3$	-359.1	3.85	0.89	0.72	0.64
$O_2(g) + 6MnO = 2Mn_3O_4$	-449.4	6.03	1.12	0.90	0.80
$O_2(g) + 1.5Co = 0.5Co_3O_4$	-446.8	8.69	1.11	0.90	0.79
$O_2(g) + 2Co = 2CoO$	-466.9	11.86	1.16	0.94	0.83
$O_2(g) + 0.5CaS = 0.5CaSO_4$	-471.0	10.56	1.17	0.94	0.84

In thermodynamic analysis, equilibrium conversion yield is a good indicator to measure the maximum conversion of fuels that the OC can achieve. The conversion yields of fuels, γ_{CH4}, γ_{CO}, γ_{H2}, are defined as follows:

$$\gamma_{CH_4} = \frac{p_{CO_2,out}}{p_{CH_4,out} + p_{CO_2,out}} \tag{2.1}$$

$$\gamma_{CO} = \frac{p_{CO_2,out}}{p_{CO_2,out} + p_{CO,out}} \tag{2.2}$$

$$\gamma_{H_2} = \frac{p_{H_2O,out}}{p_{H_2,out} + p_{H_2O,out}} \tag{2.3}$$

where $p_{i,out}$ is the partial pressure of species i (CO_2, CH_4, CO, H_2O, H_2). The conversion yields are zero when no fuel is converted and unity when fuel is completely oxidized.

In general, the maximum (equilibrium) conversion yields can be obtained by minimizing Gibbs free energy of the system. One simpler way to illustrate this concept is to use the thermodynamic equilibrium constant as a function of temperature. Take hydrogen oxidation as an example, the equilibrium reaction of metal oxide with H_2 can be written as:

$$Me_xO_y(s) + H_2(g) \leftrightarrow Me_xO_{y-1}(s) + H_2O(g) \tag{2.4}$$

The equilibrium constant is defined as:

$$K_p = \exp\left[-\frac{\hat{g}^o_{Me_xO_{y-1}(s)} + \hat{g}^o_{H_2O(g)} - \hat{g}^o_{Me_xO_y(s)} - \hat{g}^o_{H_2(g)}}{R_u T}\right] = \frac{(p_{H_2O}/p^o)^1}{(p_{H_2}/p^o)^1} = \frac{\gamma_{H_2}}{1-\gamma_{H_2}} \tag{2.5}$$

The equilibrium constant measures the reaction affinity with a high K_p value indicating a high potential to fully convert the fuel into products and thus a high conversion yield ($\gamma \sim 1$). Equilibrium constants of reductions with CH_4, and equilibrium conversion yields of CH_4, CO, H_2 at different temperatures are shown in Figure 2-1 and in Table 2-1, respectively. For comparison, Cu_2O/Cu, Mn_2O_3/MnO and CoO/Co are also included in Table 2-1. The results in Figure 2-1 and in Table 2-1 were obtained using ASPEN PLUS 7.1. One assumption made is that all substances in the solid phase are in pure form. Further, CO_2, H_2O and O_2 are also included as gaseous components. For Ca-based sulphate, no decomposition is assumed in the calculation. However, if decomposition is considered, the conversion yields will decrease and SO_x will exist in flue gas.

As seen in Table 2-1, Cu-, Fe-, and Mn-based OCs have almost complete conversion of fuels at all three temperatures while the rest have lower conversions but still above 0.97, except for CoO/Co. In general, the conversion of hydrogen is higher than that of methane or carbon monoxide. Besides, for all the OC groups, the conversion decreases as the temperature increases due to the thermal decomposition of CO_2 and H_2O at high temperatures.

Figure 2-1 shows that for these six OCs, when temperature increases from 800°C to 1200°C, almost constant or slightly lower equilibrium constant K_p is maintained at relatively high values (10^{10}) for methane. Similar results are obtained for hydrogen or carbon monoxide. Thus, for a temperature range between 800°C to 1200°C, almost complete combustion can be

expected. This suggests that CLC can be operated with a temperature range much lower than the adiabatic flame temperature of fuels (e.g. 2175°C for hydrogen, and 1993°C for methane) and much closer to the current operation temperatures of gas turbine (around 1200°C).

In a chemical-looping system, agglomeration may occur when materials become soft at temperatures approaching their melting points. Therefore, it is advantageous to operate CLC below this temperature. As seen in Table 2-1, only copper has the disadvantage of a comparably low melting temperature of 1085°C, which is within a commonly suggested operating temperature range from 800°C to 1200°C. Therefore, agglomeration may occur for copper-based OCs when particles are exposed to high temperatures. For Co_3O_4/Co as OC pair, at temperatures above 900°C, Co_3O_4 will decompose into CoO, which has relatively lower conversion yield. This decomposition temperature is generally too low for CLC to be efficient. Therefore, Cobalt-based oxides cannot be used directly as OCs. However, cobalt can be combined with other metal oxide to be good OC candidate. For Mn_2O_3/MnO, it may also decompose into its reduced form (Mn_3O_4) at about 900°C. However, Mn_3O_4/MnO has good reactivity as well as conversion yield, which makes it a promising candidate for CLC.

The oxygen capacity R_o in Table 2-1 is calculated according to:

$$R_o = (m_{ox} - m_{red}) / m_{ox} \tag{2.6}$$

where m_{ox}, m_{red} is the mass of fully oxidized, and fully reduced oxygen carrier. The oxygen capacity is the theoretical maximum mass fraction of the OC which can be used in the oxygen transfer between the fuel and air reactors. From Table 2-1, we can see that $CaSO_4$ has the highest R_o, while NiO, CuO have similar oxygen capacities. Although iron oxide has very high oxygen mass fraction, the oxygen capacity of iron-based OC is very low because only Fe_2O_3/Fe_3O_4 pair has the ability to fully convert the fuel. It should be noted that oxygen capacity decreases when an inert material is used as binder.

The reaction enthalpies and reaction constants of oxidation reactions at 1000°C are shown in Table 2-2. For comparison, the ratio of oxidation reaction enthalpies to that of conventional direct combustion is also included. Because the overall heat released from CLC is the same as that from normal combustion, it is possible to determine whether the reduction reactions in the fuel reactor are endothermic or exothermic from this ratio. A ratio above 1 means that the reduction is endothermic and below 1 indicates exothermic. As seen in Table 2-2, for the temperature of 1000°C, reductions are always exothermic when hydrogen or carbon monoxide is

used while they are endothermic for most OCs when methane is used. An endothermic fuel reactor reaction requires extra consideration of energy balance between reactors for CLC system design.

2.1.2 Preparation

Pure metals show poor reactivity, conversion or regenerability. Figure 2-2 shows one cycle conversion profile of NiO with/without binder as OC ([21]) and Figure 2-3 shows the regenerability of CuO with/without binder as OC through seven cycles ([22]). As can be seen in Figure 2-2, both the reduction and oxidation rates of pure NiO are lower than those prepared with binder. Furthermore, the oxidation conversion of reduced pure Ni can only achieve 30% in 15 min while for $NiO/NiAl_2O_4$, oxidation is almost complete in 6 min. As seen in the Figure 2-3, oxidation reaction rate of pure CuO decreases quickly with increasing the number of cycles and after three cycles of reaction the reactivity of the extrudates is extremely low, reaching conversions of only 10%. However, for CuO supported by SiO_2, no significant change is observed throughout the seven cycles, and at the same time the reaction rate is about one order of magnitude faster than pure CuO. The large difference in behavior with or without binder is due to the fact that the OC may sinter at high temperature and this prevents further reaction inside oxygen carriers. In addition, the accumulative thermal and chemical stresses of the OCs lead to progressive performance decay and mechanical degradation with the number of cycles. Similar results can be found for other metal oxides (Mn_3O_4, Fe_2O_3, Co_3O_4, etc.).

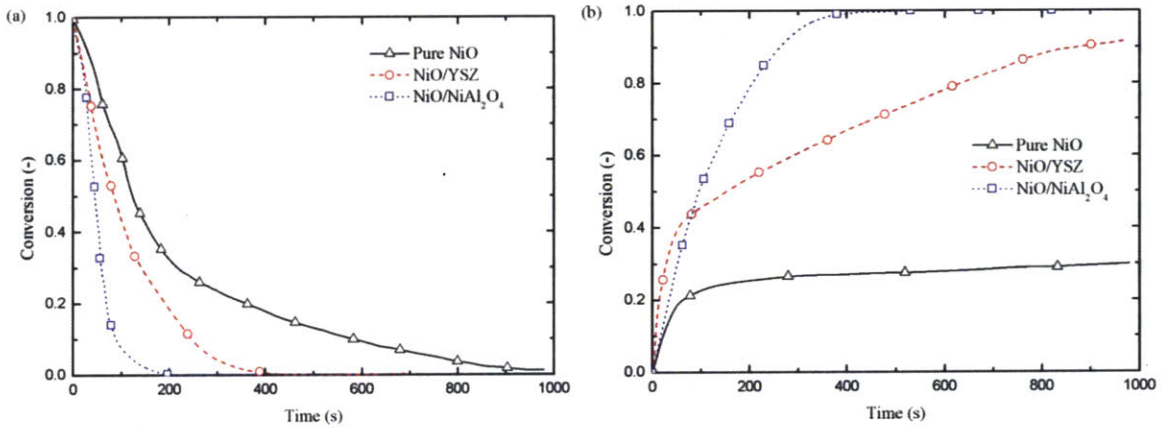

Figure 2-2 Conversion of pure NiO, NiO with YSZ or $NiAl_2O_4$ as binder in TGA for (a) reduction with H_2, and (b) oxidation with air [21].

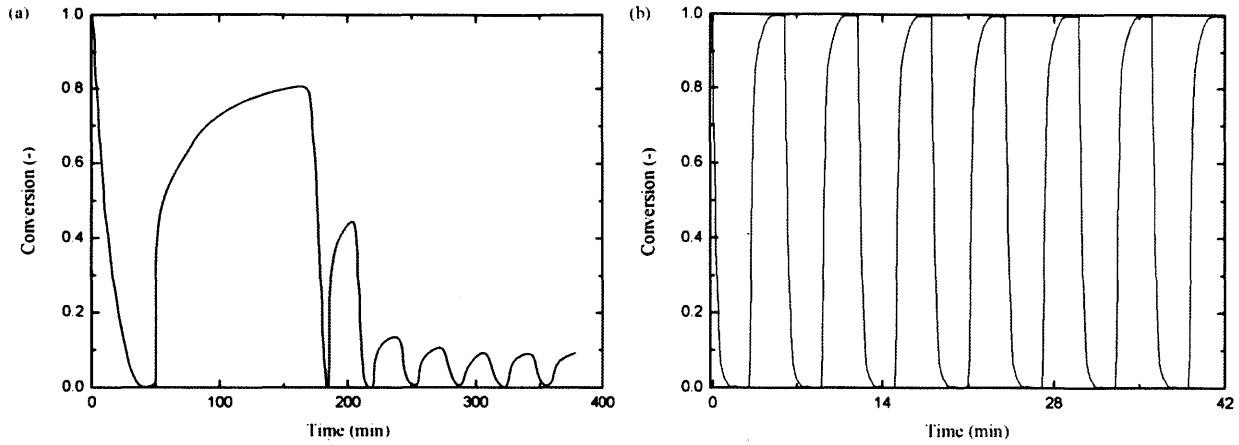

Figure 2-3 Conversion of (a) pure CuO, and (b) CuO/SiO_2 with CH_4 as reducing gas in TGA [22].

To reduce these detrimental effects, the reducible oxide as the active phase must be kept occluded in a porous matrix. In most research on oxygen carriers, inert binder is added into the oxygen carriers to enhance the mechanical strength for cyclic use. The inert binder also acts as an oxide ion conductor which helps enhance the ion permeability in the oxygen carriers [23, 24]. Moreover, the addition of inert material can also help maintain the pore structure inside the particle to provide a higher surface area for reaction. Al_2O_3 ($NiAl_2O_4$, $MgAl_2O_4$), SiO_2, TiO_2, ZrO_2, yttria-stabilized zirconia (YSZ), bentonite, sepiolite are most commonly used as binders for CLC. A detailed summary of OCs with binders utilized in the literature is presented in the Appendix A.

In some work, researchers also utilize graphite to create suitable macro-porosity to enhance the reactivity. Graphite is added during preparation, and after being calcined at high temperatures, graphite is oxidized into CO_2, hence leaving macro-pores in the particles. Thus the total surface area of the particles is increased. Kaolin is also used in some experiments as promoter for some iron oxide to increase the mechanical strength of the oxygen carrier. In some cases starch is also used as a pore-forming agent during the preparation of oxygen carrier, in order to increase porosity.

The preparation method influences the reactivity and the stability of the oxygen carriers. To achieve low production costs without sacrificing the performances of oxygen carriers, there is a great interest in the use of commercial techniques for oxygen carrier preparation. In the open literature, there are different types of oxygen preparation methods based on whether solid or liquid phase material is used for the particle preparation.

Type I, solid metal oxide and solid support material

- *Mechanical mixing* (MM): this method directly mixes the metal oxides and the binder at a certain ratio to form a paste. The paste is then extruded or compressed to form suitable shape and size.

- *Freeze granulation* (FG): Powders of metal oxides, support materials and a small amount dispersant are mixed in distilled water. After milling, some binder was added to keep the particles intact during later stages in the production process. The slurry is pumped into a spray nozzle, where atomizing air producew drops, which are sprayed into liquid nitrogen where they freeze instantaneously. The frozen water is then removed by sublimation in a freeze-drier operating at a pressure that corresponds to the vapor pressure over ice. After drying, the oxygen carriers are sintered.

- *Spray-drying* (SD): A powder mixture is dispersed in deionized water containing the necessary organic additives. Suspension is then homogenized either by milling in a planetary ball mill, or by means of a horizontal attrition mill. The water-based suspension is continuously stirred with a propeller blade mixer while being pumped to the spray-drying nozzle. After spray-drying, the fraction within the proper size range is separated from the rest. Then product is sintered at high temperature

Type II, aqueous metal solution and solid support material

- *Dry Impregnation* (DI): This method is also referred as *incipient wet impregnation.* For dry impregnation, the oxygen carriers are prepared by addition of a volume of metal solution corresponding to the total pore volume of the support particles. The aqueous solution is slowly added to the binder, with thorough stirring at room temperature. No filtration or drying steps are required with this method. Then oxygen carriers are calcined in a muffle oven to decompose the impregnated metal nitrate into insoluble metal oxide.

- *Wet Impregnation* (WI): the binder is immersed into an excess of the aqueous metal nitrate solution for a period of time at room temperature. After filtration, the oxygen carrier is dried and then calcined to decompose the impregnated metal nitrate into insoluble metal oxide. Repeated cycles can be made to increase the metal loading. Finally, oxygen carrier is calcined at high temperatures.

- *Deposition-precipitation* (DP): predetermined concentrations of aqueous solution of metal salts, depending on the desired metal oxide loading, is introduced into a container with a specific amount of binder particles suspended in a fixed amount of urea solution. The resulting slurry was maintained with vigorous mixing. The precipitate is then filtered, washed, and further dried before calcinations.

Type III, aqueous metal and support solutions

- *Co-precipitation* (CP): precursors to both the support and the metal oxides are mixed to form aqueous solutions. The precipitating agent (usually alcohol) is then introduced into the mixed solution, thus forming oxygen carriers with support material and the supported layer simultaneously. After filtration, the oxygen carrier is dried and then calcined at high temperatures. The dried powder is then milled to form proper size and shape.
- *Dissolution method* (DM): metal solution and binder solution are dissolved in water and then stirred, heated to become slurry. Similar procedures are followed as CP.
- *Sol-gel* (SG): solutions of metal alkoxide and binder are added to water and stirred. The solution is then acidified with a small amount of nitric acid. Then it is stirred and dried until a viscous mass remained. Then it is cut into desired size and then calcined at high temperatures.

For comparison, the regenerability, and the cost for different preparation methods are listed in Table 2-3. However, different methods listed here are from different literature using different oxygen-carriers, so the performance of different preparation method is also related to the behaviors of oxygen-carriers. Thus Table 2-3 only provides a general comparison. The optimal method of oxygen carrier preparation for a given chemical-looping system may vary case by case.

Table 2-3 A comparison of different preparation methods

Type	Technique	Homogeneity	Mechanical strength	Economic costs	Sintering resistance	Cu-based OC
I	MM	Poor	Poor	low	Poor	Poor
I	FG	Fair	Good	high	Fair	Poor
I	SD	Poor	Fair	fair	Poor	Poor
II	DI	Poor	Good	High	Good	Good
II	WI	Poor	Good	High	Good	Poor
II	DP	Poor	Fair	High	Poor	fair
III	CP	Fair	Poor	Fair	Fair	Fair
III	DM	Fair	Poor	Fair	Fair	Poor
III	SG	Good	Good	Very high	Good	Poor

The design and preparation of these oxygen carriers involve, to date, a complex trial-and-error procedure. Possible variables include the types of metal oxide, the oxygen carrier to support ratio (also referred to as the metal loading), the sintering temperature, the sintering time, size, etc. During the preparation of oxygen carriers, these variables are important to the behavior of the particles.

2.1.3 Experimental Results

Ni-, Cu-, Fe- and Mn-based oxygen carriers are most commonly used in literature. A brief comparison between these four oxygen carriers is listed in Table 2-4. In order to summarize the current development status of oxygen carriers in the open literature, a list of papers describing particles investigated so far is shown in Appendix A.

Table 2-4 A comparison of four most commonly used oxygen carriers.

	Fe_2O_3/Fe_3O_4	Mn_3O_4/MnO	CuO/Cu	NiO/Ni	Comments
R_o	0.03	0.07	0.20	0.21	binder will decrease Ro
reactivity	low	fair	high	very high	Nickel acts as catalyst for CH_4
cost ($/LB)	~0.1	~1	~3	~10	data from London Metal Exchange
health & environment	+	+	+	−	Nickel is toxic
thermodynamics	+	+	+	−	<99.5% conv. For NiO (Table 2-1)
reaction with CH_4	−	−	+	+ (Catalyst)	Reduction of CuO is endothermic
melting point	+	+	−	+	1085°C for Cu

In the following section, these four most important oxygen carriers are discussed and basic conclusions in the literature are also summarized.

Ni-based

Nickel oxides have been suggested as one of the most promising oxygen carriers for CLC due to its high reactivity, high oxygen capacity, and great chemical stability. Ni-based oxygen carriers are physically stable over a wide temperature range with no tendency of melting. The attrition rate of Ni-based oxygen carriers is very low, and hence it has longer lifetime. Major drawbacks of using nickel based oxygen carriers are that the conversion of CH_4, H_2, or CO is limited up to 99.5% due to its thermodynamics properties. Besides, the high cost of raw materials as well as its toxicity makes it questionable for large-scale applications.

Nickel oxides have advantages on the reduction of methane over other metal oxides in that metallic nickel (Ni^o) is known to catalyze both steam reforming:

$$CH_4 + H_2O \rightarrow CO + 3H_2 \quad (2.7)$$

and methane pyrolysis:

$$CH_4\ (g) \rightarrow C\ (s) + 2H_2\ (g) \quad (2.8)$$

The CH_4 cracking in the presence of Ni^o could lead to high concentrations of CO and H_2. Thus, even a small amount of metallic nickel existing on the particles can greatly improve the combustion reaction rate. However, methane pyrolysis reaction may lead to carbon formation on the outer surface of the particles. Carbon formation may further block the reaction between the oxygen in the inner core of the particles and the gases.

Pure NiO has been studied by Jin and Ishida [25]. Unsupported Ni-based oxygen carriers display poor regenerability over cycles due to nickel agglomeration on the surface during reduction. As a result, inert binder is commonly used for Ni-based oxygen carriers.

NiO supported by YSZ was the first oxygen carriers/binder pair system that has been proposed for CLC. It was reported by Ishida and co-workers [21, 23, 26-31] to be a good candidate for CLC. NiO/YSZ has good reactivity, and good stability. However, due to the high cost of support material and preparation method, this oxygen carrier system is less competitive in large-scale application. Later, Ishida and Jin [28, 29] suggested that Al_2O_3 could act as a good binder for nickel-based oxygen carriers with lower costs. However, the reactivity and conversion range decrease with several cycles of reaction due to the formation of spinels $NiAl_2O_4$ which is difficult to be reduced. One way to cope with this problem is to utilize $NiAl_2O_4$ rather than Al_2O_3 as the binder [21, 31]. NiO supported by $NiAl_2O_4$ exhibits excellent reactivity and regenerability and has been investigated extensively as oxygen carriers by various researchers since then. However, some drawbacks have been reported. One major drawback is that the preparation of $NiAl_2O_4$ as a binder consumes more nickel which is expensive and toxic. Besides, Johansson et al. [32] reported that unconverted methane always passed the reactor at the start of the reduction. This is likely due to the initial lack of Ni^o sites on the oxidized particles which can catalyze the incoming methane reaction. Similar results were observed by different researchers [32-34]. The other way to cope with the reactivity decay of NiO/Al_2O_3 pair is to use α-Al_2O_3 as binder rather than γ-Al_2O_3 for the preparation. α-Al_2O_3 is harder than γ-Al_2O_3 and less reactive with NiO and hence less likely to form $NiAl_2O_4$.Thus for the NiO/α-Al_2O_3 particles, more nickel exists in NiO phase. [35, 36].

Other binders have also been studied. Adanez et al [24] compared NiO supported by sepiolite, TiO_2, Al_2O_3, SiO_2, ZrO_2 by considering both reactivity and mechanical strength. TiO_2 was suggested as a good candidate since it provides adequate reactivity while maintains desirable crushing strength. The reactivity of NiO with sepiolite or Al_2O_3 as binder exhibits good reactivity but the mechanical strength is undesirable. ZrO_2 as a binder gives very low reactivity and SiO_2 gives bad regenerability. Ksepko et al [37] reported a comparison between SiO_2, ZrO_2, TiO_2, and sepiolite as a binder at a lower temperature range with the consideration of H_2S in fuel gas. Similar results were obtained as that from Adanez et al [24]. In addition, NiO/sepiolite showed excellent stability for the CLC reaction with or without the presence of H_2S. Stable performance was observed during five-cycle tests except for SiO_2 as a binder. Corbella et al. [38] reported 20-cycle tests of NiO/TiO_2 as oxygen carriers. It was found that the porosity increases with the number of cycles but the reactivity decreases. This is opposed to the observations from Adanez et al [24]. Corbella explained that this is due to the fact that NiO could react with TiO_2 to form $NiTiO_3$ which is a less reducible species. Besides, thermal decomposition of methane appears as a side reaction and carbon deposition on Ni particles was observed. The above two drawbacks might restrict the application of NiO/TiO_2 as OC for CLC.

Cu-based

Cu-based oxygen carriers have high reactivity in both reduction and oxidation cycles. It also has very high oxygen transfer capacity. Thermodynamics analysis shows that hydrocarbon fuels (e.g. methane, H_2, CO) can be converted almost completely into H_2O and CO_2 using CuO as oxygen carriers in chemical looping combustion. Cu-based oxygen carriers have strong mechanical strength, low attrition rate which gives long lifetime. Copper is abundant, non-toxic and much cheaper than nickel in nature.

Despite the above favorable features, CuO has been rejected by many researchers due to its tendency to decompose as well as its low melting point and high risk of agglomeration. When CuO is used as oxygen carriers, some oxygen can be seen during the inert period following the oxidation period due to the decomposition of CuO to Cu_2O which is the most stable phase at high temperature and low partial pressure of oxygen. In practical application an excess air in the oxidation cycle is advised as a way of minimizing CuO decomposition. When CuO-based particles reacted at 950°C or higher, there are major changes on the surface of the particle due to

the formation of a melt phase during reaction. However, special attention can be paid to the preparation, e.g., lower metal loading, more uniform distribution, etc., to minimize those impacts.

Pure CuO as oxygen carrier shows great reactivity but poor regenerability because of agglomeration [22] (as seen in Figure 2-3). Cao et al [39] also utilized bulk CuO with gasified solid fuels at lower temperature (600°C) for chemical-looping combustion such that the drawbacks of CuO at high temperatures could be avoided. No agglomeration was observed while the formation of Cu_2O was still recorded.

Cu-based oxygen carriers supported by inert binder are considered as a better option for chemical-looping combustion than pure CuO. CuO/Al_2O_3 is commonly used in the literature [22, 24, 40-48]. The solid-solid reactions between CuO and Al_2O_3 occur at temperatures above 850°C. Although it is fully reducible, the formation of $CuAl_2O_4$ will decrease the oxygen carrier reactivity. de Diego et al. [45] analyzed different CuO/Al_2O_3 oxygen carriers prepared by impregnation methods with a range of CuO content between 10 and 26 wt%. It was found that CuO/Al_2O_3 with a CuO content lower than 10wt% never agglomerated in the fluidized bed and that the CuO/Al_2O_3 oxygen carriers with loading greater than 20 wt% always agglomerated. The reactivity was reported to be high and stable and complete CH_4 conversion was obtained during most of the reduction. Attrition rate was low and decreased with increasing calcination temperature for preparation. Chuang et al. [48] reported the influence of preparation methods using CuO/Al_2O_3 as oxygen carriers. Carriers made by mechanical mixing and wet impregnation were rejected because of agglomeration, probably due to the fact the CuO was not well dispersed throughout Al_2O_3, but instead formed a surface layer on the composite particles. Co-precipitated carriers, on the other hand, did not agglomerate and showed a high carrying capacity. It was also reported that pH is a significant factor influencing the carrying capacity of the co-precipitated carrier: a high pH (~9.7) favors the production of a hard and densely packed carrier while a low pH (~7.1) results in carriers, which are soft, porous, and loosely packed internally.

SiO_2 was considered by several researchers as a binder for Cu [22, 24, 38, 49-52]. It has been shown that SiO_2 is a stable binder for copper. No solid-solid reactions between SiO_2 and CuO were observed. CuO supported on SiO_2 shows high reactivity, but lower compared to Ni-based oxygen carriers. However, CuO decomposition to Cu_2O was still observed for CuO/SiO_2. TiO_2 was also considered as a Cu binder [22, 24, 43]. Corbella et al. [43] reported a 20-cycle performance test of Cu/TiO_2 in a fixed-bed reactor, and a high reactivity and a good

regenerability at 900°C was obtained. No obvious interaction between copper and the support was observed, thus oxygen carriers prepared with TiO_2 as inert are another good candidate for Cu-based oxygen carriers.

Fe-based

Fe_2O_3 is a cheap, abundant, non-toxic metal oxide that can convert hydrocarbon fuels completely into CO_2 and H_2O. The reactivity with CH_4 is low compared to NiO, possibly due to the fact that Fe_2O_3 is reduced to Fe_3O_4 rather than to a metallic phase that could help catalyze the decomposition of hydrocarbons. However, the reactivity of Fe_2O_3 with CO and H_2 has been found to be high [53, 54]. Therefore it seems reasonable to believe that the rate-limiting step for chemical-looping combustion of hydrocarbons using Fe_2O_3 as oxygen carrier is conversion of CH_4 into reactive intermediates such as CO and H_2. Thermodynamics analysis shows that only Fe_2O_3 reducing to Fe_3O_4 can convert methane completely into CO_2 and H_2O. Further reducing to FeO or Fe will generate H_2 or CO. This could be easily controlled in the real application by the using a shorter reducing time.

Fe_2O_3 supported on different binders has been studied [24, 54-58]. Fe_2O_3 with $MgAl_2O_4$, ZrO_2 and Al_2O_3 shows good reactivity. Fe_2O_3 is considerably more inert toward reaction with Al_2O_3 under oxidizing conditions, compared to other transition-state metal oxides, i.e., nickel, copper, and cobalt, which all form irreversible spinels with alumina at high temperatures. The formation of $FeAl_2O_4$ may still occur following the reduction sequence of Fe_2O_3-Fe_3O_4-$FeAl_2O_4$-Fe for the reduction of Fe_2O_3/Al_2O_3 OC pair; however, it is an active phase and can be re-oxidized during the subsequent cycles [59]. No chemical reaction has been observed between iron oxide and zirconia, independent of the sintering temperature. However, major solid-solid reactions were observed in the Fe_2O_3/TiO_2 samples, with the formation of Fe_2TiO_5 during sintering at all temperatures [31, 56].

Ilmenite has recently been tested by various researchers [60-68]. As a natural mineral composed of $FeTiO_4$, it is a low-cost and promising oxygen carrier for CLC. Leion et al [65] showed that ilmenite gives high conversion of CO and H_2 with high reactivity but the conversion of CH_4 is moderate. Adanez et al [67] pointed out that for ilmenite as oxygen carriers, there is a activation period during first several cycles, after which the reactivity increases while the oxygen capacity decreases due to the structural changes during the activation period. A previous step for

calcination was suggested to reduce the activation period. Kolbitsch et al [60] and Berguerand et al [61-64, 69] successfully operated chemical looping combustion up to 120 kWth using ilmenite as oxygen carriers. In addition, some other forms of iron-based OCs have been investigated extensively as well, including natural minerals such as iron ores [70-73], or by-products from other process, such as oxide scales from the steel industry [71, 74, 75], or an iron waste from aluminum production [76] as oxygen carriers. These cheap iron-base OCs provide great options, especially for CLC with solid fuels, in which the makeup rate of OCs is usually high because the impurities in the solid fuels, e.g. ashes, sulfur species, mercury etc., will react with OCs to degrade the reactivities and also cause the OC weight loss during the ash separation process.

Mn-based

Mn-based oxygen carrier has no obvious disadvantages compared with Ni- Cu- Fe- based oxygen carriers and thus is considered a good option by various researchers [24, 42, 47, 77, 78]. Because MnO_2 decomposes to Mn_2O_3 in air at about 500°C and Mn_2O_3 decomposes to Mn_3O_4 at approximately 900°C [79], thus the system Mn_3O_4/MnO is most likely the OC pair system to be used. Manganese oxide is not toxic and has a high melting point. The conversion of fuel to CO_2 and H_2O is complete and twice the amount of free oxygen as the iron-system can be transferred. However, in the open literature, manganese oxides for chemical looping combustion have not been investigated to a large extent.

Mattisson et al. [47] investigated Mn_3O_4 impregnated on Al_2O_3 carrier and concluded that its reactivity was rather poor mostly due to the formation of $MnAl_2O_4$ during sintering. Though the re-oxidation of the manganese aluminate is thermodynamically feasible at temperatures below 820°C, the reaction has been found to be very slow [80]. Cho et al. [42] investigated the same composition although on freeze-granulated oxygen carriers. Again the reactivity was found to be too poor and furthermore the oxygen carriers were too soft.

Adanez et al. [24] tested manganese oxides on five different inert materials: Al_2O_3, Sepiolite, SiO_2, TiO_2 and ZrO_2. It was found that there are reactions between the support and manganese when using Al_2O_3, SiO_2 and TiO_2 resulting in phases of no or low reactivity. However, for ZrO_2 there is little solid-solid interaction between manganese and zirconia. Similar results were obtained by Zafar et al. [50], Ryden et al [58] and Johansson et al. [77]. Johansson et al. [77] also investigated the influence of adding three compounds, i.e., CaO, MgO and CeO_2, to

stabilize the Mn_3O_4/ZrO_2. It was found that much higher reactivity can be obtained than those without stabilizing compounds.

2.2 Chemical-looping Reactor System

2.2.1 Reactor Candidates

Successful application of chemical-looping combustion requires proper designs of the combustion reactor systems. A good CLC reactor system should have the following characteristics:

Gas-solid contact patterns: The contact of phases is essential for a good design. In order to maintain a fast and complete combustion of fuels, the reacting gas should be in perfect contact with oxygen carriers. The dilution impact of gaseous production should be limited, and the leakage of unburned fuel should also be minimized.

Temperature control: The temperature distribution within reactors should be uniform to maintain a stable operating condition. It should be easy to control the temperature within the reactor to achieve the optimal operating conditions of OCs. The effects of endothermic or exothermic reactions on the temperature variation with time should be minimized.

Regenerability: the chemical-looping operation should be smooth and continuous. The impact of operation on equipment (corrosion, collision, thermal stress, etc.) should be minimized. The effect of sintering or agglomeration should also be avoided.

Scale-up application: The design should be easy to scale-up for large scale applications.

Pressure drop: The pressure drop within the reactor should be low and a small amount of extra power is adequate to maintain the operation.

Attrition and fine particles: The attrition should be limited. Proper control methods should be available to recover the fine particles from flue gas.

Conversion, dilution and OC utilization: The conversion of fuel gas must be close to complete. The leakage of fuel should be limited, and the dilution of gas product with air should be avoided. There is no strict requirement on the conversion of particles but a high conversion is desirable.

A CLC reactor system includes a fuel reactor (FR) and an air reactor (AR), as well as proper connections between them. A variety of reactor options are available in the open literature for the FR and AR. This includes interconnected fluidized-bed reactors (FzB), moving bed

reactor (MvB), packed bed reactor (PcB) and rotating bed reactor (RoB). A brief comparison of these reactor units is presented in Table 2-5. The discussion of the new rotary reactor is also included. Detailed information is referred to section 3-5. Based on different reactor units, a variety of CLC reactor system designs have been proposed and investigated in the open literature:

Interconnected fluidized-bed reactors [19]: This is the most commonly investigated reactor systems. The reactor system depicted in Figure 2-4(a) shows a typical layout of this reactor system. It consists of an air reactor, a fuel reactor and a cyclone. The air reactor is a fast fluidized-bed with concurrent pneumatic transport. The upper part of the air reactor operates as a riser where the oxidized particles are entrained. The oxygen carrier is subsequently separated from the carrying flue gas in a cyclone, the remaining gas leaving the cyclone as oxygen-depleted air. The particles then fall into the fuel reactor fluidized with fuel gas. The fuel reactor is a bubbling fluidized bed or a turbulent fluidized bed. Afterwards, the oxygen carrier is re-circulated to the air reactor by gravity through the loop-seal for regeneration. Particle loop-seals located between the air and fuel reactors are used to accommodate pressure differences between the reactors, and avoid mixing of the flue gases in their respective exhausts. The major difficulty of fluidized-bed reactors remains with the transport of a large amount of particles, especially at elevated pressures. Bubble formation may lower the fuel concentration and limited solid in the bubble phase restricted the heterogeneous reactions. Besides, efficient cyclones are necessary to separate the oxygen carrier particles from flue stream. Gas leakage between fuel and air reactors could happen if there is a pressure difference between reactors. Effective loop-seals are critical to the pressure balance and hence the minimization of the gas leakage in the system [81]. For coal-fired fluidized-bed CLC, unreacted chars and syngas can be transported from fuel reactor to air reactor by the circulation of oxygen carriers. A higher temperature and a specially designed loop-seal which is fluidized by steam can generally enhance the solid fuel gasification and hence decrease the leakage [82].

In the open literature, research on reactor designs has been almost exclusively focused on interconnected fluidized bed reactor systems. This can be seen in Appendix A and Appendix B. Lyngfelt et al. [19] proposed the first prototype for CLC. After that, several CLC prototypes have been designed and operated by various research groups under realistic conditions with sufficient operation time. Among them major contributors are Chalmers University of Technology in Sweden, Vienna University of Technology in Austria, CSIC-ECB in Spain, Tokyo Institute of

Technology, Korea Institute of Energy Research and Southeast University in China. Currently, laboratory scale systems can be operated with different types of fuel up to 145kWth with the aim to realize systems to MW-level in the near future. A brief review of the batch-scale fluidized-bed prototypes are summarized in Section 2.2.2.

Moving bed reactor [11, 83, 84]: The utilization of a moving bed as FR and a fast fluidized bed reactor as a AR for CLC has been suggested and tested by Fan and co-workers at Ohio State University. Figure 2-4(b) depicts the gas-solid contacting pattern for countercurrent moving bed reactors as well as a 25kW pilot-scale prototype unit for Syngas Chemical Looping (SCL) process constructed at Ohio State University. As shown in Figure 2-4(b), the reactor consists of a reducer, where the metal oxide (e.g., Fe_2O_3) is reduced by syngas, a oxidizer, where the reduced metal oxide (e.g., Fe, FeO) is oxidized by steam to generate H_2, and a combustor, where the oxidized metal oxide (e.g., Fe_3O_4) is fully regenerated (to Fe_2O_3) by oxygen. The oxygen carrier particles are pneumatically transported from the combustor to the top of the reducer and then transported downwards to the oxidizer by gravity. Iron-based metal oxide is suggested as the oxygen carrier for the moving bed reactor because of its multiple oxidation modes. A bench-scale moving-bed reactor with a maximum capacity of 2.5 kW has been constructed to test the SCL process [11]. The reactor is maintained at 900°C with the fuel conversion efficiency close to unity. Besides, a sub-pilot scale unit has also been constructed with the power capacity of 25kW [11].

A moving bed reactor has the advantages that the mixing of gas and solid phases along moving direction is small such that the dilution effect of product on the incoming fuel is minimized. The conversion of particles as well as fuels can reach a higher level than that in a well stirred reactor (fluidized bed reactor). However, similar technical difficulties still exist in the particle circulation process. The temperature variation within reactors is non-uniform which may lead to exergy loss. Gas leakage may occur when there is a pressure mismatch between the moving bed and the fluidized bed. Besides, special attention should be paid to the robustness of control.

Packed bed reactor [18, 85-87]: The packed bed reactor, as a fixed bed reactor, has been mainly investigated and tested at by Noorman and co-workers University of Twente in Netherlands. Figure 2-4(c) shows the schematic drawing of the packed bed reactor: the oxygen carrier particles are packed into the reactor and they are alternately exposed to reducing and

oxidizing conditions via periodic switching of the gas feed streams. Two reactors in parallel working are used alternately to assure a continuous high temperature gas stream supply to the downstream gas turbine. The process consists of alternate oxidation and reduction cycles in two separate reactors, intermittently alternated with short periods of mild fluidization of the bed after each cycle to level off temperature and concentration profiles.

A first experimental evaluation of the concept was made with a Cu-based oxygen-carrier and CH_4 as fuel [86]. The packed bed was pressurized at 2.5bar with the initial temperature of 650°C. The propagation of the reaction front in the packed bed was clearly observed where the local temperature of the oxygen carriers increased by 200°C during the oxidation. The fuel was completely converted during the initial period of the operation, although severe methane slip was observed when the reduction temperature is low. The pressure drop during the reduction and oxidation period was 0.2 and 0.6 bar, respectively. Carbon deposition was reported when methane/nitrogen was used as feed gas. However, with the addition of steam or CO_2, carbon deposition can be completely suppressed [87]. Parametric study [87] showed that the reduction temperature is one of the most important parameters for the packed-bed CLC. $CaMnO_3$ was also tested in the packed-bed reactor [87], although poor stability restricted the usage of this material for CLC.

The main advantages of reactor concepts based on packed bed reactor technology are that the separation of gas and particles is intrinsically avoided, that the reactor design can be much more compact, and that they allow for better utilization of the oxygen. Besides, since the operation is in stationary beds, no extra energy is needed for circulation, and the exergy loss associated with the heat transfer between two reactors needed in the previous case can be avoided. However, one of the biggest challenges associated with stationary reactor system is that heating and cooling the packed particles may cause a large temperature fluctuation within the reactor, as observed in ref. [86]. The thermal distortion associated with temperature fluctuation may crack the oxygen carrier particles and increase the risk of failure. Other disadvantages of the concept include the fuel slip during the switching period and the necessity to use a high temperature, high flow gas switching system.

Rotating bed reactor [88]: As depicted in Figure 2-4(d), an annulus fixed bed containing OC particles rotates when fuel and air gases are introduced radially outwards through the reactor. Inert gas, (in this case, steam) is fed between air and fuel sectors, and separation walls on the

outer and inner walls are used to avoid mixing. The advantages of the rotating bed reactor include the compactness of design, limited energy for circulation, and the feasibility of scale-up and commercialization. However, the main challenge is to avoid the gas leakage and dilution between fuel and air streams, which at the moment are unavoidable [81]. A lab-scale rotating bed reactor was constructed and tested using CuO/Al_2O_3 as the oxygen carriers and CH_4 as fuel with the operating temperature of 650-800°C [89]. The fuel conversion efficiency is around 90% and less than 10% of the CO_2 leaves the reactor from the air side. However, a major air slippage from the air sector was observed which leads to a low CO_2 purity (30-65%) in the flue stream.

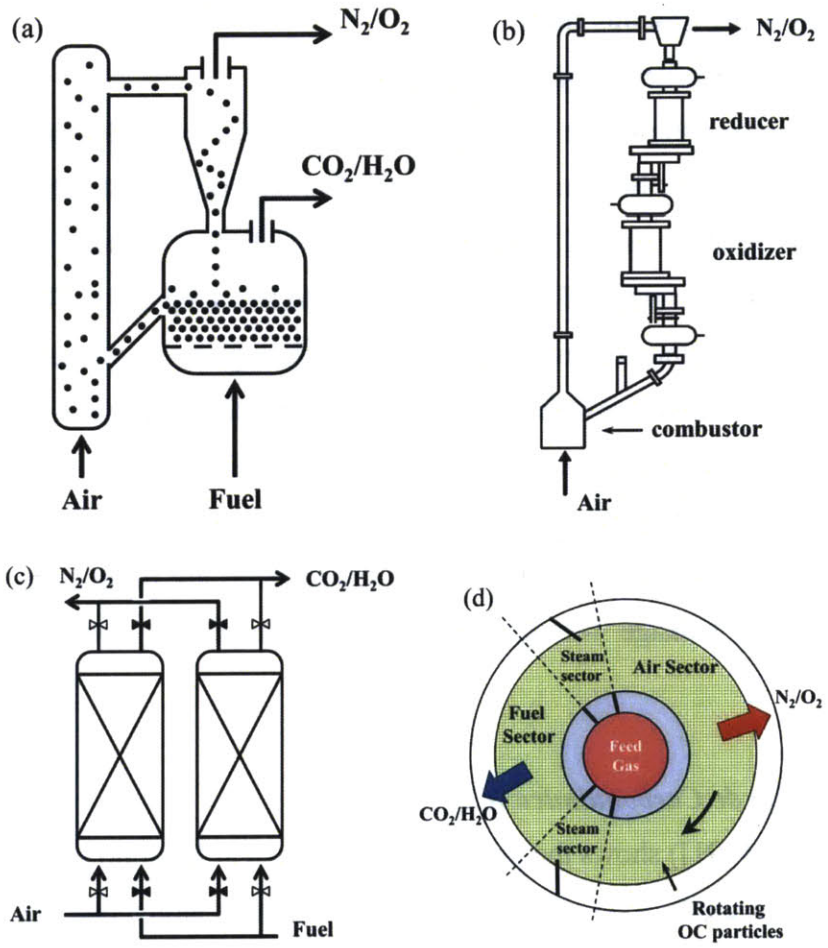

Figure 2-4 Potential reactor candidates for Chemical-looping combustion: (a) interconnected fluidized bed reactors [81]; (b) moving bed reactors [11]; (c) packed bed reactors [86]; (d) horizontal rotating reactors [88].

2.2.2 Fluidized-bed Prototypes

Concerning CLC reactor design, currently six groups of fluidized-bed prototypes have been successfully constructed and reported extensively in the literature, all of which are based on

inter-connected fluidized-bed reactor designs: four of them are using gaseous fuel while the other two are using solid fuels (coal, biomass). All of them are based on the concept of inter-connected fluidized beds proposed by Lyngfelt in 2001 [19], i.e. a combination of a FR and an AR with proper connections. However, the scale of the reactors, the efficiency of combustion, and the power output are far different. A summary of the operating conditions is shown in Appendix B. The basic designs and operation experience with these prototypes can lay a foundation for the scale-up and commercialization of CLC technology.

2.2.1.1 Prototypes using gaseous fuels

***Prototype in Chalmers University of Technology* (I)**

Figure 2-5 ([90]) shows the prototype designed and constructed in 2004[1] in Chalmers University of Technology in Sweden with a primary thermal capacity of 10kW. This prototype is composed of a high-velocity riser (C), an air reactor (B) and a low velocity bubbling fuel reactor (A). These three parts are connected through cyclone and two loop seals. The gas velocity of air injected at the bottom of the AR increases as it goes through the riser because of the smaller cross-section area, and hence provides the driving force for the circulation of particles between the two beds. Thus a secondary air injection system is avoided. The particles carried away from the riser are recovered by a cyclone and led to the fuel reactor. The cyclone is used to separate particles from the flue gas. From the fuel reactor the particles are returned to the air reactor by means of gravity. No leakage between reactors and a high fuel conversion (98-99%) was reported.

***Prototype in Instituto de Carboquimica (CSIC)* (II)**

Figure 2-6 ([11, 91]) shows the prototype constructed at Instituto de Carboquimica (CSIC) in Zaragoza Spain in 2006. Two versions have been built: a larger one has a power level of 10kW, and the smaller is of 500W. This prototype is basically composed of two interconnected fluidized-bed reactors, a riser for solids transported to the fuel reactor, a solid valve for an accurate control of the solids feed to the fuel reactor, and two loop seals to avoid leakage. The fuel and air reactors work in the bubbling fluidization regime. An updated version is also designed where the secondary air is introduced at the top of the bubbling bed AR to help particle

[1] The year mentioned is the year of first published paper for this prototype. Similar cases are for other prototypes.

entrainment. It is worth noting that both prototype versions incorporate a bed-freeboard structure for AR and FR which could reduce the particle elutriation. No gas leakage between reactors was detected.

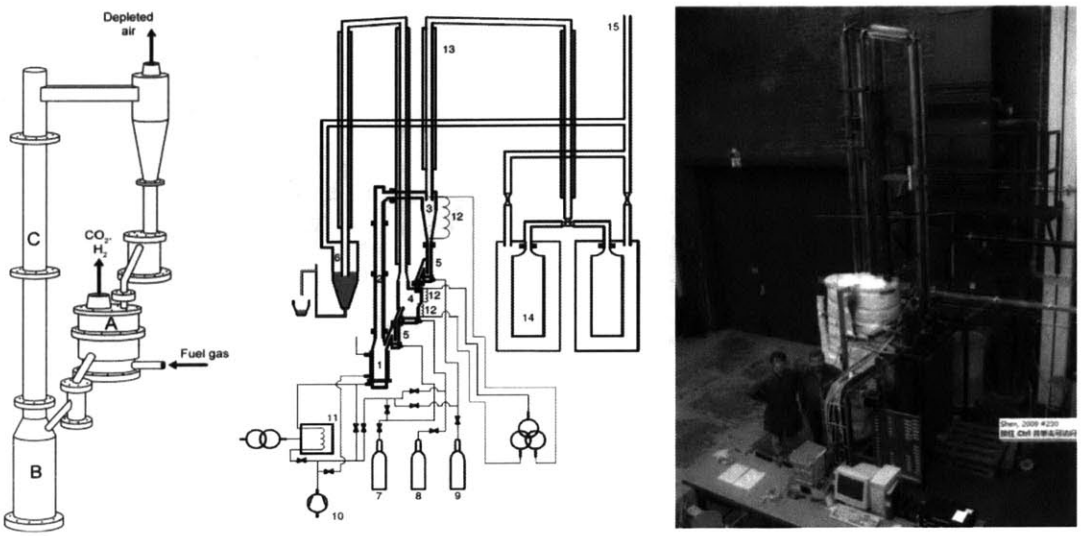

Figure 2-5 Drawing of prototype constructed in Chalmers University of Technology [11, 90]

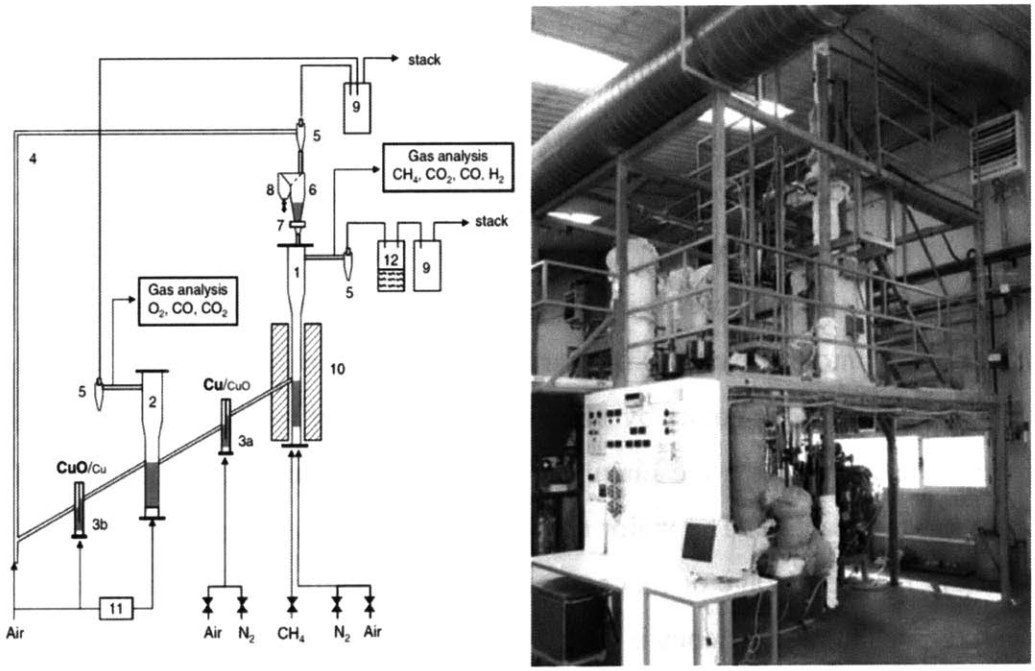

Figure 2-6 Drawing of prototype constructed in CSIC [11, 91]

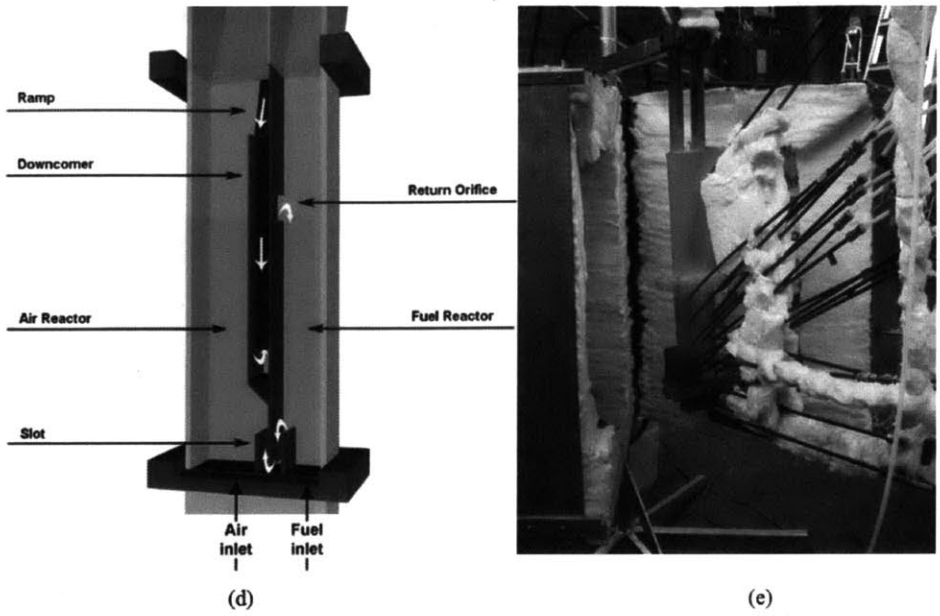

Figure 2-7 Drawing of the prototype constructed in Chalmers University of Technology [40, 92, 93].

***Smaller Prototype in Chalmers University of Technology* (III)**

This prototype of CLC was designed and constructed in 2004 in Chalmers University of Technology in Sweden. The reactor system is designed for a fuel flow corresponding to a thermal capacity between 100 and 300 W. Figure 2-7 shows a layout of this prototype. This prototype is a very compact one, which consists of a two-compartment fluidized bed in one reactor. One compartment is the air reactor and the other compartment is the fuel reactor. On top of this section, both reactors increase in width in order to decrease the gas velocities and allow particles to fall back into the reactors. The particles falling down in the sloping section above the air reactor are led to the downcomer by a leaning wall. The slot in Figure 2-7 through which the particles from the fuel reactor are circulated to the air reactor is designed to minimize gas leakage between the reactors. The major drawback is that gas leakage is high (could be >10% [40]), especially for the leakage of fuel accompanying the particles circulating from FR to AR, and thus carbon separation efficiency is low.

Table 2-5 Comparison of CLC reactor candidates

	Gas-solid contact	Temperature control	Regenerability	Scale-up application	Pressure drop	Attrition and fine particles	OC utilization	Fuel conversion and separation	Gas leakage
Fluidized bed, Figure 2-4(a)	Limited solid in bubbles, inefficient gas solid contact in bubbles [11]	Isothermal, perfect heat exchange and large heat transport available [94]	Steady operation possible, agglomeration may impact operation, collision may cause vessel erosion [94]	Large scale operation possible, severe difficulties for pressurization [81, 85]	Significant pressure drop to sustain solid weight [94]	High attrition, particles may be cracked or fractured [94]	Much more needed than stoichiometry, insufficient usage of oxygen carrier [95]	Non-uniform residence time and dilution by product decreases fuel conversion, effective cyclones needed for separation. [11, 19]	Pressure mismatch and gas carry-over in the particles cause leakage. Effective loop-seal is critical. More leakage for solid fuel.
Moving bed, Figure 2-4(b)	Fair gas-solid mixing, non-uniform product distribution	Temperature gradients can be controlled by proper gas and solid flows	Smooth and steady operation possible, flexible flowing patterns available, similar issues (erosion or agglomeration) [94]	Large-scale operations possible, similar difficulties for pressurization [81, 85]	Intermediate, large enough to circulate particles [11, 94]	Intermediate between packed and fluidized beds [94]	Intermediate between packed and fluidized beds	High fuel conversion possible, fuel or product gas may bypass which may decrease separation efficiency	Similar gas leakage problems as in fluidized bed. Effective loop-seal is critical.
Packed bed, Figure 2-4(c)	Good gas-solid contact, highly reactivity possible, product gas doesn't dilute reactant[85, 96]	Severe temperature control difficulties, mild fluidization may be needed after each cycle to level off temperature profiles [81, 94]	Periodically operation possible, severe control problem during the switching process[81, 94]	Possible to work under pressure, serious temperature control problems, sophisticated systems needed for gas control [81, 94]	Pressure drop is relatively small, 0.2~0.6 bar for total pressure of 2.5 bar [86]	Limited solid attrition or fine particles [94]	Effective utilization of OC is possible, smaller amount is needed	High fuel conversion possible, high CO_2 separation efficiency possible [85, 96]	Severe fuel slip occurs at low temperature or during the gas switching period [85, 96]
Rotary bed, Figure 2-4(d)	Good gas-solid contact, high reactivity possible, limited product gas dilution	Temperature is controlled only by gas flow, high thermal contact resistance between particles	Smooth and periodical operation possible	Widely used, suitable for particles liable to sinter or melt	Pressure drop is small, similar as in packed bed	Limited solid attrition or fine particles [88, 94]	Effective utilization of OC is possible, smaller amount is needed	Complete fuel conversion possible, but gas dilution is unavoidable [81, 88]	Unavoidable gas leakage and dilution between the fuel and air sector [81, 88]
New rotary reactor, Figure 3-3	small channel favors the mass diffusion	Temperature is controlled by flow and solid layer, high conductive material enhances isothermality	Continuous cyclic stationary operation, bulk layer maintains stability, thermal distortion during start-up may impact reactor	Large-scale operation possible, reactors can be in parallelized. Gas sealing system is very critical.	Pressure drop is negligible, only due to skin friction	Limited solid attrition or fine particles	Non-uniform coating of oxygen carrier can greatly enhance the OC utilization	High fuel conversion possible, complete CO_2 separation possible due to effective purging sectors	Gas may leak through radial, peripheral seals. Effective seals are critical.

***Prototype in Vienna University of Technology* (IV)**

This prototype was designed and constructed in Vienna University of Technology in Austria in 2007. It has a designed fuel power of 120kW, and operations up to 145kW have been reported in the literature [60]. Figure 2-8 shows the sketch of this prototype. This design consists of mainly a FR, an AR, an upper loop seal, a lower loop seal, an internal loop seal, and two cyclones. Two circulation loops are formed between FR and AR: the primary circulation loop, and the local secondary circulation loop. The entrainment of the AR determines global solids circulation in the primary loop. A secondary air injection is located at the middle portion of AR to enable the effective control of global circulation rates. The solids are separated from the AR exhaust stream in a cyclone separator and passed over through a fluidized loop seal (upper loop-seal) into the right-hand side reactor (secondary reactor). This prototype is also named as dual circulating fluidized bed (DCFB) system. Very limited gas leakage (<1% [97]) was observed, and good carbon separation efficiency can be obtained.

2.2.1.2 Prototypes using solid fuels

***Prototype for solid fuels in Chalmers University of Technology* (V)**

This prototype was designed and constructed in Chalmers University of Technology in Sweden in 2008, with power output level of 10kW. This prototype was based on the design of gaseous prototype (Figure 2-5), but important modifications in the fuel reactor chamber and the inclusion of an additional solids recirculation loop are made to adapt the system for solid fuels. The fuel reactor is divided into three chambers (as seen in Figure 2-9): (i) a low velocity part where the fuel particles devolatize, are gasified and the volatiles and the syngas reduces the oxidized metal particles; (ii) a carbon stripper that aims at separating the remaining and unreacted coal particles from the metal oxides; (iii) a high velocity part, where a certain proportion of both particle types are entrained upwards, in order to provide a particles recirculation and recollection back to the fuel reactor via the smaller fuel reactor cyclone. Two particle locks are located between the air and the fuel reactors solids inlets/outlets. They accommodate for the pressure differences and prevent gas mixing between the reactors. The fuel conversion efficiency were reported to be rather low (<80% [61-63]) because of the low reactivity of OCs with solid fuels. The unburnt solid fuels will be carried with OCs into AR thus

the carbon separation efficiency is also low (about 80% [61-63]). Nevertheless, this is the very first prototype for chemical looping combustion using solid fuels. Further improvement can be expected for this prototype.

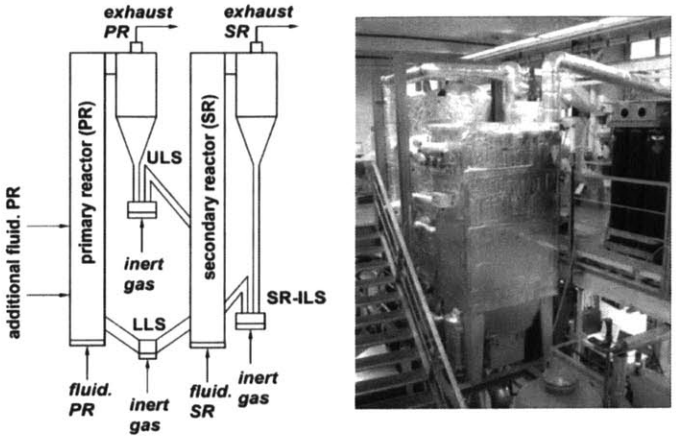

Figure 2-8 Drawing of the prototype constructed in Vienna University of Technology [11, 97]

LLS: lower loop seal; SR: secondary reactor; ILS: internal loop seal

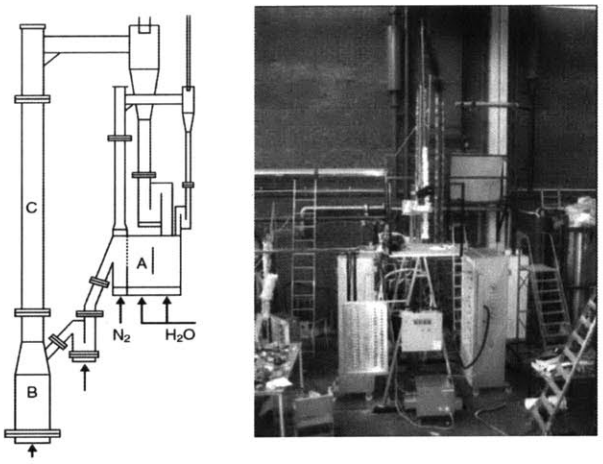

Figure 2-9 drawing of the prototype constructed in Chalmers University of Technology [11, 61]

***Prototype in Southeast University* (VI)**

This prototype was designed and constructed in Southeast University in China in 2009. Several modified versions have also been tested and investigated. Two levels of thermal capacities have been reported, 10kW and 1kW. Figure 2-10 showed the sketch of the design. It is composed of a high velocity AR, a cyclone, and a spout-fluid bed as FR. The high velocity fluidized bed is directly connected to the spout-fluid bed through the cyclone. Compared to

previous prototypes, a spout-fluid bed, instead of a bubbling fluidized bed, is adopted for the fuel reactor because of strong solids mixing and long residence time of coal particles in the spout-fluid bed. In this way, the energy conversion efficiency can be enhanced. In order to prevent the dilution between FR and AR, there exists a specially designed two-compartment configuration inside the spout-fluid bed. The major compartment is a reaction chamber, and the minor one is inner seal loop. The reaction chamber allows the combination of coal gasification and oxygen carrier reduction with coal syngas to proceed inside the spout-fluid bed. The inner seal allows particle movement from the reaction chamber to AR, and prevents backward bypassing of the flue gas from AR to the spout-fluid bed. Generally, the particle size of OC is smaller than the solid fuel particles, thus the re-circulation through inner seal is easier for OC particles. Compared to prototype V, the energy conversion efficiency is enhanced (around 90%) due to the better mixing in the spout-fluid bed. However, the carbon capture efficiency is still low (around 80%) and this is limited by the inner loop through which unreacted chars and syngas can be transported from fuel reactor to air reactor by the circulation of oxygen carriers. A higher temperature will generally enhance the solid fuel gasification, increase the reactivity and hence decrease unburnt fuels being transported to AR. Besides, the modified inner seal loop, which is fluidized by steam, can decrease the amount of coal particles transported to the AR, thus the carbon separation efficiency is greatly enhanced (up to 95% [82]).

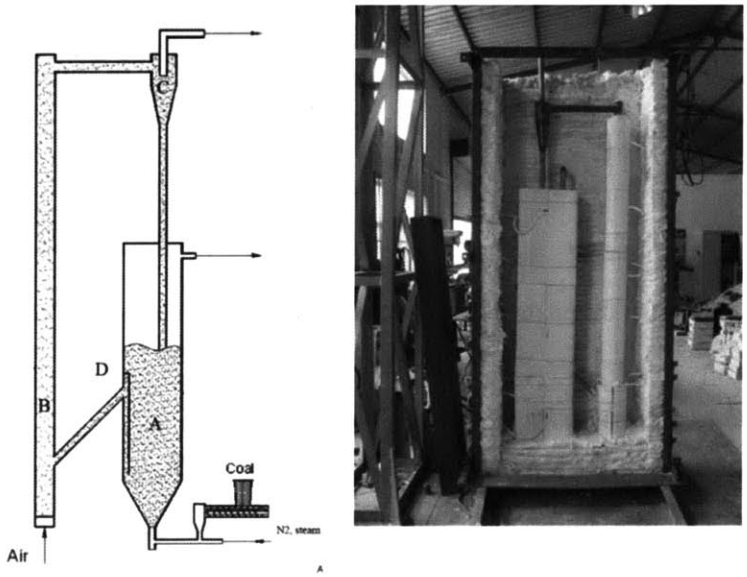

Figure 2-10 Drawing of prototype constructed in Southeast University [11, 98]

A) FR, spout-fluidized bed, B) AR, C) cyclone, D) inner seal

2.3 Modeling of Chemical-looping Combustion

One critical step toward commercialization of the CLC process is the development of accurate mathematical models. Numerical modeling and simulation of chemical-looping combustion can provide valuable information on the reactor design, operating condition selection, and the process integration. However, few research papers focus on numerical modeling and simulations of chemical-looping process, as compared to vast amount of research work concentrating on the material investigation and prototype operation. The reason for this lies in the intrinsic complexity of the multi-phase reactive flow in chemical-looping combustion, especially for fluidized-bed reactors. The lack of mature modeling tools makes the computations unreliable and excessively time-consuming. This section briefly addresses the three major aspects of modeling: heterogeneous kinetics modeling, reactor modeling, and the process simulation.

2.3.1 Oxygen Carrier Kinetics

Kinetic modeling offers the opportunity to gain a better understanding of the reduction and oxidation reactions and to predict the effect of varying the reaction conditions. It can reveal new and useful information that is not apparent by simple observation of the experimental data. Kinetic modeling also provides insight into the mechanisms of a chemical reaction in relation to oxygen carrier composition. Although, the accurate modeling of oxygen carrier reactivity always needs the specification of hydrodynamics within reactors, it is generally easier and helpful to first have a look at the heterogeneous solid-gas reactions without coupling with fluid fields. The kinetics models are helpful for the estimation of the operating conditions: inventory, heat balance of reactor, etc. Once the mechanism is determined, it is then possible to optimize the reaction conditions based on that mechanism.

For a solid-gas reaction,

$$A\,(\mathrm{g}) + b\,B(\mathrm{s}) \rightarrow r\,R\,(\mathrm{g}) + s\,S\,(\mathrm{s}) \tag{2.9}$$

The reaction process for kinetics modeling can be formulated as:

$$\frac{dX}{dt} = k(T) f(X) g(C_A) \tag{2.10}$$

where C_A represents the concentration of the gas reactant and g describes the effect of gas concentration on reactivity. X is the oxygen carrier conversion. f depicts the changes of the solid

conversion on reactivity, i.e. pores and grains structure changes. $k(T)$ can be well represented by Arrhenius' law:

$$k = k_0 e^{-E_a / R_u T} \tag{2.11}$$

where k_0 is the pre-exponential factor, T is the temperature, R_u is the gas universal constant, and E_a is the activation energy.

Thus for a specific kinetics model with expressions assumed for $f(\alpha)$ and $g(C_A)$, non-linear regression analysis can be utilized to estimate the kinetics parameters. Work has been carried out using kinetics modeling of OC particles. Four types of kinetics models have been considered to represent the kinetics in fluidized-bed particle reactions of the CLC process: i) power-law relation; ii) shrinking-core model; iii) nucleation and nuclei growth model; and iv) changing grain size model. Detailed discussion can be found in ref. [81].

2.3.2 Reactor Simulation

Chemical-looping combustion in the reactor typically involves a highly sophisticated gas-solid interaction. The gas-solid reactive flows are generally very complex due to the strong coupling between three aspects: kinetics, hydrodynamics, and inter-phase interaction. This is especially the case when the solid is pneumatically transported within the reactor as in inter-connected fluidized-bed reactors or the moving-bed reactors. A mature theory which covers all the above aspects and is suitable for both lean and dense phases of solid-gas reactive flows is still missing. One commonly suggested way is to utilize the modified Navior-Stokes equations for multi-phase flow incorporating kinetic theory model of granular flow (Gidaspow [99]) to characterize the effect of particle collision, motion and friction on both gas phase and solid phase. The kinetic theory of granular flow is an extension of the classical kinetic gas theory. Granular flow models were first applied to CLC process in 2008 [100] although these models have been frequently used for bubbling fluidized beds, mixing, downflow reactors and spouted beds [101]. For review purpose, the governing equations for the solid-gas phases flow specifically for fluidized-bed CLC are summarized in the following. For other scenarios such as rotary bed or packed bed flow, the governing equations can be modified correspondingly. Alternative constitutive relations of inter-phase coefficients have also been used in the literature.

Continuity equation:

$$\frac{\partial(\varepsilon_i \rho_i)}{\partial t} + \nabla \cdot (\varepsilon_i \rho_i \mathbf{u}_i) = \dot{r}_i \quad i = g, s \tag{2.12}$$

where ε_i and ρ_i are the volume fraction, density of phase *i*. $\mathbf{u}_i$ is the bulk velocity of phase *i*. $\dot{r}_i$ is the mass transfer into phase *i* due to reaction.

Species transport equation:

$$\frac{\partial(\varepsilon_g \rho_g Y_{g,j})}{\partial t} + \nabla \cdot (\varepsilon_g \rho_g \mathbf{u}_g Y_{g,j}) = -\nabla \cdot (\varepsilon_g \mathbf{J}_{g,j}) + \varepsilon_g \dot{r}_{g,j} \tag{2.13}$$

where $\mathbf{J}_{g,j}$ and $\dot{r}_{g,j}$ are the diffusive mass flux and the reaction rate of species j. $Y_{g,j}$ is the species mass fraction.

Momentum Equation

$$\frac{\partial(\varepsilon_i \rho_i \mathbf{u}_i)}{\partial t} + \nabla \cdot (\varepsilon_i \rho_i \mathbf{u}_i \mathbf{u}_i) = \varepsilon_i \rho_i \mathbf{g} - \varepsilon_i \nabla p + \nabla \cdot \boldsymbol{\tau}_i + \beta_B (\mathbf{u}_j - \mathbf{u}_i) + \dot{r}_i \mathbf{u}_i \quad i = g, s \quad j \neq i \tag{2.14}$$

where β_B is the drag force coefficient, and can be approximated according to ref. [99]. $\boldsymbol{\tau}_i$ is the stress tensor and $\mathbf{g}$ is the gravity.

Energy Equations:

$$\frac{\partial(\varepsilon_i \rho_i h_i)}{\partial t} + \nabla \cdot (\varepsilon_i \rho_i \mathbf{u}_i h_i) = \nabla \cdot (k_i \nabla T_i) + Q_i + S_i \quad i = g, s \tag{2.15}$$

where h_i is the enthalpy of phase *i*. T_i, k_i are the temperature, conductivity of phase *i*. S_i is the heat of reaction. $Q_g = -Q_s$ is the inter-phase heat transfer.

2.3.3 Cyclic process analysis

Various preliminary system designs for chemical looping power generation have been reported in the open literature. A summary is listed Appendix C. One of the most common designs is a combined cycle (CC) with the combustor replaced by CLC reactors (CLC-CC). Figure 2-11 ([6]) shows the simplified layout of the CLC combined cycle. The flue gas from the AR is used to drive the gas turbine, as in conventional CC. However, a secondary CO_2 gas turbine and steam turbine can be applied to extract the energy from the flue gas out of the FR. The gas turbine flue gas from the AR is used to drive the bottom steam cycle while the flue gas from the FR can be utilized to preheat the fuel. Similar designs have been proposed by Naqvi and co-workers [102, 103]. Several variations of the CC design have also been investigated. For instance, the pressurized flue gas from the FR can be directly used to drive the bottoming steam

cycle [104, 105] or be linked with the recuperator to preheat the compressed air [106], such that the CO_2 stream is not expanded, and the work of CO_2 compression is reduced. Figure 2-12 compares these three designs. The combined cycle with CO_2 gas turbine and steam turbine offers the highest efficiency while the characteristics of the other two (CC with recuperation, and CC with FR flue gas driving steam cycle) are almost the same.

Sensitivity analysis of the combined cycle [105, 106] showed that the oxidation reactor exit temperature is the parameter of paramount significance. The higher the oxidation temperature, the higher is the gas turbine inlet temperature (TIT) and hence the higher is the net plant efficiency. While modern gas turbine can operate at TIT values of 1400°C or above, there are limitations associated with the temperature inside the oxidation reactor of CLC. On the one hand, as discussed in Section 2.5, higher oxidation temperature will increase the risk of agglomeration and attrition and hence raise the maintenances cost. On the other hand, the higher oxidation temperature will result in stricter requirement on the reactor material towards high temperature and high pressure. The continuing development of oxygen carrier research may broaden the operation range that oxygen carriers can withstand, while the specially designed reactors equipped with lining of high-temperature resistant ceramic bricks can be a feasible solution towards the reactor material limit. Nevertheless, it is beneficial to explore other possibilities that would result in efficient CLC cycles operating on relatively lower and thus safer temperatures. One potential option is to utilize reheating to decrease the oxidation temperature while maintaining acceptable efficiency. Anheden and Svedberg [107] proposed a single stage reheating CC using Ni-based OC with methane as fuel. The exergy destruction in the reactor is lower compared with conventional direct combustion, and hence the total efficiency is enhanced. Naqvi et al. [106] carried out a systematic comparison of the multi-stage reheating cycles, as seen in Figure 2-12. It was reported that single-stage reheating could achieve an efficiency around 51% with T_{ox} of only 1000°C whereas an oxidation temperature above 1200°C is necessary to obtain similar efficiency for CLC without reheating. At the oxidation temperature of 1200°C, single-stage reheating shows above 53% net plant efficiency. The double reheat CLC however, does not exhibit substantial efficiency improvement compared to the single reheat cycle.

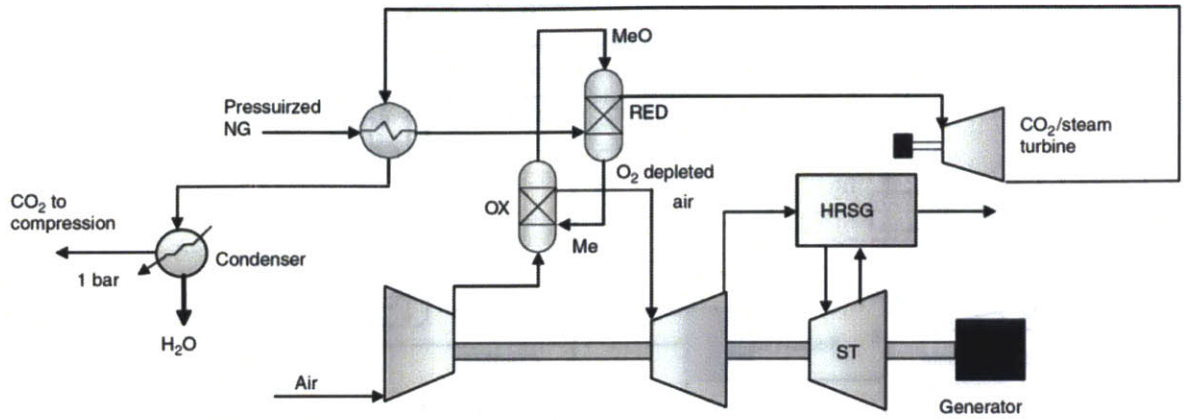

Figure 2-11 The cyclic flow diagram of chemical looping combined cycle.[6]

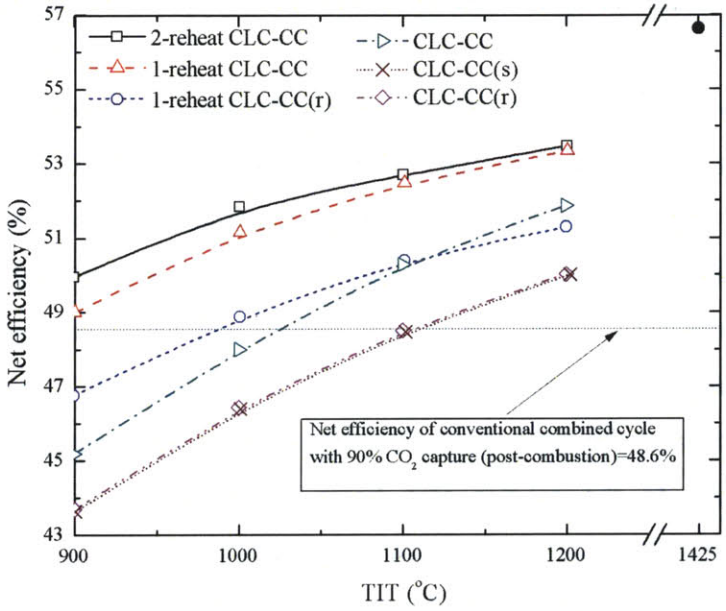

Figure 2-12 Comparison of multi-stage combined cycle designs [108]. Solid circle is for the combined cycle without CCS; CLC-CC(r) is the CLC combined cycle with FR flue gas recuperation; CLC-CC(s) is the CLC combined cycle with FR flue gas driving bottom steam cycle.

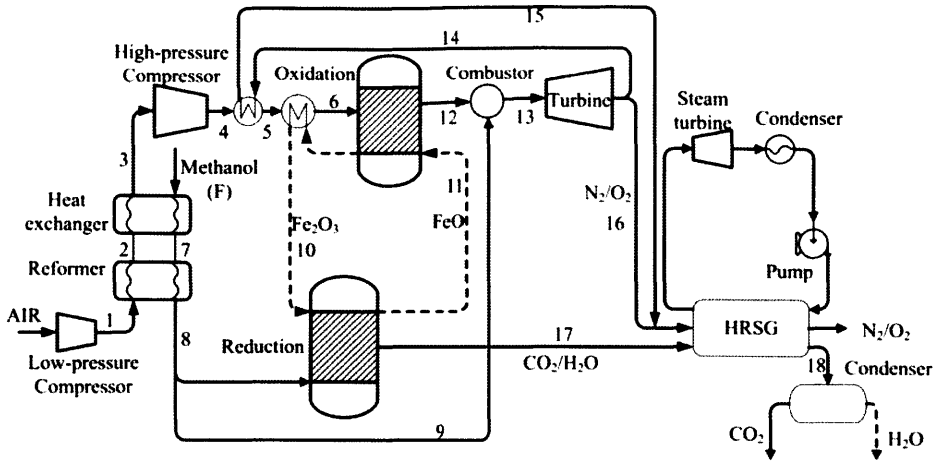

Figure 2-13 The cyclic flow diagram of the intercooled combined cycle using methanol as fuel. [109]

Another issue associated with CLC power generation is that as air flows across the AR, part of the oxygen is transferred to the OC. Therefore, only a portion of the compressed air is used to drive the gas turbine. In order to deliver certain amount of specific work output, a higher air intake rate is needed. Accordingly, the air compression work as well as the exergy destruction in the compressor increases which lowers the overall efficiency compared to conventional combined cycle. In order to cope with this issue, CLC cycles based on "humid-air cycle" concept can be utilized to enhance the total mass flow rate without increasing the compressor work. Besides, adding steam to the reactor also helps lower the reaction temperature. Several simulations of CLC have been carried out with integration of a saturator in the cycle. Ishida et al in 1987 [15] first proposed a "humid-CLC" cycle with fuel saturated by steam. It was reported that the saturation of methane with water recovers low-level thermal energy by evaporating the steam in a saturator using the exhaust gas. In addition, the added steam could facilitate the fuel decomposition (e.g. methane reforming). The flue gas from the FR contains only H_2O (from the reaction and from steam saturation) and CO_2 (from the reaction) and 90% water can be condensed because the gas is not diluted with air. An updated version was reported by Ishida and co-workers [16, 110] utilizing saturated air rather than saturated fuel. In contrast to conventional humid-air cycle in which the impurities from the exhaust (NO_x, CO_2) cause corrosion of the turbine blade, the separation of air from the fuel in the CLC humid-air cycle case has no corrosion problem. The overall efficiency of the humid-air CLC was reported to be over 55%, 2% higher than the multi-stage combined cycle. Similar results were reported by Brandvoll and

Bolland [111]. Comparison with the conventional combined cycle shows that the humid-air CLC has similar or even lower exergy loss and power requirement for the compression.

As mentioned before, CLC has advantages over conventional direct combustion in that the exergy destruction within the combustion is minimized. This has been validated in every cyclic exergy study [15, 16, 107, 109, 110, 112-115]. Thus in a power generation cycle integrated with CLC, it is possible to achieve higher efficiency compared to conventional power generation. However, as mentioned in previous section, the heat transfer between the gas streams and the solid may lead to large irreversibility if large temperature gradients exist. Thus special attention must be paid to the strategic energy management with proper preheating, recuperation, heat exchange between the oxidized and reduced solid oxygen carriers, etc., to minimize the exergy loss within the heat transfer. Jin and co-workers proposed a series of designs illustrating this aspect [109, 112]. Figure 2-13 shows an intercooled CLC combined cycle using methanol as a fuel. The heat released from the intercooler in conventional intercooled gas turbine, with a temperature range of 200-300°C, is usually wasted. However, in this design the heat can be utilized to evaporate and decompose liquid methanol into syngas and preheat the syngas towards reduction temperature, as seen in T-Q profile in Figure 2-14 (a). Another feature in this design is to install a heat exchanger between the preheated air (stream 5) and the oxidized oxygen carriers (stream 10). Therefore the compressed air can be further preheated close to the oxidation temperature and the oxidized oxygen carriers are cooled to the reduction temperature, as seen in Figure 2-14 (b). During these two processes, the temperature matching between the hot streams and the cold streams is a key factor. From Figure 2-14 we may see minimal temperature differences and hence the exergy destruction associated with the heat transfer process is minimized. The efficiency was reported to be over 59% with supplementary firing.

One other advantage of CLC is that it could transfer the energy from the low grade reduction reaction up to the high grade oxidation reaction and hence enhance the work output at high temperature level. This feature would provide a chance to utilize low temperature energy source, e.g., solar energy, geo-thermal energy or even exhaust gas from turbine, to drive the low temperature reduction, and utilize the high temperature flue gas from AR to power a turbine. A variety of solar-hybrid CLC cycle designs have been proposed by Hong and co-workers [113-115] based on this characteristic. Figure 2-15 shows the layout of the solar-hybrid CLC design using methanol as fuel. The solar energy input is used to supply reaction heat to the endothermic

reduction through which the energy is upgraded by OCs to the oxidation reaction which is at a much higher temperature. Preliminary calculation shows that the utilization of solar-hybrid design gives an overall efficiency above 57%. It is worth mentioning that by incorporating solar energy into CLC cycle, the solar-to-electricity efficiency can also be enhanced [113].

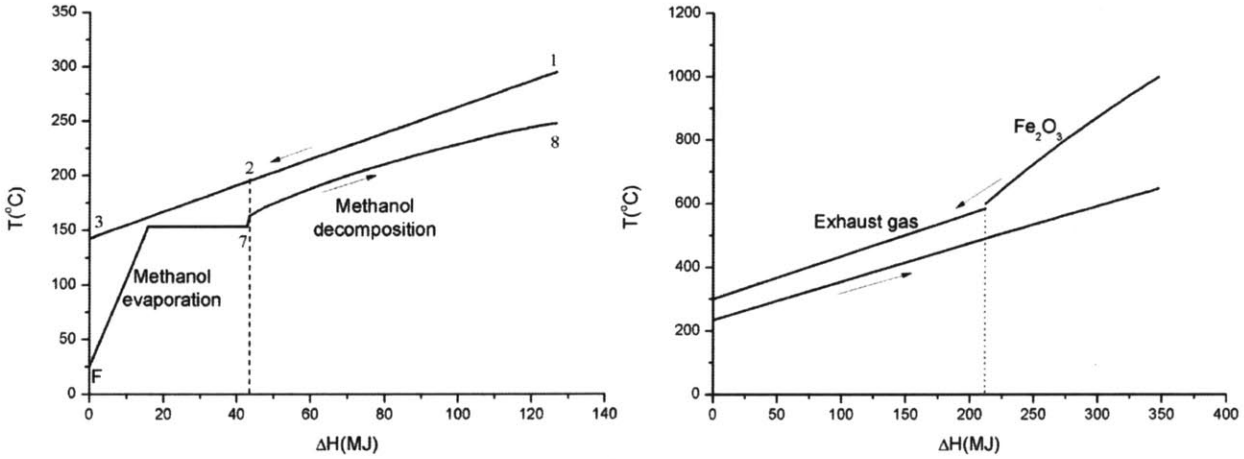

Figure 2-14 Temperature profile as a function of heat transfer for (a) methanol evaporation and decomposition and (b) exhaust heat recovery. [109]

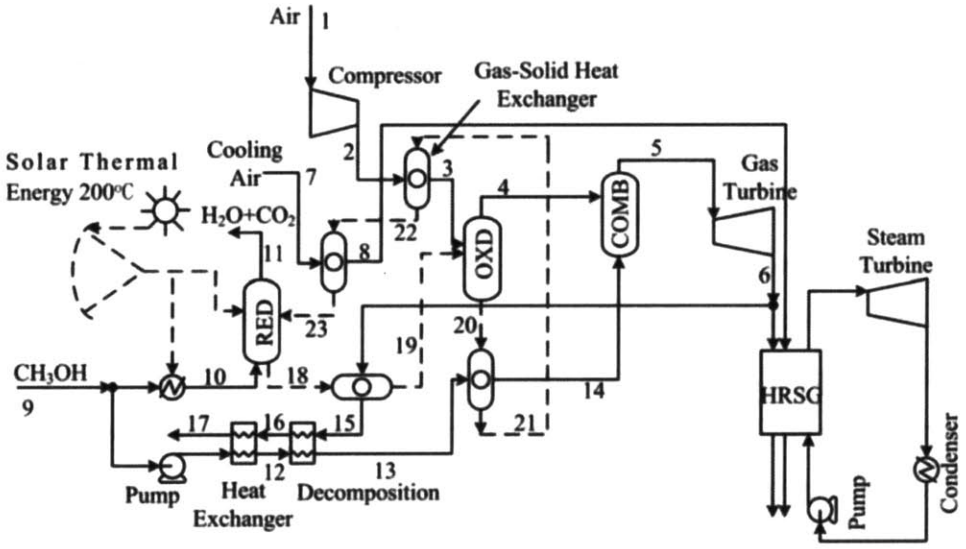

Figure 2-15 The cyclic flow diagram of the solar-hybrid combined cycle using methanol as fuel[113].

Chapter 3

Reactor Design

3.1 Introduction

As discussed in section 2, Appendix A and Appendix B, research on CLC so far has been mostly focused on utilizing an interconnected fluidized-bed reactor with oxygen carriers particles circulated throughout the reactors, as shown in Figure 2-4 (a). However, major drawbacks of this design are related to the particle circulation process: extra energy is needed to fluidize the beds and hence the pressure drop throughout the reactor is usually high; an efficient cyclone unit is required to separate the particles from the flue gas; fine particles must be removed before the flue gas entering gas turbine; agglomeration may happen; and particle collisions would impair the lifetime of the reactors. Moreover, significant nitrogen and CO_2 leakage can occur which leads to reduction of the capture efficiency or the need for extra separation downstream to purify the CO_2 stream. These issues are more severe under elevated pressures. Although a great variety of successful industrial applications using fluidized bed reactors have been built, the complexity of the multiphase, multi-scale reactive flow makes it difficult to design, optimize and scale-up the reactors.

Alternative designs, such as the moving-bed reactor (Figure 2-4 (b), [11, 83, 84]), the packed-bed reactor (Figure 2-4 (c), [85-87]) or the annulus rotating bed reactor (Figure 2-4 (d), [88]), have also been proposed and investigated. However, as discussed in Table 2-5, major issues still exist in each of these designs: the particle circulation problems in a moving-bed reactor; the technical difficulties associated with the effective control of extremely large volumes of gas under high temperature and high pressure in the packed-bed reactor; and the unavoidable mixing between the fuel and the air sector in the horizontal rotating reactor.

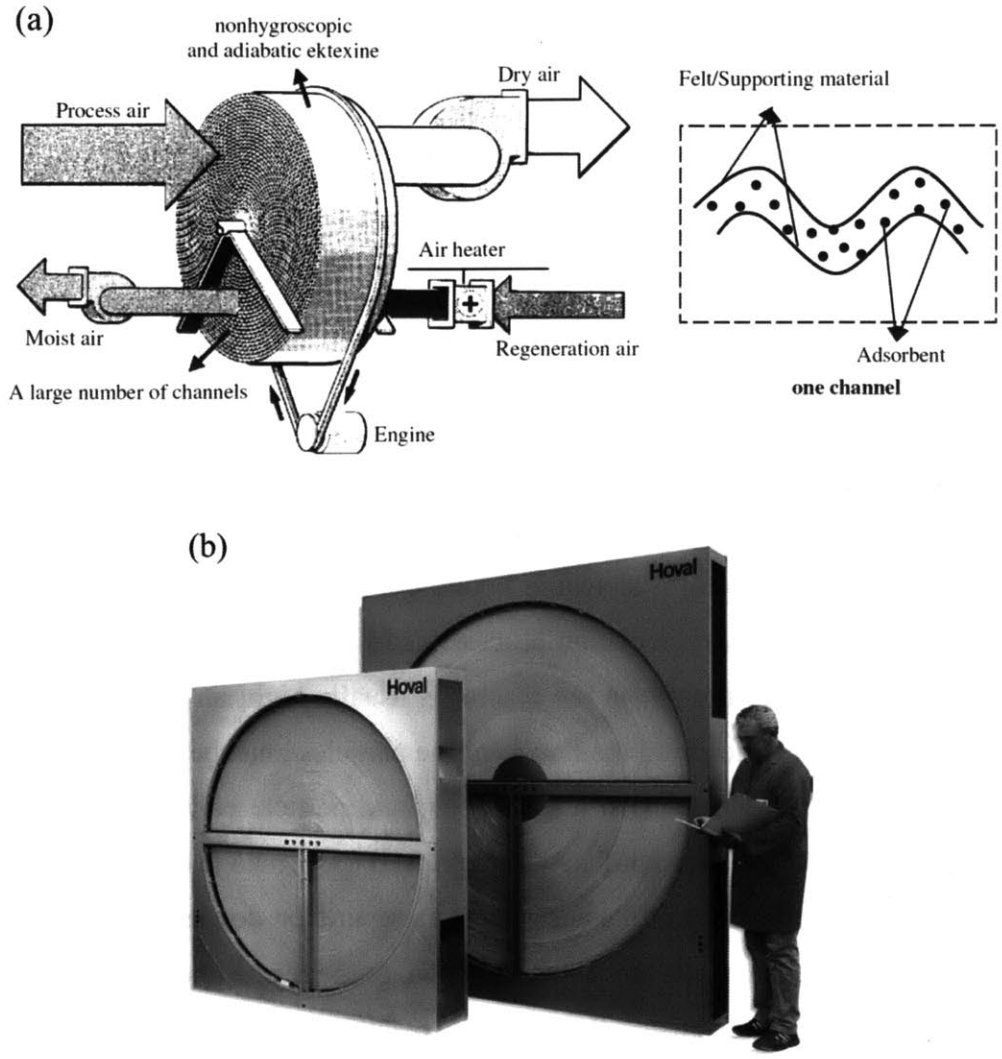

Figure 3-1 Schematic figure of (a) rotary desiccant wheel [116], and (b) rotary regenerative heat exchanger [117].

An innovative method of chemical-looping combustion is described in this study. It is based on the rotary bed reactor technology, where a solid matrix wheel rotates between the reducing and oxidizing environments. The main advantages of a reactor concept based on the rotary reactor technology are that the separation of the gas and particles are intrinsically avoided, the operation is continuous and while cyclical, it is stationary. Moreover, the reactor design can be more compact and easier to scale-up. The idea of a rotary chemical-looping reactor system is based on two innovative applications of rotary technology:

- **Rotary desiccant wheel** (Figure 3-1(a)): a desiccant wheel matrix consists of a large number of channels with walls constructed of supporting material coated or impregnated

with desiccant material. The desiccant material adsorbs water vapor when moist air passes through the process air side, and it is regenerated when it desorbs water while heated air flows through the regeneration side [116].

- **Rotary regenerative heat exchanger** (Figure 3-1(b)): The rotary heat exchanger transfers heat between a high pressure low temperature feed gas and a low pressure high temperature flue gas. As the wheel rotates between the cold and hot streams, only heat is transferred through solid matrix. An effective sealing system, which could avoid the mixing between low pressure flue gas and high pressure inlet air, is needed to reach a high efficiency [117-121].

The rotary bed reactor is a promising option for chemical-looping combustion. It combines the basic elements of a rotary desiccant wheel and a rotary regenerative heat exchanger. The oxygen carrier, rather than the desiccant material, is coated or impregnated on the surface of the spinning wheel matrix in a way similar to that in the desiccant wheel. As the reactor rotates, oxygen is absorbed while the channels pass through the air section, temporarily stored in the oxygen carrier, and then released to oxidize the fuel. During the cyclic operation, the solid wheel also behaves as a heat exchanger to transfer the reaction heat to the flowing gas. Effective sealing systems can be adapted from the rotary regenerative heat exchanger to avoid dilution. Several key challenges could be resolved based on the experiences from previous industrial applications of rotary bed reactors. One distinction though is the high temperature operation of the rotary reactor. Special attention must be paid to the differential thermal expansion associated with the reactor and the container, as will be discussed in section 5.4.

A similar idea of utilizing a rotary reactor for chemical-looping combustion was briefly suggested before. Pavone and co-workers [122, 123] discussed the possibility of utilizing chemical-looping redox (reduction-oxidation) chamber within a Brayton cycle, as seen in Figure 3-2. The redox performance of one channel was simulated using a commercial CFD package for the first 25 seconds (three cycles). Unburned fuel was observed at the outlet. For a carbon capture efficiency of 90%, the energy penalty is 15% of the power output without CO_2 capture. However, little discussion was given regarding the reactor design, cyclic performance or operating conditions. The research on this subject was terminated because of leakage and safety concerns. Cichanowicz and Muzio [124] extended the rotary idea to a Rankine cycle utilizing

solid fuel with a counter-current flow pattern in the reactor. Coal particles enter the chamber channel and undergo a series of complex reactions, e.g. de-volatilization, pyrolysis and char oxidation, generating syngas which is then oxidized by the oxygen carriers along the channel. However, a major barrier in this design is that the ash particles tend to stick to surfaces, which may lead to blockage and surface erosion. In addition, the burnout time needed for solid fuel is generally much longer than that for gaseous fuel such that a highly sophisticated post-possessing system is needed to remove unburned char particles.

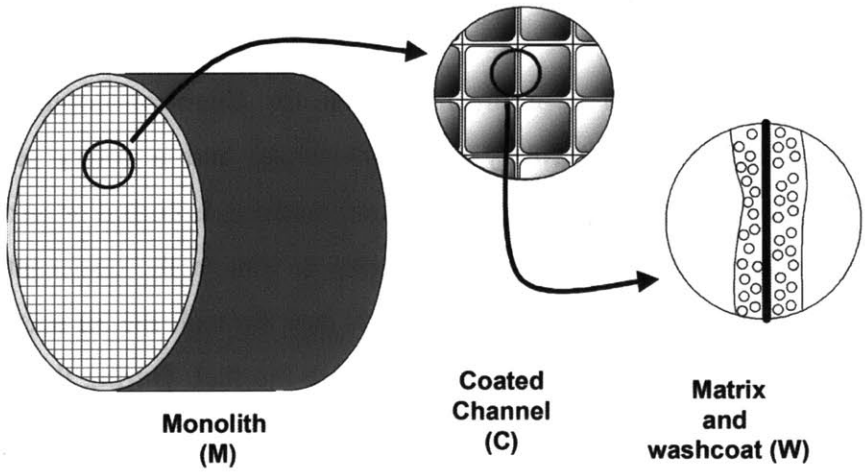

Figure 3-2 Schematic drawing of chemical-looping redox chamber with CO_2 recovery. [122, 123].

In this chapter, detailed descriptions of the reactor design, sector arrangement, material construction, functionality, and operating conditions of the rotary bed reactor are presented.

3.2 Reactor Design and Specification

The rotary bed CLC reactor consists of a rotary bed matrix, a driving motor, and two stationary gas chambers located at the top and bottom of the wheel (inlet or outlet), as shown in Figure 3-3(a). Pressurized feed gas flows in a co-current pattern from the bottom feeding chamber, reacts with the oxygen carrier as it passes through the rotary bed and leaves the system from the top exit chamber. The heat generated from the exothermic reactions is utilized to heat the passing gas to high temperature, which is ultimately used to drive turbines to generate electricity. The solid wheel temporarily stores the heat from reaction and releases the heat to the flow. The rotary bed, powered by the driving motor, rotates at a constant speed while the feeding

chambers remain stationary. The entire reactor is surrounded by insulation walls that could sustain high temperatures and high pressures (as shown in Figure 3-3(b)). For clarity, the insulation walls of the reactor wheel are not shown in Figure 3-3(a). Figure 3-3(b) shows the cross-sectional view of the reactor. The rotary bed matrix consists of an array of identical long and narrow channels. A typical channel size is several millimeters wide depending on the cell density. The flow in the channel is generally laminar. The oxygen carriers are coated or impregnated onto the inner surfaces of each channel. Two streams of gas are admitted into the spinning channels from the feed side and leave the wheel from two different zones divided by insulation walls in the exit chambers. As the channel passes through the fuel zone, gaseous fuel stream flows into the channel, reacts with the active metal oxide to generate CO_2 and H_2O. As the same channel passes through the air zone, air flows into channel to fully regenerate the oxygen carrier back to its original state. Gas streams in the fuel and air zones are at the same pressures. The chemical energy from the continuous redox (reduction and oxidation) reactions is transferred to the channel wall by the convective flow through the rotating matrix, which behaves in a similar way as in the rotary heat exchanger. The center of the rotary bed is a small hollow channel through which a cylindrical bearing is inserted to support the reactor construction and actuation. The design is not limited to the co-current flow pattern. For example, a counter-current flow pattern with fuel (or air) flowing from top chamber to the bottom chamber can be an alternative option.

Figure 3-4(a) shows the bottom view of the gas feeding chamber. The feed chamber is divided into four sectors: a fuel sector (θ_{fuel}), an air sector (θ_{air}), a fuel purging sector (θ_{fuel_purge}) and an air purging sector (θ_{fuel_purge}). The fuel zone is divided into fuel and fuel purging sectors while the air zone is divided into air and air purging sectors. Fuel gas or air is fed into the fuel or air sector, respectively, while steam is used as a "sweeping" gas in the purging sectors to flush the reactor and hence avoid gas carry-over between sectors. The four sectors at the bottom chamber are separated by insulation walls which remain stationary during operation. Figure 3-4(b) shows the isometric projection of the reactor wireframe. The top exit chamber consists of a fuel sector and an air sector. While one slug of feed gas passes through a channel, the reactor bed spins continuously. Accordingly, flue gas exits at the same radial location of the wheel at a slightly different angle. The two purging sectors acts as a "buffer zone" to account for this angle mismatch. Therefore, as one channel spins out of the fuel (or air) sector and enters the following

purging sector, a feed steam continuously flushes the residual fuel (or unburned air) into the same zone at the top without diluting the other zone. Due to rotation, some steam from the fuel (or air) purging sector may also end up entering the following air (or fuel) sector.

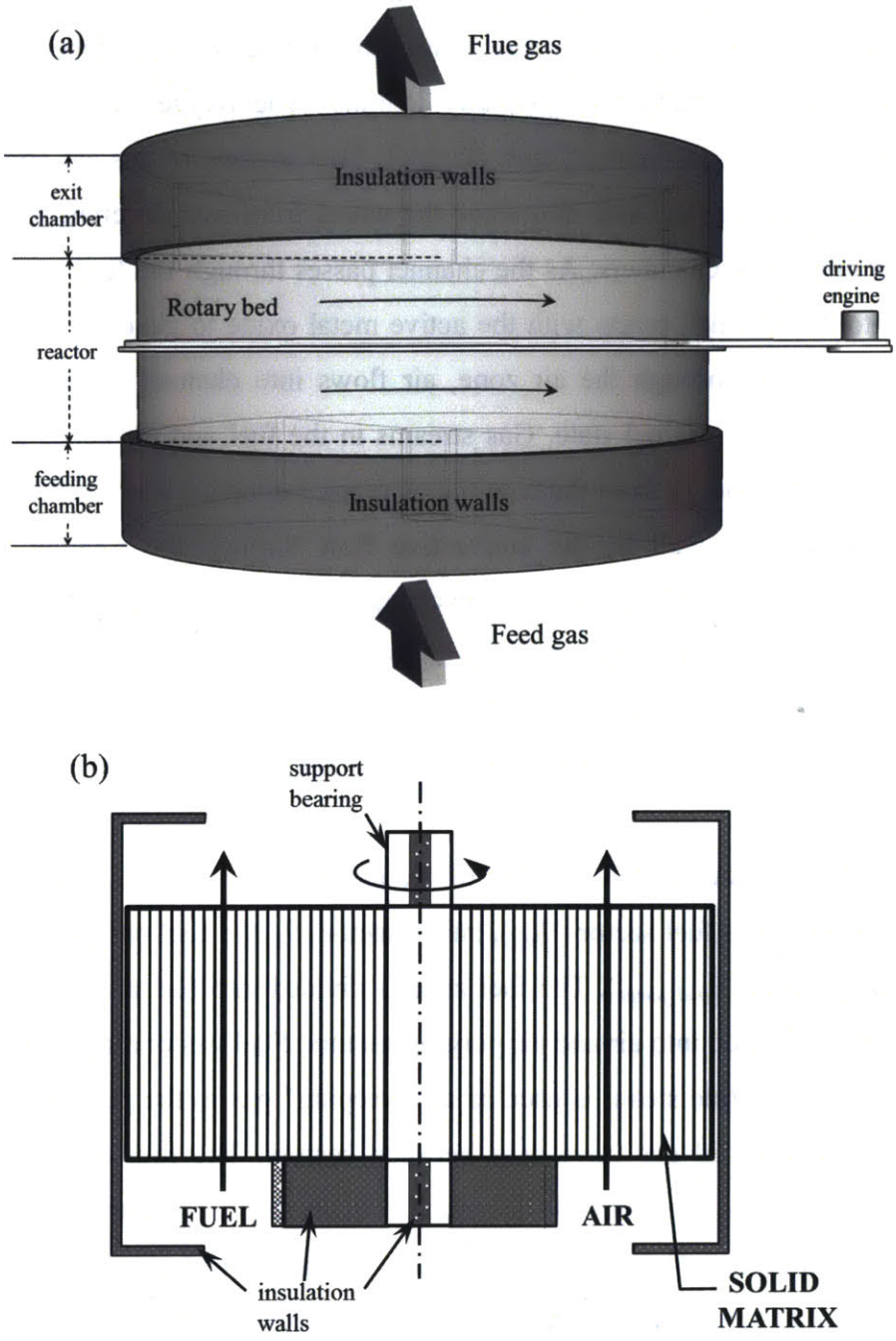

Figure 3-3 Schematic diagram of rotary CLC system design with (a) front view (b) cross-section view.

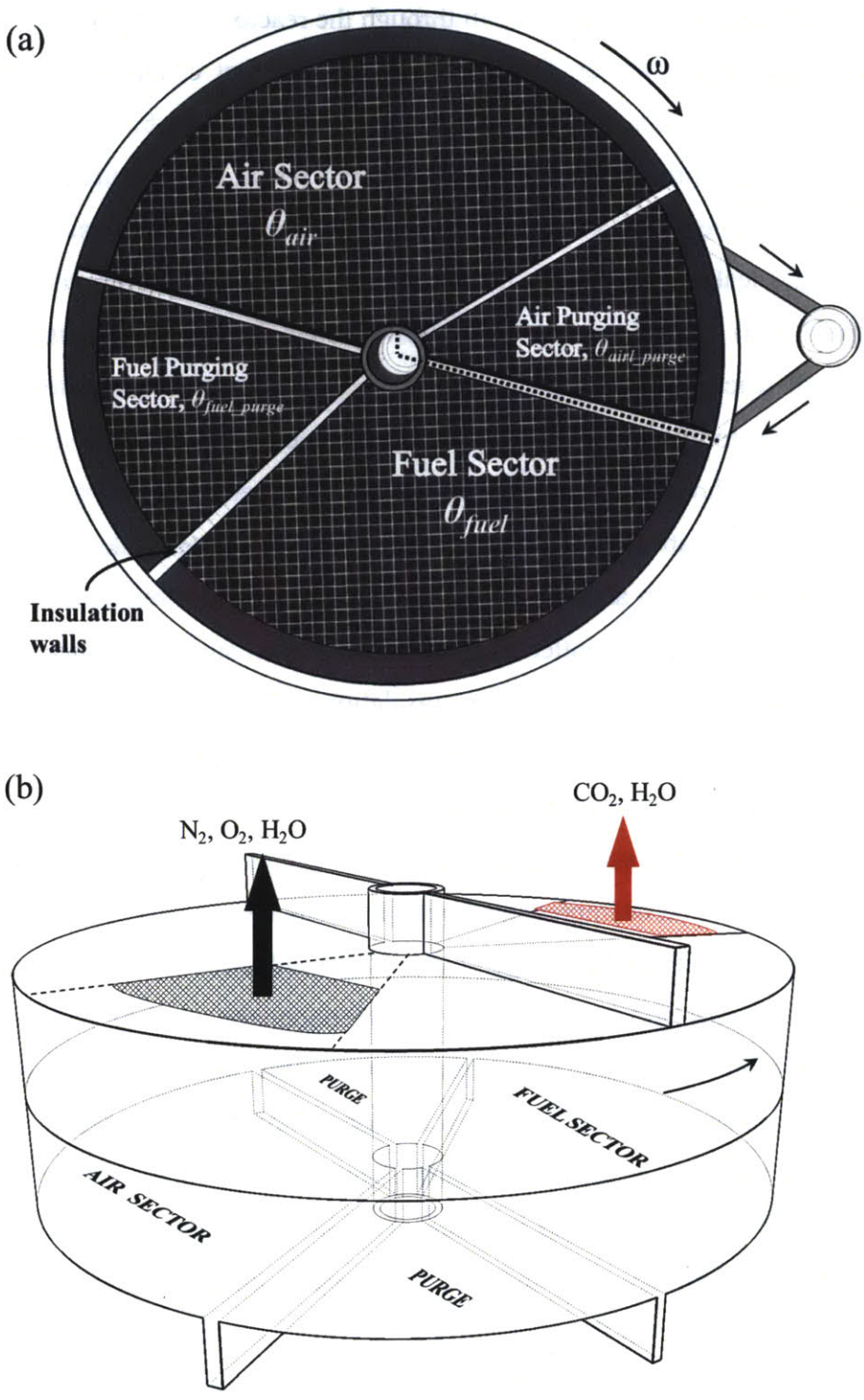

Figure 3-4 Schematic drawing of rotary CLC system design with (a) bottom view, and (b) the isometric projection of the wireframe.

Figure 3-5 shows the gas flow pattern through the reactor. The majority of feed gas enters the reactor from the feed chamber, flows through the different channels, and then leaves the reactor from the exit chamber. Pressure drop along channel is attributed to the skin friction, which is generally small for a laminar channel flow. As a result, the pressure differences between different sectors are expected to be small and hence the pressure-driven gas leakage is limited. However, some gas leakage may occur due to spinning motion of the reactor. For instance, as shown in Figure 3-5(a) and (b), some gas may flow through the gap between the insulation walls and the peripheral reactor surface and leave the reactor without being reacted; some gas may bypass from fuel zone to the air zone through the gap between the insulation separation walls and the rotating reactor, as shown in Figure 3-5(c) and (d). However, sealing systems similar to those used in the rotary regenerative heat exchanger can diminish the gas leakage (as seen in Figure 3-5): peripheral seals will trap and force the flow into centrifugal motion and hence restrict the gas bypass from the inlet to the outlet side; radial seals with small clearance can significantly reduce the gas leakage rate between stationary insulation walls and the moving reactor.

The rotary bed matrix consists of a large number of channels. Each channel consists of an inner gas passage and solid support material coated with the oxygen carrier, as shown in Figure 3-6(a). Gas flows through the passages and reacts with the oxygen carrier on the inner surface. The oxygen carrier is coated or impregnated onto a porous layer of the solid support, as seen in Figure 3-6(b). High porosity of the oxygen carrier layer enhances the surface area between the solid and the gas species and hence favors the heterogeneous surface reactions. The binder material in the porous layer acts as an oxygen-permeable material that helps improve the physical and chemical stabilities of the oxygen carrier and therefore maintains its reactivity after repeated cycles. In addition, as shown in Figure 3-6(b), a bulk support layer is bonded to the porous layer. This bulk support layer is made of highly conductive materials with high heat capacity, which can effectively store the heat produced in the exothermic reaction, transfer it within the reactor, and heat up the flowing gas. Consequently, the utilization of bulk support layer is critical to the temperature uniformity of the reactor. Besides, the bulk layer helps avoid the gas mixing between the adjacent channels. Note that the support material in the porous layer and the bulk layer is not necessarily the same.

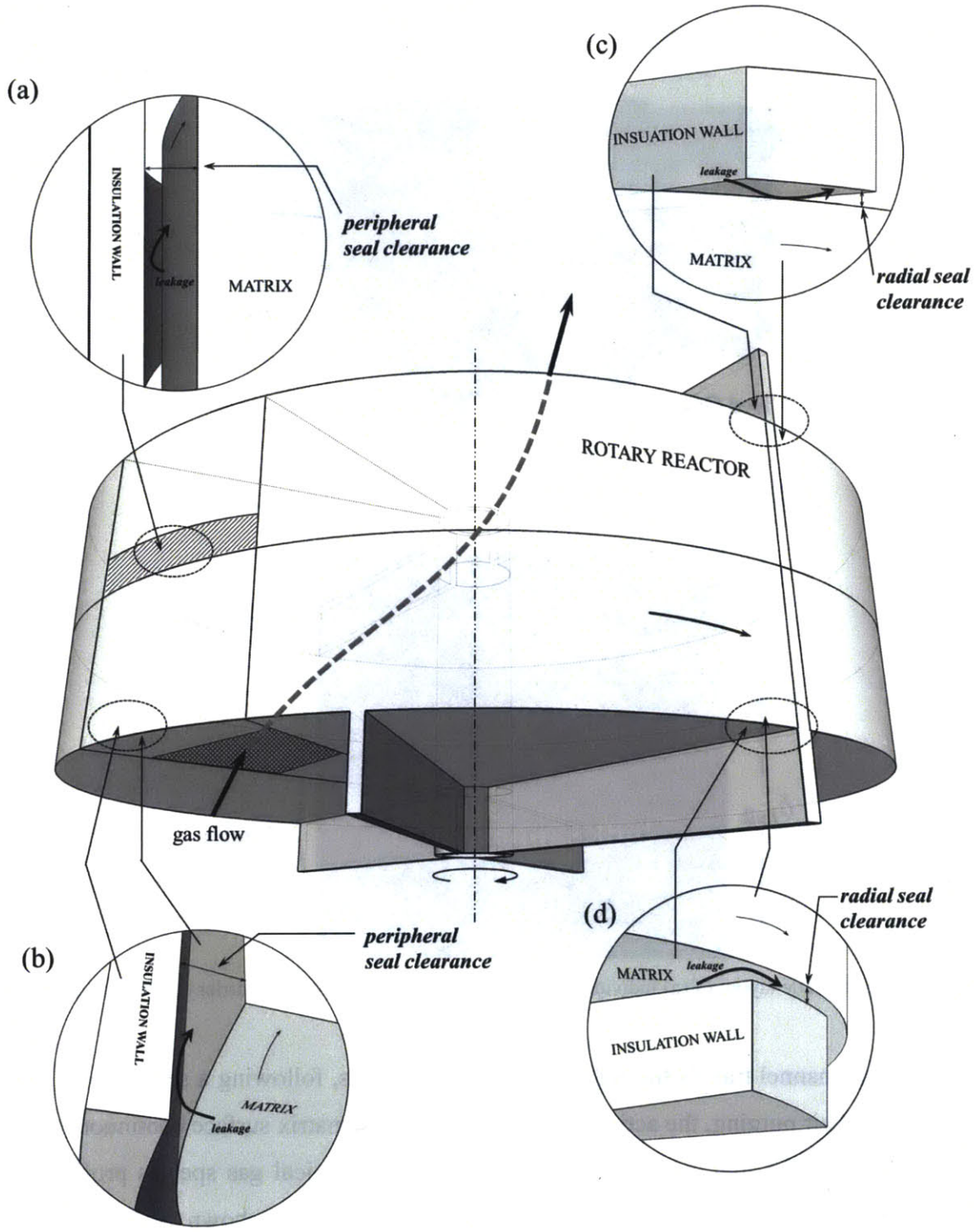

Figure 3-5 Schematic drawing of gas flow pattern through reactor and gas leakage through radial seals and peripheral seals. (a), (b) Peripheral seals prevent leakage between the insulation walls and the peripheral surface of the reactor. (c), (d) Radial seals restrict leakage between the insulation walls and the top and bottom surfaces of the reactor.

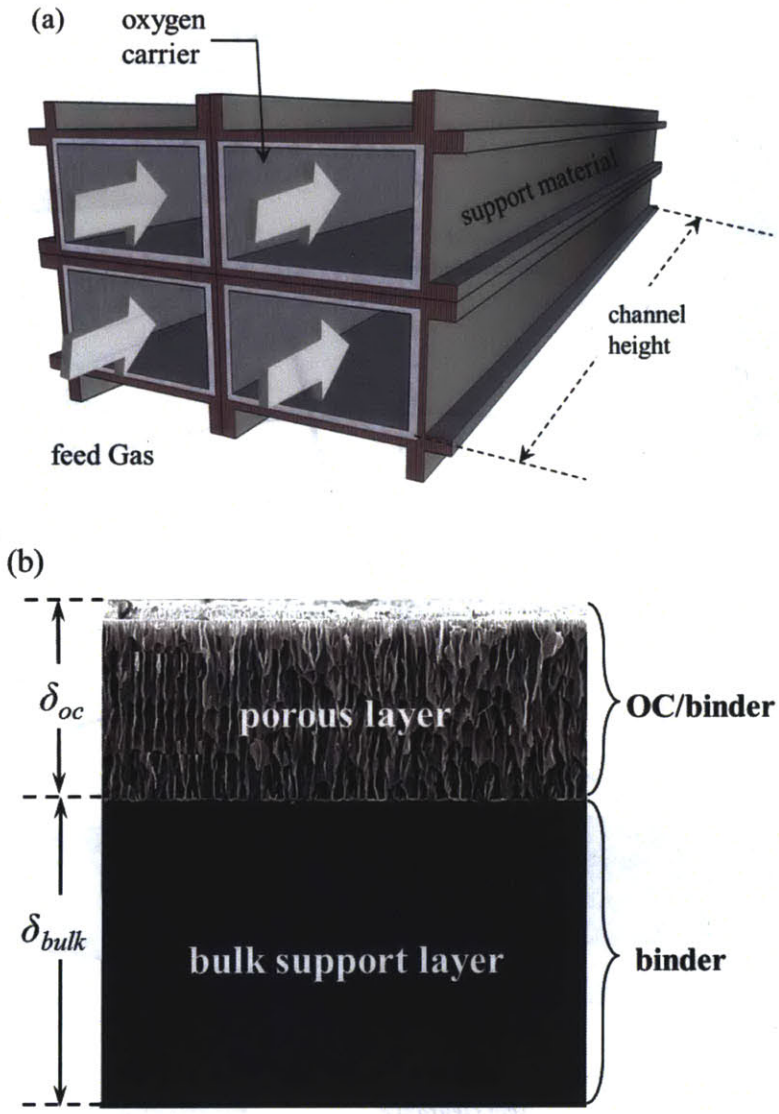

Figure 3-6 Schematic layout of (a) individual channel structure and (b) oxygen carrier coating on the surface.

As one channel travels through the fuel and air zones, following a sequence of fuel, fuel purging, air and air purging, the active oxygen carrier on the matrix surface continuously releases oxygen to oxidize the fuel, and absorbs oxygen from air. Typical gas species profiles for two consecutive cycles at the inlet and the outlet of one channel are shown in Figure 3-7 . The thermal and chemical state in one channel undergoes a transient process: gas species enters the channel, absorbs or releases oxygen from the oxygen carrier material, releases or absorbs energy with the reactor matrix, and leaves the reactor with a varying flow velocity and concentrations. Given constant inlet conditions during operation, as shown in Figure 3-7 (a), it is expected that after a number of cycles, the reactor will gradually converge to a periodic-stationary state: the

physical and chemical processes within one cycle will go back to the original states after one cycle. The compositions at the exit of the reactor at stationary state are shown in Figure 3-7(b). Therefore, the sum of a large number of transient flue streams exiting from the fuel sector (or air sector) will mix well to give one steady-state flue stream. The steady separate streams from the fuel sector and air sector can then be utilized to drive the gas turbine, as shown in Figure 3-8, and CO_2 can be easily separated after water condensation. The following analysis will mainly focus on this periodic-state behavior.

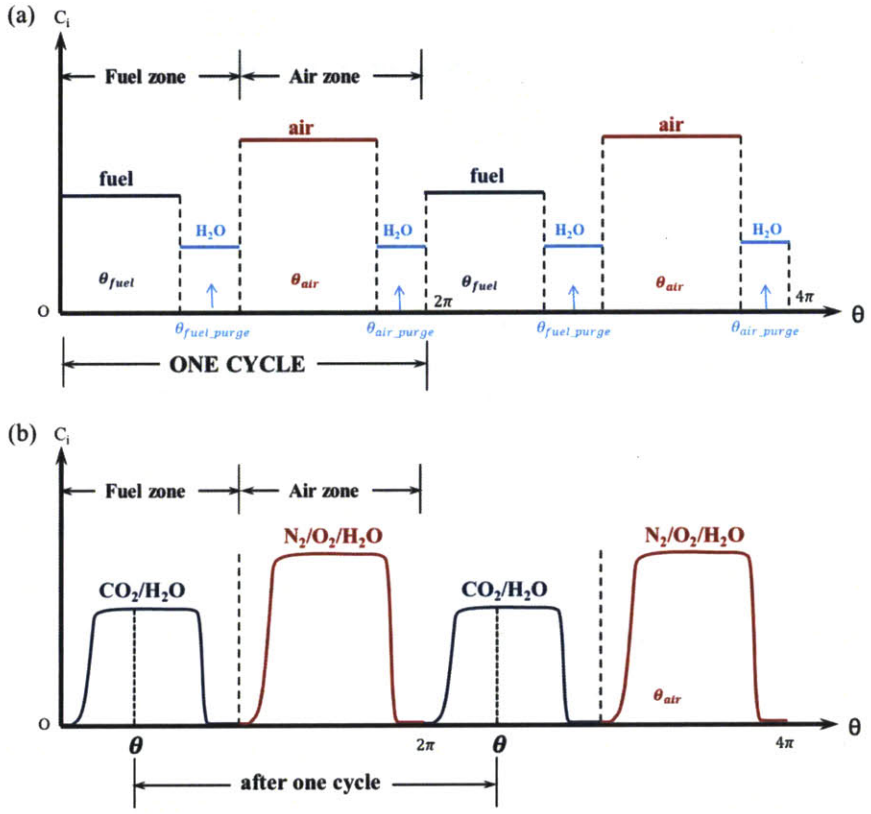

Figure 3-7 Schematic profiles of gas species concentration (a) at inlet and (b) at the exit for two cycles. Each cycle includes fuel, fuel purging, air and air purging sectors.

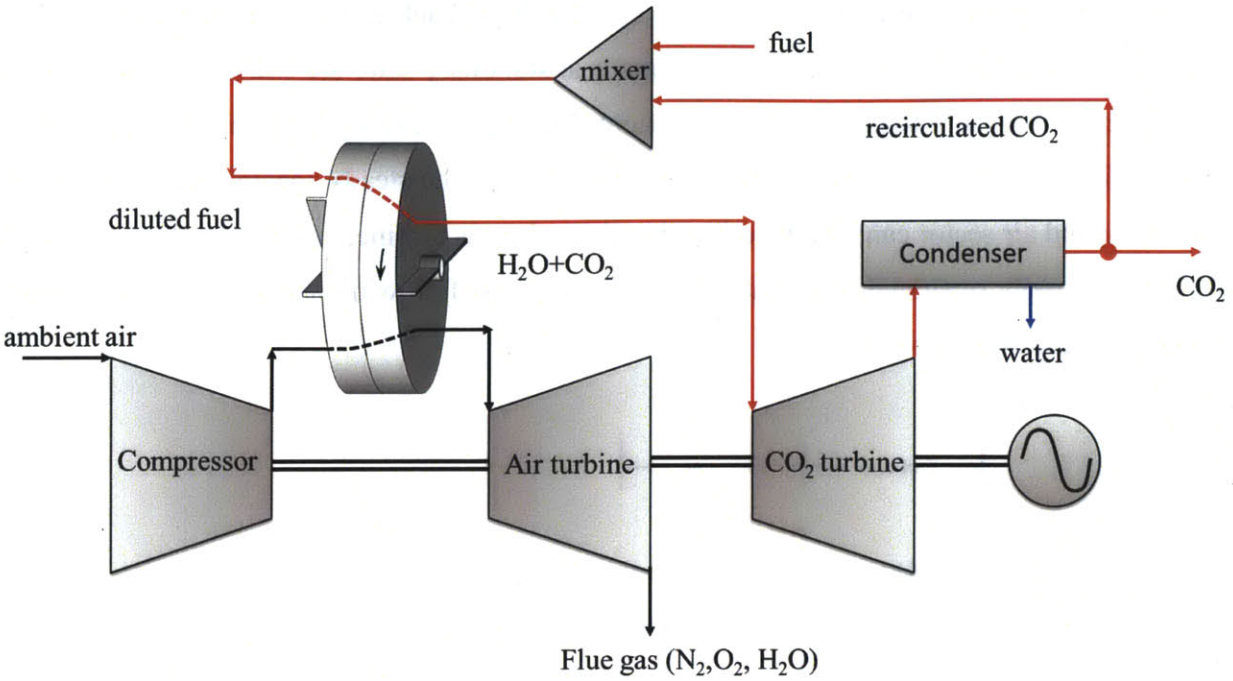

Figure 3-8 Simplified layout of the rotary chemical-looping combustion cycle. The red lines show the carbon flow pattern through the system. The feed purge streams are excluded in this layout for clarity.

A brief comparison between the proposed rotary reactor and other reactor candidates is presented in Table 2-5. The rotary reactor's merits are its ability of reaching high fuel conversion and carbon separation efficiencies, its compactness, and the feasibility of scale-up. Utilizing a rotating wheel with regulated flows gives rise to the possibility of performing chemical-looping combustion without complex gas-solid fluidization, and makes the most of the physical and chemical properties of the solid materials (heat capacity, conductivity, etc.). A specially designed channel with a combination of a highly porous oxygen carrier layer and a highly conductive bulk support layer favors the heterogeneous oxygen absorption and desorption reactions and should maintain an effective overall temperature control within the reactor. The pressure drop within the reactor should be small, and a uniform pressure distribution should be expected. Since direct solid-solid interactions are avoided, the solid attrition should be also limited. Thus, the proposed rotary reactor could be an alternative option for the chemical-looping combustion.

3.3 Design Criteria

The rotary reactor design should satisfy a number of criteria including complete fuel conversion, carbon separation, and operational stability. High fuel conversion and high carbon separation efficiency are the most fundamental requirements for CCS. Additionally, operational stability ensures a steady periodic performance and thus a long operational lifetime and a low operating cost for the power generation. The operational stability includes thermal, mechanical, and chemical stability: temperature variation with time should be limited such that the thermal expansion and distortion associated with temperature gradient are limited; solid support material must be mechanically robust such that it is effectively resistant to agglomeration, sintering or cracking during operation; high redox reactivity of the oxygen carrier should be maintained for many cycles while minimal reaction should occur for the support material. Therefore, the discussion of the reactor design parameters and operating conditions is primarily based on these three design criteria.

A variety of parameters can be specified to achieve the above design criteria. These design parameters and operating conditions can be categorized into three parts:

(1) *Material selection* (Table 3-1): OC, supporting material, surface treatment and coating.

(2) *Reactor configuration* (Table 3-2): shape, size of channel, arrangement of sector, seals;

(3) *Operating condition* (Table 3-3): temperature, pressure, rotational velocity, feed velocity.

The reactor design is not limited by the materials used as oxygen carriers/support, or the preparation method. Any of the materials or preparation methods described by Adanez et al. [81] are potential candidates for this rotary design, as well as other materials studied by numerous other investigators, which include, for example, in reduced metal form, Fe, Cu, Mn, Co, Ni, etc. The support material can be any material conventionally utilized as ceramic insulators: Al_2O_3, YSZ, TiO_2, BN, and etc. The preparation method includes, for example, wet-impregnation, dry-impregnation, deposition-precipitation, wash-coating, etc. Surface treatment methods, such as surface-etching, can be utilized to enhance the surface porosity and improve oxygen carrier load. In addition, the channels can be formed in a variety of geometry or sizes, such as, grid-type, honeycomb geometry shapes, plate-types, any series of corrugated shapes, or any type of geometry that presents a high specific surface area. Besides, the reactor can be operated at different pressures, temperatures, flow velocities, and so on.

Table 3-1 Properties of the oxygen carrier and support materials utilized in the base case

	Symbol	Value	Unit
Oxygen carrier	CuO	copper oxide	
Support material	BN	boron nitride	
density of bulk support layer	ρ_s	3450	kg/m^3
porosity of porous OC layer	ε_s	0.57	
conductivity of support	k_s	740	W/(mK)
active CuO load	wt%	10	-
volume fraction of CuO in OC layer	ε_{CuO}	0.0281	-
volume fraction of Cu in OC layer	ε_{Cu}	0.0161	-
pre-exponential factor for reduction (Eq. (4.10))	$k_{0,CH4}$	1.125×10^6	$mol^{0.6}\ m^{-1.8}\ s^{-1}$
pre-exponential factor for oxidation (Eq. (4.11))	$k_{0,O2}$	2.043×10^4	$mol^{0.0}\ m^{0.0}\ s^{-1}$
activation energy for reduction (Eq. (4.10))	E_{CH4}	60	kJ mol^{-1}
activation energy for oxidation (Eq. (4.11))	E_{O2}	15	kJ mol^{-1}
pressure coefficient for reduction (Eq. (4.10))[1)]	a_{CH4}	0.83	-
pressure coefficient for oxidation (Eq. (4.11))	a_{O2}	0.68	-
reaction order for reduction (Eq. (4.10))	n_{CH4}	0.4	-
reaction order for oxidation (Eq. (4.11))	n_{O2}	1.0	-

[1)] The coefficient is for CuO reduction with CO. There is no available data for CH_4.

Table 3-2 Reactor design and configurations for the base case

	Symbol	Value	Unit
channel side size	d	2	mm
channel length	H	1.3	m
reactor diameter	D	1.6	m
thickness of solid (support and OC layers)	δ_s	260	μm
thickness of porous OC layer	δ_{oc}	50	μm
size of air sector	θ_{air}	$\pi/3$	rad
size of fuel sector	θ_{fuel}	$11\pi/8$	rad
size of air purge sector	θ_{air_p}	$\pi/12$	rad
size of fuel purge sector	θ_{fuel_p}	$5\pi/24$	rad
size of air zone	θ_{air_zone}	$5\pi/12$	rad
size of fuel zone	θ_{fuel_zone}	$19\pi/12$	rad

Table 3-3 Operating conditions for the base case

	Symbol	Value	Unit
operating pressure	P	10	*atm*
fuel inlet temperature	T_{fuel}	823	*K*
air inlet temperature	T_{air}	823	*K*
purging steam temperature	T_{purge}	823	*K*
volume fraction of fuel at inlet	vol%	7.5	-
cyclic period time	τ	48	*s*
air flow velocity	u_{air}	1	*m/s*
fuel flow velocity	u_{fuel}	0.15	*m/s*
steam velocity of fuel purging sector	u_{fuel_p}	0.3	*m/s*
steam velocity of air purging sector	u_{air_p}	1	*m/s*

Velocities are evaluated at operation temperature

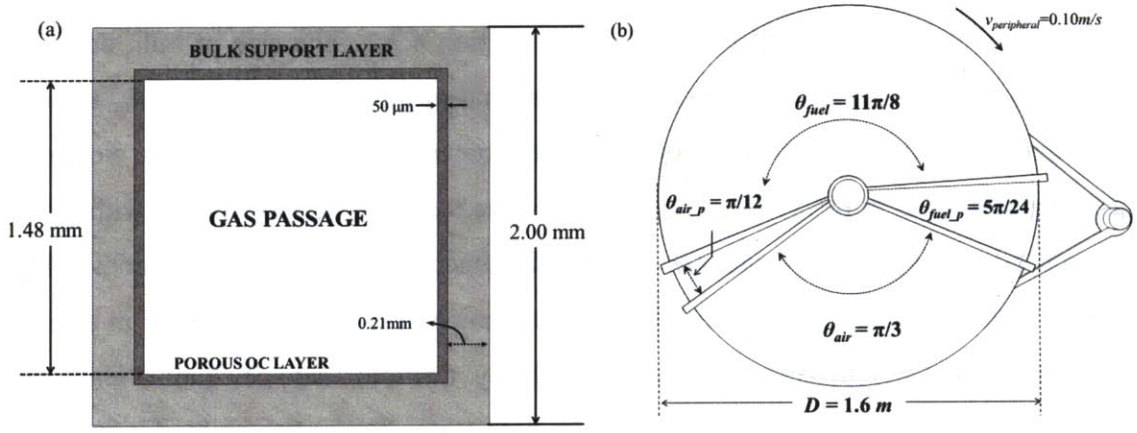

Figure 3-9 The design configuration of the reactor: (a) the channels and (b) the sectors.

The above parameters are highly coupled, and they are all closely related to the performances of the reactor. For instance, highly reactive oxygen carrier material, effectively coated porous layer, or simply a long enough channel with a small cross-sectional area all lead to high redox reactivity and thus a high fuel conversion. The CO_2 separation efficiency is directly determined by the purging gas velocity through the channel, the residence time in each zone, and the size and porosity of the channel. Furthermore, the operational stability is closely related to almost all design parameters: the oxygen carrier, preparation method, size of channel, temperature, pressure, gas flow rate, etc., which all affect the reactivity and influence the heat balance within reaction; the selection of support material and the geometry of the channel

determines the thermal inertia, mechanical strength, and chemical regenerability of the reactor; the arrangement of the purging sector, and the sealing systems are closely related to the fuel/air separation and thus the safety of the reactor, etc. The reactor design is complex and it involves the comprehensive consideration of all the aspects above.

Table 3-1 through Table 3-3 and Figure 3-9 show typical design parameters for the reactor considered in this work. Copper is utilized as the oxygen carrier due to its high reactivity and low tendency for carbon deposition, oxygen capacity and relative low cost [7] while boron nitride (BN) is used as support material for both layers due to its key properties resulting from its crystalline structure, such as high thermal conductivity, low thermal expansion, effective thermal shock resistance, and high chemical stability in oxidizing environment. The bulk dense support layer (260 μm) is pre-treated by surface etching, and then coated with copper nitrite by wet-impregnation to form a thin porous oxygen carrier layer (50 μm). The thickness of the porous oxygen carrier layer is the same as that utilized in ref. [122] and it is also related to OC kinetics experiments in ref. [125], as will be discussed in section 4.3.3. The size of bulk dense support layer ($\delta_s - \delta_{oc}$) is one order of magnitude larger than that of the OC layer $(1 - \varepsilon_s)\delta_{oc}$ to ensure the thermal regenerability. The active oxygen carrier content is around 10% (by weight) in the porous layer similar as in ref. [125]. The channel of the reactor is square-shaped with side size of 2.0mm and hence the flow through the channel is generally laminar. The channel side size is larger than that utilized in ref. [122] (0.5mm). The choice of channel cross-section size is based on the consideration of reactivity and periodic stability: a smaller size of channel leads to higher reaction rates but a larger temperature variation with time. The entire reactor is pressurized at $10atm$. The selection of the operating pressure is based on the experiences in a non-ideal Brayton cycle considering the impact of the compressor and turbine efficiencies on the cycle efficiency and the specific work [126]. The operation temperature ranges from 823K to 1245K. The fuel is diluted with recirculated CO_2 to lower the operating temperature below the material limits of gas turbine. The size of the reactor (diameter, height) is configured to ensure complete fuel conversion with a primary thermal capacity of 1MW. The angles of sectors and the rotational velocity are selected to provide enough residence time for complete oxygen carrier regeneration, complete purging of residual fuel (or air) and also avoid the complete reduction of the oxygen carrier in the fuel sector. The performance of the reactor is evaluated based on the simplified model as will be discussed in the next chapter.

Chapter 4

Numerical Modeling of Rotary Reactor

4.1 Model Description

The modeling of the rotary reactor starts with analyzing an individual channel during a full cycle. As the wheel rotates at a constant angular velocity, each individual channel experiences the same identical sequence of events: reduction in the fuel zone, purging of the fuel stream; regeneration in the air zone followed by the purging of the left-over air stream. All channels have the same residence time in each sector. Thus, in the preliminary analysis, we can reasonably neglect the radial variations among different channels in the reactor and only focus on one channel while changing inlet conditions. The channel in the rotary reactor typically has a very high height to equivalent diameter ratio (H/d = 650, as seen in Table 3-2). Therefore, using a one-dimensional plug flow model with the mass and heat transfer between the solid and the gas flow should be able to characterize the physical and chemical processes within the channel.

The model includes both the gas phase and the solid phase, as shown in Figure 4-1. The flow inside the channel is laminar ($Re_d = \rho u d/\mu \sim 10$). The pressure drop is caused by laminar skin friction (ΔP~1kPa), which is small compared to the operation pressure. Therefore, it is reasonable to assume a constant thermodynamic pressure along the channel. Because of the relatively low temperatures and the small channel size, radiative heat transfer between the solid and the flow gas is generally negligible [127]. Besides, as the solid layer is thin (Bi = $h_{gs}\delta_s/k_s \sim 10^{-4}$, h_{gs} is the convective heat transfer coefficient), the horizontal temperature variation in the solid between neighboring channels is small and hence the solid phase can be treated as a transient fin with temperature variation only along the axial direction of the channel [127].

As shown in Figure 4-1, the numerical model is composed by three parts, corresponding to the fluid flow, mass transfer, and energy transfer. As the gas flows through the channel, the fuel is heated by convection, while reacting with the oxygen carrier to generate CO_2 and steam, which further increases the flow velocity. The mass diffusion of the fuel into the oxygen carrier

layer and of CO_2 and H_2O out of the same layer, and the convective heat transfer between the solid and the gas both depend on the local flow. Therefore, all of the three parts, i.e., the fluid flow, mass transfer and energy transfer, in the reactor must be solved simultaneously.

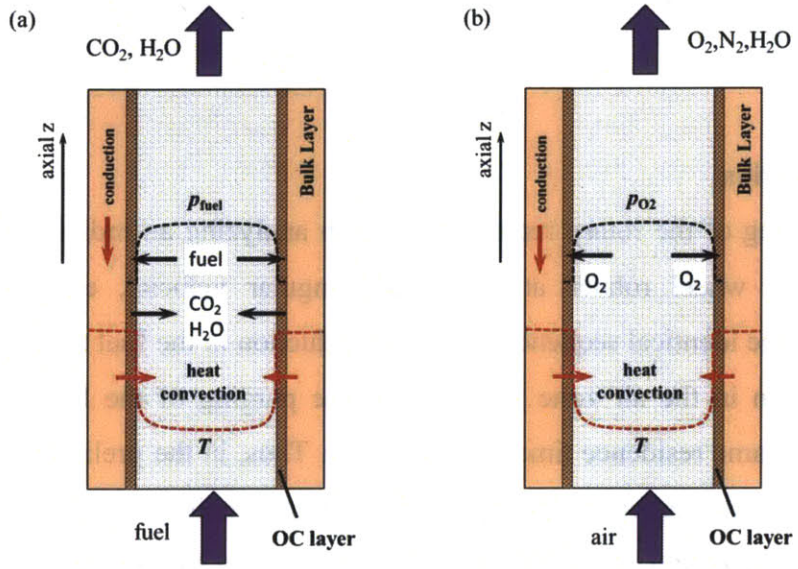

Figure 4-1 Modeling for the reactive flow in one channel for (a) fuel zone and (b) air zone. T is the temperature. p_{fuel} and p_{O2} are the partial pressure of fuel and oxygen.

4.2 Governing Equations

The conservation of a gas species i in the bulk flow and in the porous OC layer can be obtained by integrating Eq. (2.13) over the cross-sectional area of gas passage and porous oxygen carrier layer, as follows (Figure 4-2 (a)):

$$A_p\left[\frac{\partial\left(X_{b,i}C_b\right)}{\partial t}+\frac{\partial\left(u_bX_{b,i}C_b\right)}{\partial z}\right]=-P_cJ_i \tag{4.1}$$

$$A_{oc}\left[\frac{\partial\left(\varepsilon_sX_{s,i}C_s\right)}{\partial t}+\frac{\partial\left(\varepsilon_su_sX_{s,i}C_s\right)}{\partial z}\right]=P_cJ_i+P_c\omega_{g,i} \tag{4.2}$$

where A_p is the cross-section area (m^2) of the channel. A_{oc} is cross-section area (m^2) of the porous OC layer. P_c is the channel perimeter (m). C_b and C_s are the local molar density (mol/m^3) in the bulk flow and in the porous layer. $X_{s,i}$ and $X_{b,i}$ are the molar fractions of gas species i in porous OC layer and bulk flow. u_b and u_s are the bulk velocities (m/s) in the plug flow and in the porous

layer, respectively. ε_s is the volume fraction of the gas in the porous layer. $\omega_{g,i}$ is the overall molar reaction rate (mol/m^{2}s) for species i in the porous OC layer. Note that $\omega_{g,i}$ is the extrinsic reaction rate in the porous layer which models the effective mass diffusion and the chemical reactions. J_i is the external mass diffusion rate (mol/m^{2}s) from the bulk flow to the surface of the porous layer. The species diffusion flux can be calculated based on:

$$J_i = h_{m,i}\left(X_{b,i} - X_{s,i}\right)C_b \tag{4.3}$$

where $h_{m,i}$ is the mass transfer coefficient (m/s) for species i derivable from the Sherwood number. For laminar flow in the square-shape channel, the Sherwood number is 3.61 for the uniform wall flux model and 2.98 for the uniform wall temperature model [127]. For this work, the Sherwood number of 3.61 is utilized because in the periodic state, the wall temperature increases from the inlet to the exit in a similar way as in the uniform wall flux model. The axial gas diffusion is generally much smaller than the convection terms, and thus it is neglected in Eqs. (4.1) and (4.2).

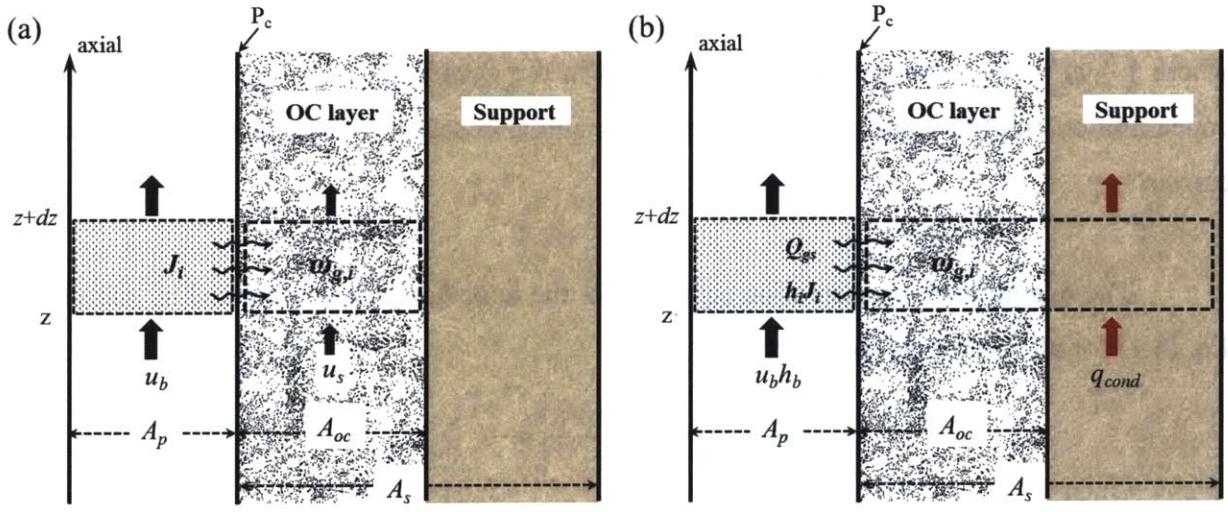

Figure 4-2 Schematic drawing of the (a) species transport and (b) energy transfer in the channel.

Eqs. (4.1) and (4.2) describe the gas species balance among the bulk flow, porous spaces in the solid OC layer and the heterogeneous reaction. The gas components are transported from the bulk towards the OC layer surface by external diffusion (J_i), and then is consumed as it diffuses through the porous layer ($\omega_{g,i}$). Some of the gas species is also stored or transported by convection in the porous layer. As seen in Table 3-2, the gas volume in porous oxygen carrier layer ($\varepsilon_s A_{oc}$) is one order of magnitude smaller than that in the channel (A_p). Thus, the amount of

gas contained in the pores within the porous OC layer is negligible compared to that in bulk flow. The bulk convection velocity in the porous layer is lower than the velocity in the bulk flow because of the surface drag on the flow. Thus, the convection term is also negligible. Therefore, Eq.(4.2) can be simplified into:

$$0 = P_c J_i + P_c \omega_i \tag{4.4}$$

which means that all the gas that diffuses from the bulk flow into the porous layer will be completely consumed and all of the product molecules that are generated from the heterogeneous reaction in the porous layer will be transported out to the bulk flow. The internal mass diffusion is included in the extrinsic reaction rate, $\omega_{g,i}$, and it will be discussed in section 4.3.

The conservation of the oxygen carrier (*CuO* or *Cu*) in the porous OC layer is described as:

$$A_{oc} \frac{\partial\left[\left(1-\varepsilon_s\right) C_{oc,i}\right]}{\partial t} = P_c \omega_{oc,i} \qquad i = CuO \; or \; Cu \tag{4.5}$$

where $1 - \varepsilon_s$ is the volume fraction of the solid in the porous layer. $C_{oc,i}$ is the CuO/Cu molar concentration (mol/m^3) and $\omega_{oc,i}$ is the extrinsic molar reaction rate (mol/m^{2}s) for the oxygen carrier.

The overall mass conservation equation for the bulk flow can be obtained by summing up Eq. (4.1) for all species, as follows:

$$A_p \left[\frac{\partial C_b}{\partial t} + \frac{\partial\left(u_b C_b\right)}{\partial z} \right] = -P_c \sum_i J_i \tag{4.6}$$

Only n-1 species equations (Eq. (4.1) and Eq. (4.2)) are solved since the mole fractions, X_i, sum to unity. The overall mass conservation, Eq.(4.6), can be re-written in terms of the pressure, p.

The energy conservation equation for bulk flow is given by (Figure 4-2 (b)):

$$A_p \left[\frac{\partial E_g}{\partial t} + \frac{\partial\left(u_b H_g\right)}{\partial z} \right] = -P_c Q_{gs} - \sum_i P_c h_{s,i} J_i \tag{4.7}$$

where E_g and H_g are the energy and enthalpy (J/m^3) of the bulk flow. $h_{s,i}$ is the molar enthalpy (J/mol) for species i and it is evaluated at the temperature of the porous layer. Q_{gs} is the inter-phase heat transfer rate (W/m^2) due to heat convection and it can be calculated based on

$$Q_{gs} = h_{gs}\left(T_g - T_s\right) \tag{4.8}$$

where T_s and T_g are the bulk temperatures (K) of solid (including both layers) and the flow. h_{cv} is the convective heat transfer coefficient (W/m^{2}K) derivable from the Nusselt number. The Nusselt number utilized in this model is 3.61 from the uniform wall heat flux laminar heat transfer model [127].

The energy conservation equation for the solid phase (including both layers, as shown in Figure 4-2 (b)) can be written as follows:

$$A_s \frac{\partial E_s}{\partial t} = A_s \frac{\partial}{\partial z}\left(k_s \frac{\partial T_s}{\partial z}\right) + P_c Q_{gs} + \sum_i P_c h_{s,i} J_i \tag{4.9}$$

where A_s is the cross-sectional area (m^2) of the solid phase. E_s is the energy of the solid phase (J/m^3), including both the support material and the oxygen carrier. k_s is the conductivity (W/mK) of the solid phase. As discussed in Section 3.3, the size of the bulk layer is much larger than that of the porous layer ($(1 - \varepsilon_s)\delta_{oc}/(\delta_s - \delta_{oc}) \sim 0.1$), thus the thermal processes within the solid phase are mainly determined by the properties (heat capacity, density, conductivity) of the bulk layer.

Eqs. (4.7) and (4.9) characterizes the energy balance between the bulk flow and the solid phase by means of convective heat transfer, conductive heat transfer and the energy transfer associated with the species transfer. The solid phase behaves as a heat reservoir during operation to temporarily store the energy from the heterogeneous reactions in the porous layer and conduct that heat from the hot to the cold locations and finally heat up the bulk flow by convection. The solid phase, especially the bulk support layer, is critical to the overall energy balance in the reactor. The energy equation for the gas phase in the pore volumes in the porous OC layer is neglected since the gas temperature there is almost identical to the solid temperature.

Since the pressure is assumed to be constant throughout the channel, the momentum equations are excluded from the governing equations. Therefore, Eqs. (4.1), (4.4)-(4.7) and (4.9) completely characterize the fluid flow, mass transfer, and energy transfer within the channel. The boundary conditions at the inlet, $z = 0$, are specified by the inlet conditions (flow rate, species

concentration, and temperature) for each sector, as shown in Figure 3-7 and Table 3-3.

4.3 Reaction Kinetics

The reaction mechanism utilized here is based on the one-step extrinsic (mass-specific) kinetics from Garcia-Labiano et al [125]. The kinetics data in ref. [125] was obtained from thermo-gravimetric analyzer (TGA) experiments at atmospheric pressure with CuO/Al_2O_3 as oxygen carrier particles. The oxygen carrier is prepared by wet-impregnation with 10% active metal oxide load (by weight). The preparation method, the active metal oxide load and the porosity of the oxygen carrier are the same with those assumed in this study, as shown in Table 3-1. The diameter of oxygen carrier particles is within 0.1-0.3mm. The reduction and oxidation reactions are given by the following equations:

$$4CuO(s) + CH_4(g) \rightarrow 4Cu(s) + CO_2(g) + 2H_2O(g) \quad (4.10)$$

$$2Cu\ (s) + O_2(g) \rightarrow 2CuO(s) \quad (4.11)$$

The extrinsic kinetics in ref. [125] is based on the unreacted shrinking-core model (USCM) [128]. The unreacted shrinking-core model assumes that as the reaction progresses, it leaves behind a layer of product which consists of reacted solid, i.e., *Cu* for reduction and *CuO* for oxidation, and the binder. As the reaction proceeds, the thickness of the product layer increases, producing a gradually shrinking unreacted core of the oxygen carrier, although the thickness of the oxygen carrier remains constant.

Garcia-Labiano et al. [125, 129] further pointed out that for CuO/Cu prepared by wet impregnation, the active metal oxide is uniformly dispersed in the porous surface of the support material. The external and internal mass transfer resistances are less important as compared to the chemical kinetics under the operating temperature up to 1000°C. Thus, the gaseous reactant (or product) can easily diffuse through (or out of) the porous medium. Each grain of oxygen carrier is exposed to the ambient gas concentration and hence the active metal oxide in each segment within the porous medium is converted in the same way as that in the plate-like unreacted shrinking-core model[2]. Thus, Garcia-Labiano et al. [125] simplified the USCM as follows:

[2] Note that the authors in ref. [125] treated each grain of the active metal oxide in the OC particles as a plate-like thin layer, although the mechanism is obtained for spherical particles. This simplification is only valid when the internal diffusion resistance is negligible and the reaction is limited by the chemical kinetics. For detailed information, please refer to ref. [125].

$$\frac{dX}{dt} = \frac{v_{oc,i} k_i}{\hat{\rho}_{m,i}} C_{s,i}^{n} \tag{4.12}$$

where $\hat{\rho}_{m,i}$ (mol/m^3) is the molar density of CuO for reduction or Cu for oxidation. $v_{oc,i}$ is the stoichiometric coefficient. k_i is the Arrhenius reaction rate constant (m$^{(3n-3)}$mol$^{(1-n)}$/s). $C_{s,i}$ is the gas concentration (mol/m^3) of CH_4 (for reduction) and O_2 (for oxidation) at the porous surface and n is reaction order. The kinetics parameters are shown in Table 3-1. X is the non-dimensional oxygen carrier conversion variable, defined as:

$$X = \frac{C_{oc,CuO}}{C_{oc,CuO} + C_{oc,Cu}} \tag{4.13}$$

where $C_{oc,CuO}$ and $C_{oc,Cu}$ are the molar concentration (mol/m^3) of copper oxide and copper, respectively. X equals zero when oxygen carrier is fully reduced and unity when fully oxidized.

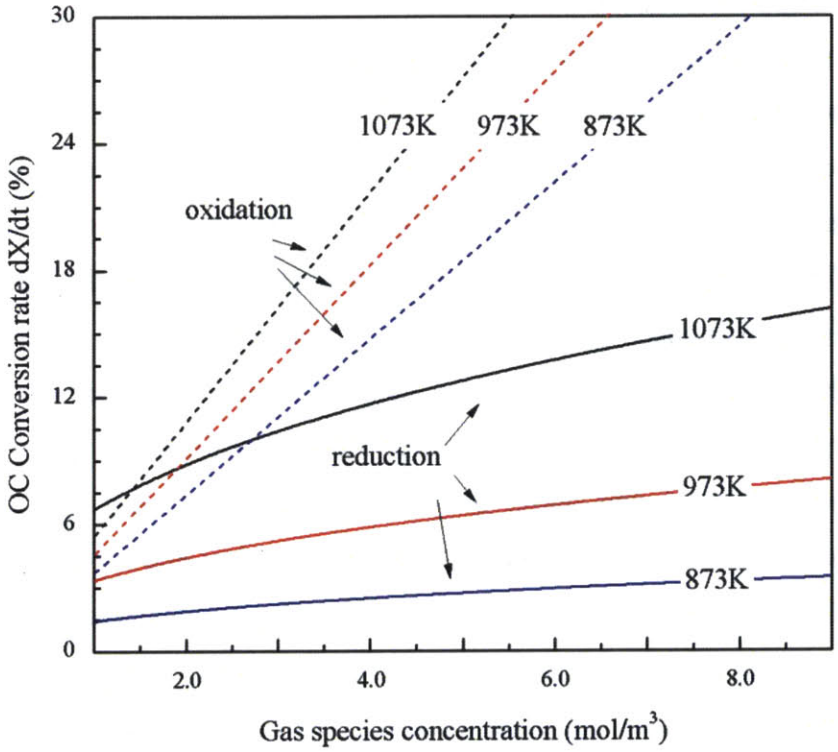

Figure 4-3 Oxygen carrier conversion rate (dX/dt) as a function of gas species concentration and operating temperature. Solid lines are for reduction and dashed lines are for the oxidation.

Figure 4-3 shows the oxygen carrier conversion rate (dX/dt) for reduction and oxidation for a typical range of the gas molar density under current operating conditions. As seen in Figure 4-3, the reduction reactivity is generally lower than the oxidation rate; therefore, reduction is the

rate limiting step. For reduction, as the temperature rises by $100K$, the reaction rate doubles, while for oxidation, only 10% increase is observed. However, the oxidation is more sensitive to the gas species concentration compared to the reduction.

In order to apply this kinetics to the rotary reactor, attention must be paid to the differences in the operating conditions between the mechanism in [125] and the rotary channel design. Ref. [125] is for CuO/Al_2O_3 spherical particles at atmospheric pressure while the numerical model in this work is for the reactive flow over CuO/BN plate-like layer at high pressure. The discrepancies in these three aspects may have significant impacts on the reactor performance. However, for this preliminary analysis, it is reasonable to scale the kinetics to the current design conditions to obtain qualitatively reliable results.

4.3.1 Effect of Support Material

In this study, boron nitride is utilized as the support material since it has a much higher thermal conductivity than alumina. Because of the excellent thermal and chemical stability, boron nitride ceramics are commonly utilized as part of high-temperature equipment.

As discussed in section 2.1.2, the effect of the binder on the reactivity is mainly related to the regenerability of the oxygen carrier. During periodic operations, the inert binder acts as a porous matrix to help enhance the ion permeability, maintain the pore structure and sustain the thermal and the mechanical stresses. Thus, support material with similar properties should exhibit similar periodic performances in chemical-looping combustion.

Comparing alumina and boron nitride, one may notice that they have very similar physical characteristics: both show excellent thermal, chemical and mechanical stability at high temperatures. In their crystalline form, c-BN and α-Al_2O_3, the hardness of these two materials make them suitable as an abrasive and as a component in cutting tools. Both alumina and boron nitride are electrical insulators but good thermal conductors. When in contact with oxygen at high temperatures, a thin passivation layer of B_2O_3 forms to prevent further oxidation in a similar way as in the metallic aluminum material.

Thus, it is reasonable to adapt the mechanism from ref. [125] to the BN supported oxygen carrier in this work.

4.3.2 Effect of Total Pressure

For the modeling, it is recommended to utilize the kinetic parameters experimentally obtained at the same operating pressure as assumed in the model. However, very limited experiments have been performed to investigate the OC behavior at high pressures, and a comprehensive examination of the pressure effect on the CLC reactivity is still missing [81]. One approach to account for the pressure effects is to adapt the results from heterogeneous surface catalyzed reactions (e.g. Langmuir-Hinshelwood mechanism). However, reactions in CLC are primary non-catalytic and OCs act as the sources of undiluted oxygen with relatively high amount of active material, as compared to heterogeneous catalyst. The above difference makes it insufficient to directly apply the knowledge from catalyzed reactions to CLC [11].

In general, the total reaction rate is enhanced by increasing the total pressure [21, 25, 31, 130] because of the increase of the reactant partial pressure. However, Garcia-Labiano et al. [46] reported that this increase in the reaction rate is lower than the expected increase due to the saturation of gas molecules in the pores cavity. Garcia-Labiano et al. [46] expressed this pressure-inhibition effect as:

$$\frac{k_p}{k} = \left(\frac{P}{P_0}\right)^{-a} \tag{4.14}$$

where k_p is the Arrhenius reaction rate constant at pressure P and a is the pressure coefficient. k is the constant at atmospheric pressure, P_0. From (4.14), it is obvious that a higher operating pressure leads to a lower reaction rate constant k_p.

In this study, Eq.(4.14) is utilized to account for the pressure effect. The coefficient a for CuO is tabulated in Table 3-1. Note that in ref. [46], the coefficient a is provided only for CO (a = 0.83), H_2 (a = 0.53) and O_2 (a = 0.68). Thus, the larger coefficient (a = 0.83) is utilized to give a conservative evaluation of the pressure effect on the CH_4 reduction reaction.

4.3.3 Effect of Surface Curvature

Experiments on the redox reactions of the OC [125] have been conducted using spherical particle samples in thermo-gravimetric analyzer with d_p ranging from 0.1mm to 0.3mm while in this study the porous layer of the same materials is used with essentially a plate-like geometry. The geometry of the oxygen carrier may affect the heterogeneous reactions in two ways:

- ***External diffusion resistance:*** as shown in Figure 4-4, a larger curvature of the particle in

traditional applications is accompanied with a higher surface area being exposed to bulk flow. This influences the external mass transfer resistance from the bulk flow to the surface of oxygen carrier.

- ***Internal diffusion resistance:*** oxygen carriers with different shapes and sizes have different diffusion distances through the porous medium. Thus, this leads to different internal mass transfer resistances within the oxygen carrier.

In this study, the external mass transfer is readily characterized by Eq. (4.4). However, the effect of the internal resistance is inherently integrated in the extrinsic kinetics. As mentioned before, the extrinsic kinetics from ref. [125] assumed limited internal mass diffusion resistance. Therefore, in order to apply the extrinsic kinetics from ref. [125], special attention must be paid to the selection of the thickness of the porous layer to assure that the ***internal mass diffusion resistance*** in the porous layer is indeed small and the active metal oxide in the porous medium is converted in the same way as in ref. [125]. Thus the discussion in this sub-section is focused on how the gas components diffuse within the porous medium in a ***spherical particle*** (in ref. [125]) or a ***plate-like layer*** (in this study).

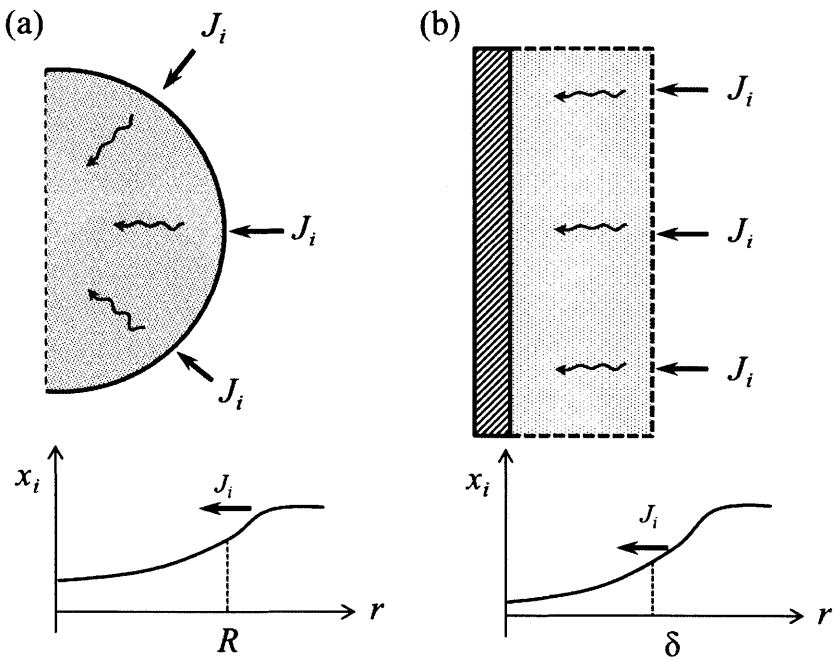

Figure 4-4 Effect of surface curvature on the internal mass diffusion: (a) spherical particle and (b) porous OC layer.

As shown in Figure 4-4, the internal mass diffusion resistance affects the reaction in a

way such that the gas concentration decreases as it diffuses through the oxygen carrier. Therefore, the reactivity at the center of the oxygen carrier should be lower than that on the surface. However, as pointed out by Garcia-Labiano et al. [125], oxygen carrier prepared by wet-impregnation exhibits a well-dispersed metal oxide distribution in the porous surface of the support material. The internal mass-transfer resistance is less important in such CLC systems and the conversion of the oxygen carrier is mainly limited by the chemical reaction rates [81, 125, 129]. The gas concentration variation within the porous medium is thus limited and the oxygen carrier is reduced or oxidized in a highly uniform rate throughout the entire particle.

A simple estimation can be made to validate this conclusion. In the porous layer, the species conservation is expressed by Eq. (2.13). By assuming that the transient term and the convection term are negligible, and porosity, mass diffusion coefficient and the reaction rate are constant, Eq. (2.13) can be simplified as:

$$\nabla\cdot\left(D_a\nabla C_{s,i}\right)+\dot{r}_{g,i}=0 \tag{4.15}$$

where D_a is the diffusion coefficient (m^2/s) in the porous medium, $C_{s,i}$ is the molar density (mol/m^3) and $\dot{r}_{g,i}$ is the reaction rate (mol/m^3s). Integrating the above equation over the cross-section for a spherical particle (Figure 4-4 (a)) and a plate-like layer (Figure 4-4 (b)) respectively, the maximum concentration drop through the medium can be obtained as:

$$\Delta C_{s,i}=\left|\frac{\dot{r}_{g,i}d_p^2}{24D_a}\right| \qquad \text{for a spherical particle} \tag{4.16}$$

$$\Delta C_{s,i}=\left|\frac{\dot{r}_{g,i}\delta_{oc}^2}{2D_a}\right| \qquad \text{for a plate-like layer} \tag{4.17}$$

where d_p is the particle diameter (m), and δ_{oc} is the thickness of porous layer (m). For the reduction reaction (of OC particles from ref. [125]) at $10atm$ and $1073K$, the relative concentration drop $\Delta C_{s,i}/C_{s,i}$ is less than 0.1%[3] and the relative reactivity difference between the core and the outer surface of the OC particles is less than 0.1%. Similar results can be obtained for the oxidation reaction. This estimation validated the conclusion from ref. [125] that the internal mass transfer resistance is small compared to the chemical reactions.

By matching the maximum concentration drop between the spherical particle case (Eq. (4.16)) and the plate-like layer case (Eq.(4.17)), the OC layer thickness for a plate-like layer

[3] The diffusivity D_a is estimated as $\varepsilon_s D_a'$, where ε_s is the porosity of porous medium and D_a' is the binary diffusion coefficient.

should be within $29\mu m$ to $87\mu m$. Similar results can be obtained from the unreacted shrinking-core model [128], as shown in Appendix D. Therefore, for the plate-like OC layer with the thickness within the above range, the maximum species concentration drop through the medium should be small (<0.1%) such that the oxygen carrier within the porous layer is exposed to the same gas concentration and it is converted in the same way as that in ref. [125].

The thickness utilized in this design is 50 μm (see Table 3-2), which is within the above range. Thus, the internal mass diffusion resistances of the porous OC layer and the spherical particle are comparable and both of them are much smaller than the chemical kinetics resistance. The gas concentration variation in both cases is limited (<0.1%) and the oxygen carrier reacts with the gas in a uniform conversion rate throughout the porous medium. The kinetics from Eq. (4.12) can then be adapted in this study, as follows:

$$-\frac{\omega_{g,i}}{v_{g,i}} = -\frac{\omega_{oc,i}}{v_{oc,i}} = \frac{\delta_{oc}\varepsilon_i \rho_{m,i}}{v_{oc,i}} \frac{dX}{dt} \tag{4.18}$$

where $v_{oc,i}$ is the stoichiometric coefficient for the gas species, and ε_i is the volume fraction of CuO (or Cu) in the porous OC layer.

4.4 Numerical Implementation

Because of the highly non-linear and stiff nature of the system of governing equations, the method of lines has been applied to transform the governing equations into a system of ODEs using finite volume discretization along the spatial coordinate. The resulting system of ODEs is then integrated in time using a fully implicit scheme. The code was written in MATLAB and the temporal integration was performed using the ode15s solver [131]. The physical domain is discretized into 100 cells using the control volume formulation with a uniform grid covering the entire channel from the inlet to the outlet. All state variables are calculated at the centers of the control volumes. All advection terms are evaluated using upwind difference approximation. Gas phase and solid phase properties are calculated dynamically as functions of the local state variables. The heat capacities, enthalpies and the conductivities of the gas mixture and the solid phase are evaluated as a function of temperature using the values from the NIST property database [132]. Binary diffusion coefficients are calculated according to Fuller et al. [133].

The flow diagram for the overall simulation of the model is shown in Figure 4-5. Based on the specified design parameters, the physical and chemical processes within the channel are

simulated for repeated cycles. The simulation in one cycle follows a sequence of fuel sector, fuel purge sector, air sector and air purge sector. In each sector, the modeling is based on the inlet condition as specified in Table 3-3, and initial conditions from the results in the last sector. The simulation is repeated until the reactor performances reach a cyclic stationary state, i.e.

$$\|\Delta T_s\| = \sqrt{\frac{1}{\tau H}\int_0^{\tau}\int_0^{H}\left[T_s(z,t+T)-T_s(z,t)\right]^2 dzdt} < 0.01K \tag{4.19}$$

where τ is cyclic period time and H is the height of the channel. Eq. (4.19) means the temperature distributions for two consecutive cycles are almost identical, and hence a periodic state is obtained for the rotary reactor. Typically, converged solutions for the reacting flow were obtained after about 300 cycles (~ 4 hours in rotary reactor operational time).

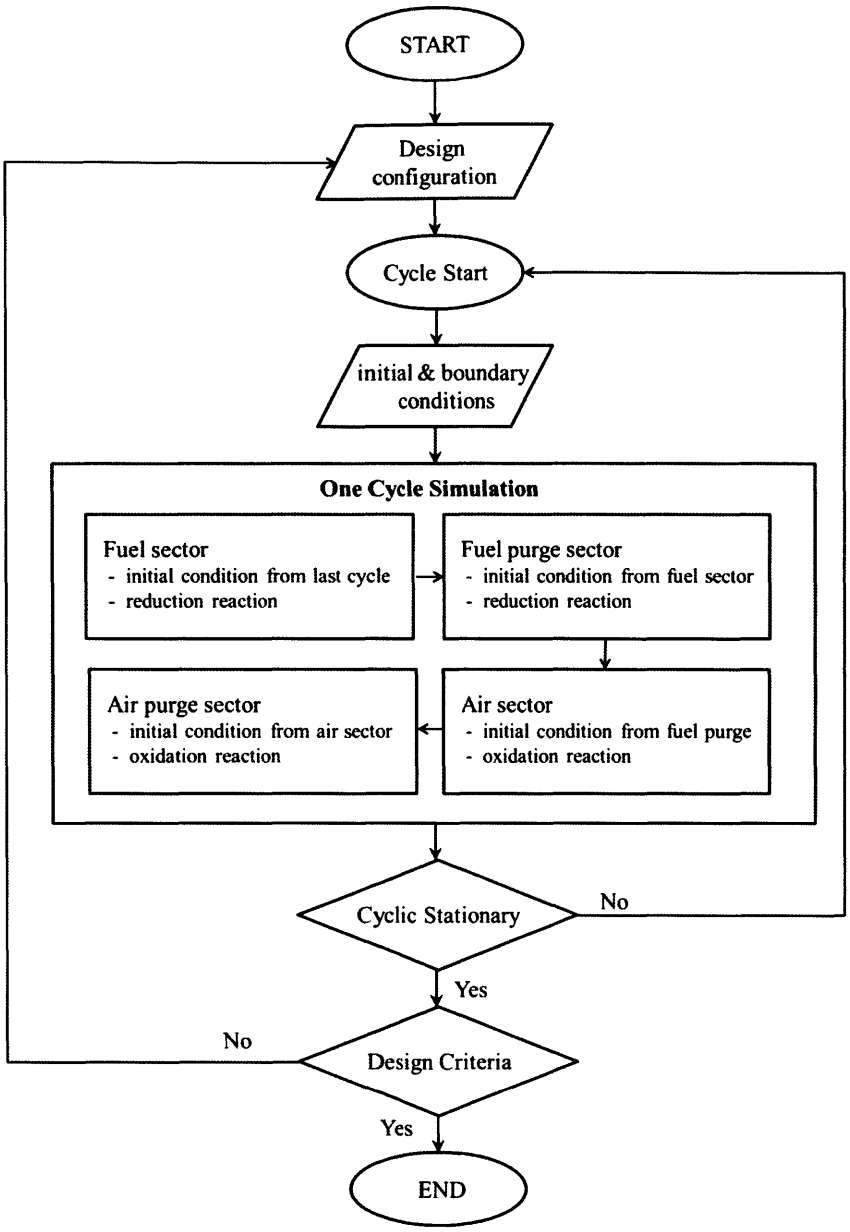

Figure 4-5 Simplified flow diagram of calculation for the overall modeling.

4.5 Validation of the Numerical Approach

Since there are no experimental data available for chemical-looping combustion in a channel flow, the numerical approach was tested with respect to two simple internal flow cases from which analytical solutions can be obtained: nonreactive flow, and isothermal oxidation flow. For validation purposes, results predicted by the model are compared with the analytical solutions for these two cases. For detailed derivation, please refer to Appendix E.

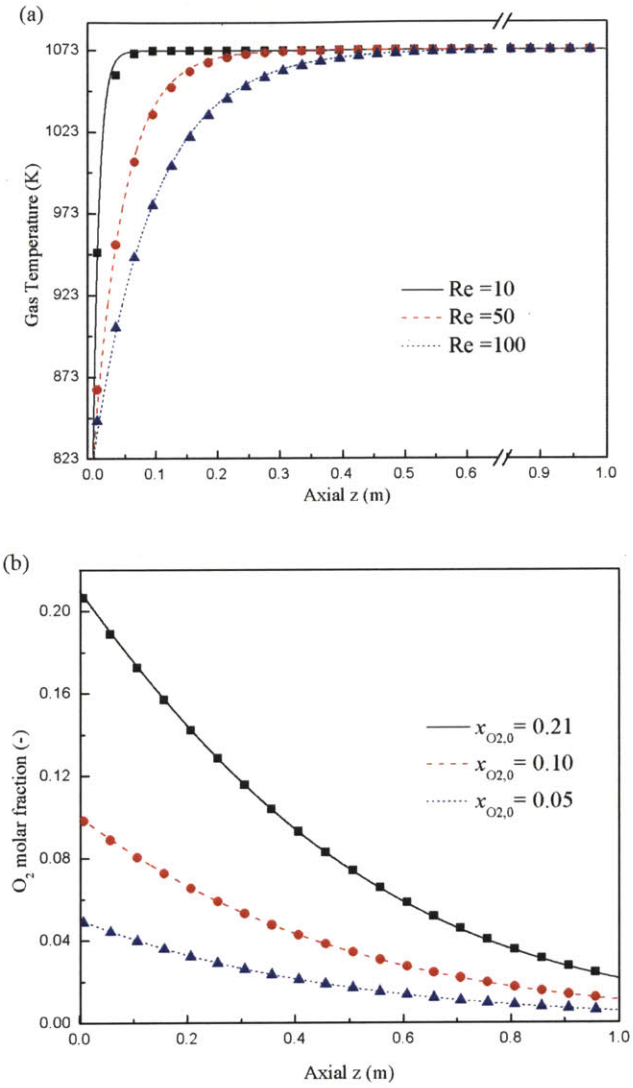

Figure 4-6 Comparison between predicted results (symbols) and analytical solutions (lines); (a) Gas temperature distribution for nonreactive flow with different Reynolds number, and (b) oxygen molar fraction for isothermal oxidation with different inlet oxygen concentration.

Figure 4-6 (a) shows a comparison between predicted results and analytical solutions for the non-reactive energy transfer process. Cold air flow enters the channel and leaves at high temperature while the solid phase is maintained at 1073K. Figure 4-6 (b) shows the comparison of the oxygen molar fraction between predicted results and analytical solutions for the mass transfer process. Both solid and gas phases are kept at 1073K and the air flow continuously oxidizes the oxygen carrier on the surface of the channel. In both cases, the energy or mass

transfer process is coupled with the fluid flow in the channel. As observed in Figure 4-6, the simulation matches the theoretical solutions perfectly.

Chapter 5

Results and Discussions

5.1 Periodic Performance

The developed model was used to simulate the operation of the rotary reactor using the design parameters and the operating conditions shown in Table 3-1 through Table 3-3. Simulations were conducted for repeated cycles until periodic operation was achieved. The output of the model consists of the gas flow velocity, the axial profiles of the temperature and gas composition and the conversion of the oxygen carrier. As an example, Figure 5-1 shows the temperature and gas concentration profiles in one cycle as a function of the angle of rotation (from 0 to 2π) for three locations: near the inlet, in the middle, and near the exit of the wheel. Note that different temperature scales are used for clarity. As observed in Figure 5-1, each curve (temperature or concentration) quickly reaches a quasi-steady state in the fuel sector after a short transition period from the previous purge sector. The fuel concentration gradually decreases from the inlet to the outlet. As seen in Figure 5-1 (c), at the wheel exit the methane concentration is almost zero all the time. Thus, the fuel is almost completely combusted before the exit of the reactor. However, there is a small peak of fuel concentration when the channel enters the fuel purge sector. This is attributed to the relatively high steam velocity in the purge sector (as shown in Table 3-3). The residual fuel is quickly pushed towards the exit of the channel and reacts with the oxygen carrier near the outlet. All the methane is purged out of the channel before the channel enters the air sector. Therefore, no direct mixing between the fuel and oxygen is observed and thus the safety of the operation is ensured.

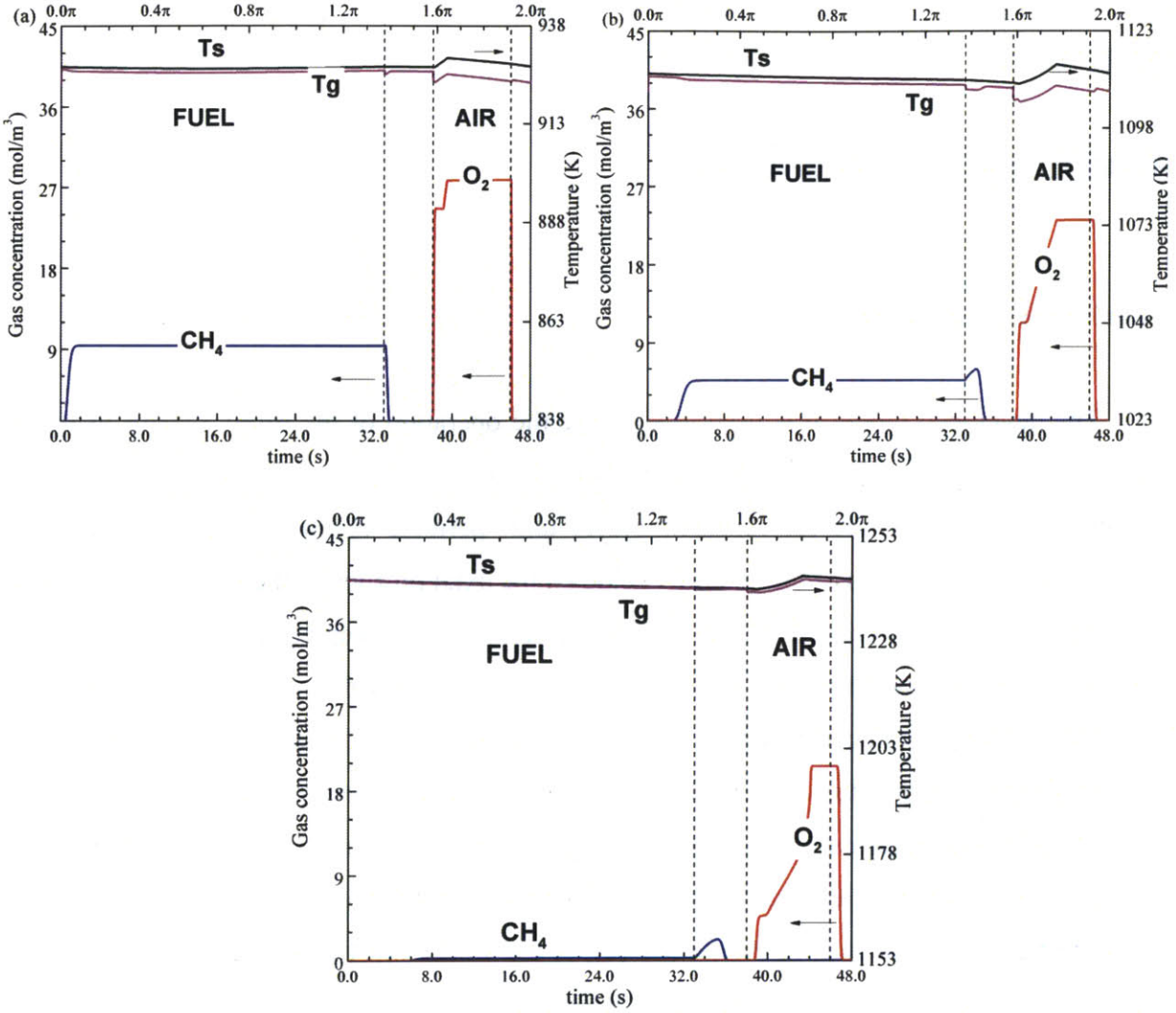

Figure 5-1 Reactor performance in one cycle for different locations along the channel: (a) z =0.12m (10%); (b) z = 0.64 m (50%); and (c) z =1.16m (90%). Note that different temperature scales are used for clarity.

The black lines in Figure 5-1 show the solid temperature profiles, which remain almost constant throughout the entire cycle. The maximum temperature variation with time is less than 10*K*. The limited temperature variation is mainly because of the high thermal inertia of the bulk dense layer in the solid phase which acts as a heat reservoir to match the energy transfer processes. However, small temperature jumps are observed in the air sector when the feed air passes through and the oxygen concentration rises. As discussed in section 3.3, the copper oxidation rate is highly dependent upon the local oxygen concentration. Thus, a rapid oxygen concentration rise leads to a fast energy release from the highly exothermic copper oxidation reactions, which significantly exceeds the heat convection rate to the gas flow. Consequently, the

energy is temporarily stored in the solid phase and the solid temperature increases. After these temperature jumps, the solid temperature decreases since energy is transferred out of the channel walls to the flowing gas by heat convection. Comparing Figure 5-1 (a), (b) and (c), it is observed that the solid temperature gradually increases from the inlet to outlet. The temperature variation at the outlet is within 1K. The gas temperature profile is directly determined by the solid temperature due to the large specific surface area of the channel and hence the high convective heat transfer rate between the solid phase and the flow. Consequently, the gas temperature fluctuation is limited and the maximum variation is generally less than $10K$.

Table 5-1 Overall performance of the rotary reactor in cyclic stationary state

	Value	Unit
Thermal capacity	1.02	MW
Combustion efficiency	97.58%	-
CO_2 separation efficiency	100.00%	-
Second-law efficiency (exergy efficiency)	81.24%	-
Average gas residence time in the fuel sector	6.21	s
Average gas residence time in the fuel purge sector	3.25	s
Average gas residence time in the air sector	1.03	s
Average gas residence time in the air purge sector	0.99	s
Temperature variation between two cycles, Eq.(4.19)	0.01	K

Table 5-2 Steady-state output streams from fuel zone and air zone

Outlet flue gas	**Fuel Zone**	**Air Zone**
Velocity (m/s)	0.16	0.77
Temperature (K)	1245.06	1245.23
CH_4 mole fraction (%)	0.12	0
CO_2 mole fraction (%)	68.85	0
H_2O mole fraction (%)	31.03	21.55
O_2mole fraction (%)	0	10.30
N_2 mole fraction (%)	0	68.15

The periodic performance is shown in Table 5-1. The thermal capacity is 1.02MW and the combustion and the carbon separation efficiencies are close to unity. Table 5-2 shows the outlet flue gas velocity, temperature, and mole-fraction for the fuel zone and air zone. The flue gas in the chamber downstream the wheel is a combination of a large number of flow streams leaving all the channels in the fuel (or air) zone. The gas velocity in the air zone is higher than that in the fuel zone due to the higher feed velocity. The outlet temperatures are close to each other. Only a small fraction of methane leaves the fuel zone without conversion. No dilution between CO_2 and air is observed in the flue gas.

The second-law efficiency is calculated for the rotary reactor as follows:

$$\eta_{II} = \frac{\dot{W}_{\max,out}}{\dot{W}_{\max,in}} \tag{5.1}$$

where $\dot{W}_{\max,in}$ and $\dot{W}_{\max,out}$ are the maximum work that can be obtained from the feed streams and flue streams, respectively. For detailed derivation of $\dot{W}_{\max,in}$ and $\dot{W}_{\max,out}$, please refer to Appendix F. The second-law efficiency of the rotary reactor is 81.24%. $1 - \eta_{II}$ describes the unavoidable work loss due to the reaction within the reactor. As a comparison, the second-law law efficiency is also calculated for the conventional direct combustion under the same operating conditions. Two cases are considered, as shown in Figure 5-2, with one being combustion with purging streams mixing while the other one being unmixed combustion with steam bypassing. The calculation is also included in Appendix F. As shown in Figure 5-2 (a), the efficiency of the first case is 78.62%, which is about 2.6% lower than the rotary design because of the exergy destruction associated with the stream mixing. However, the efficiency for the second case is slightly higher than the rotary design[4], as shown in Figure 5-2 (b). This is because the purging flow rate utilized under current operating conditions is relatively high such that the exergy loss from the purging gas dilution in the rotary design surpasses the exergy gain associated with the flue gas separation. Therefore, in terms of the design optimization, the influences of the purging gas flow rate on the reactor efficiency should be considered.

[4] The outlet temperature for the second case is much higher and in the real application, however, cooling may be necessary to lower the temperature below the material limit. This would lead to lower second-law efficiency.

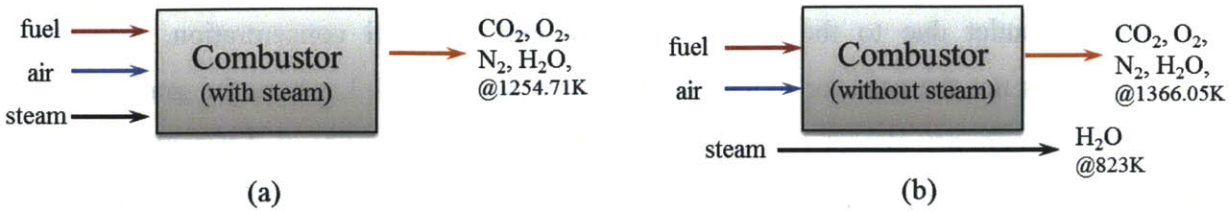

Figure 5-2 Illustration of direction combustion systems for comparison; (a) steam is mixed with fuel and air to generate one flue stream; (b) steam bypasses the reactor without mixing. The 2nd law efficiency: (a) 78.62% and (b) 82.11%.

Pressure loss is expected as the gas flows through the channel. A higher velocity and a smaller channel leads to a larger pressure drop through the reactor. An accurate prediction of the pressure distribution requires solving the momentum equation along the channel. As an estimate, the pressure drop through the channel can be evaluated based on the classic fully developed flow theory, as follows [127]:

$$f = \frac{57}{\mathrm{Re}_d}, \quad \mathrm{Re}_d < 2300 \tag{5.2}$$

where f is the friction factor and Re_d is the Reynolds number. The pressure drop is estimated to be around 1kPa. This pressure loss is small compared to the operating pressure (10*atm*).

5.2 Oxygen Carrier Conversion

During the cyclic operation, the oxygen carrier plays a key role in determining the fuel conversion; therefore it is crucial for the design of the reactor. Figure 5-3 shows the oxygen carrier conversion variation for one cycle along the channel. Note that in Figure 5-3 (a) the conversion contours are plotted as a function of both time and axial location, and darker colors represent higher oxygen concentrations. As seen in Figure 5-3, the oxygen carrier along the channel releases oxygen to oxidize the fuel in the fuel sector and absorbs oxygen in the air sector. After about 45 seconds of one cycle (about one second before the channel moves to the air purge sector), all the copper along the channel is fully regenerated to copper oxide. Therefore, the air sector size is large enough to ensure the complete regeneration of the oxygen carrier.

As discussed in section 3.3, the heterogeneous reaction is closely related to the local temperature and the gas concentration: higher temperatures or species concentration favors conversion. This is evident in Figure 5-3: the reduction reaction rate in the fuel sector is lowest at

the inlet and outlet due to the low temperature and low fuel concentration, respectively. However, this is not the case for oxidation, as shown in Figure 5-3, where the gradients of the conversion contours are almost constant, although the oxidation starts at different time for the different axial locations. This is because oxidation is much more sensitive to the oxygen concentration in the gas stream, as discussed in section 3.3. Therefore, as the gas flows through a channel, the local oxygen carrier rapidly absorbs all available oxygen from the bulk flow, leading to a slowly propagating oxygen front, which is evident in the oxygen molar fraction contour shown in Figure 5-4. As the oxygen molar fraction front moves forward, the oxygen carrier behind the propagating front is already fully oxidized. In contrast, the fuel molar fraction profile in Figure 5-4 quickly reaches a quasi-steady state after a short transition period from the purge sector to fuel sector. The methane concentration distribution along the channel remains stable for about 26 seconds until the channel moves into the fuel purge sector. Comparing the reduction and oxidation processes, we can conclude that for copper oxide as an oxygen carrier, the reactor design and operation are more limited by the reduction rate.

As shown in Figure 5-4, the majority of the fuel is fully converted within the 1.2 m of the channel. Thus, the reactor is long enough to convert the majority of the feed methane. As seen in Figure 5-3, the reduction is fastest at about 0.85m, and at the end of the fuel sector, the oxygen carrier conversion is 0.16. As the channel moves into the fuel purge sector, the fuel concentration contour is shifted slightly upwards towards the outlet of the channel; the unconverted methane reacts with the copper oxide downstream. The oxygen carrier at the outlet (z=1.3m) is barely reacted except during the fuel purge process where high steam flow rate pushes the residual fuel towards the exit of the channel, as illustrated in Figure 5-3 and Figure 5-4. At the end of the fuel zone, the oxygen carrier conversion is a U-shaped curve, as shown in Figure 5-3(c), with a minimum of 0.15 at 0.85m and a maximum of 0.9 at the exit of the channel. The complete reduction of the oxygen carrier is not observed. Thus, the choice of the fuel sector size and the rotational speed is reasonable. For an optimized design, a non-uniform coating, i.e. coating with first increasing and then decreasing thickness along the axial, is a good option to make better utilization of the oxygen carriers.

Figure 5-4 (b) also shows the effects of the external mass transfer resistance on the oxygen carrier conversion. The lines were simulated from the model considering the external mass transfer between the bulk flow and the solid surface while the symbols were calculated

assuming an infinite fast external mass transfer rate in Eq. (4.3). As observed in Figure 5-4 (b), the symbols match the lines perfectly. Thus, the external mass transfer resistance is less important under the current operating conditions and the oxygen carrier conversion is mainly limited by the chemical reactions.

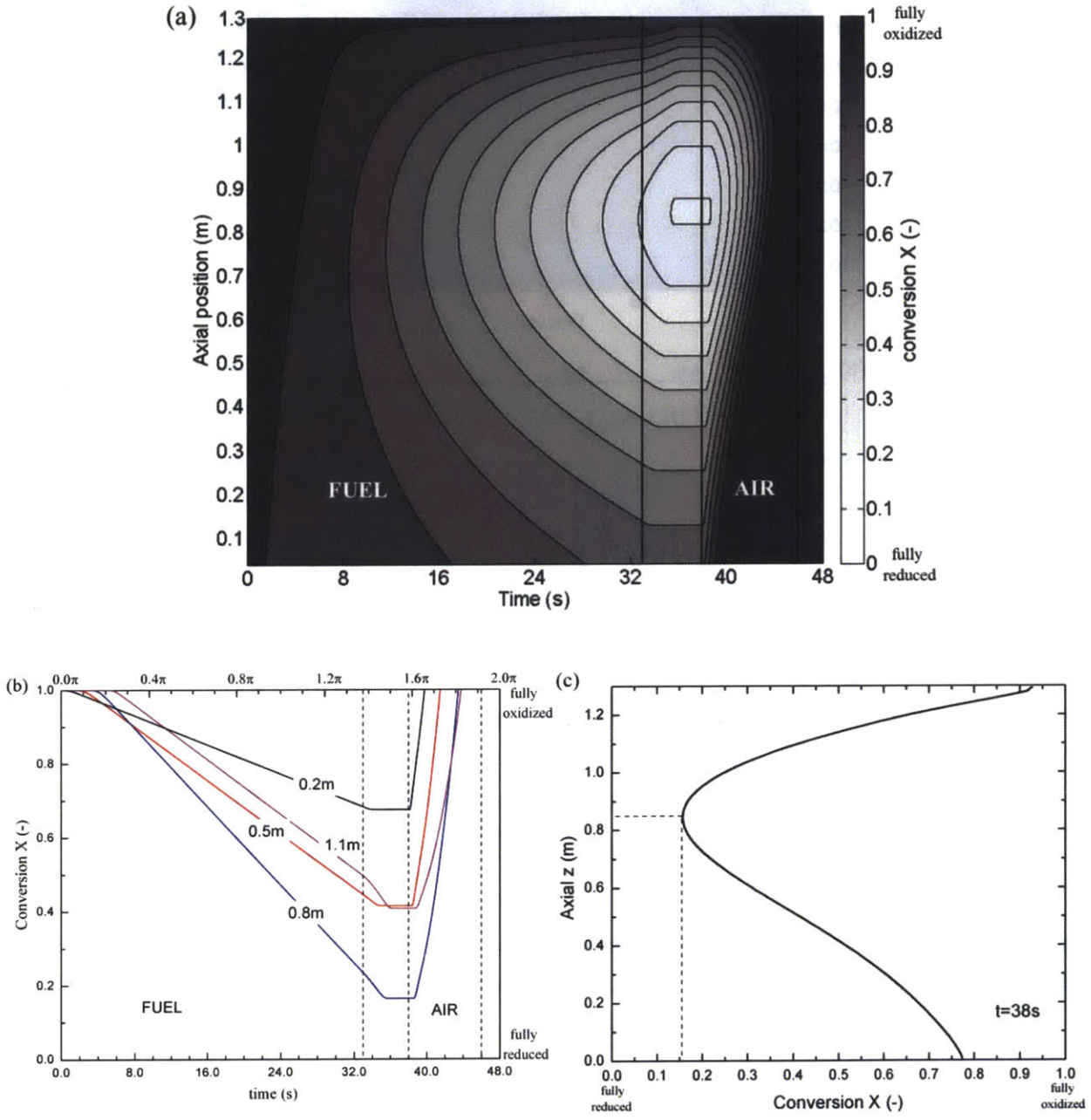

Figure 5-3 Oxygen carrier conversion variation within one cycle: (a) contours of conversion for entire channel; (b) the profiles of conversion for four locations and (c) the profile of conversion at the end of the fuel purge sector (t=38s).

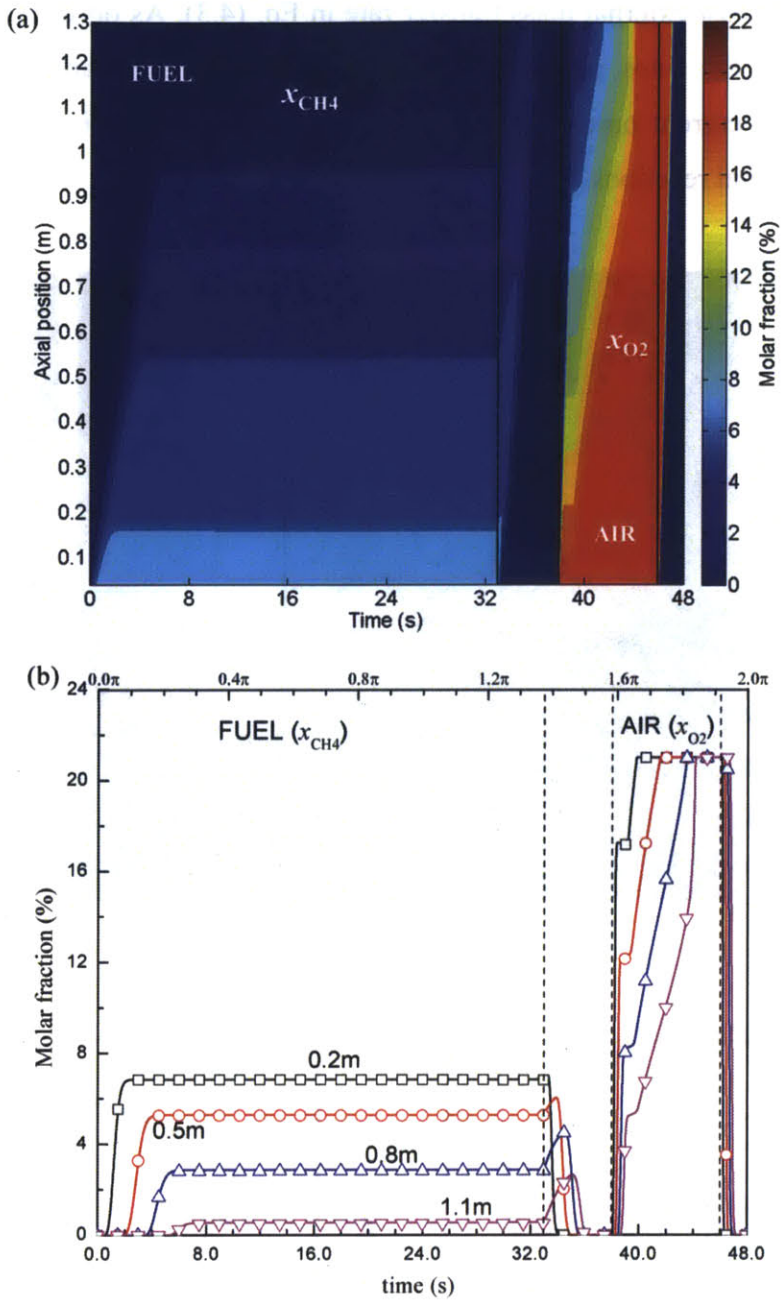

Figure 5-4 The molar fraction of the fuel and the oxygen within one cycle. (a) Contours of molar fraction for entire channel; (b) the profiles of conversion for four locations. Symbols in (b) are the calculated assuming infinite mass transfer coefficient $h_{m,i}$ in Eq. (4.3).

5.3 Gas Velocity Distribution

As the reactor rotates across zones, two time scales are closely coupled with the fluid flow in the channel: the residence time of the channel in each sector, and the residence time of the gas in each channel. The first time scale determines the reactor thermal capacity, oxygen

carrier conversion as well as the regenerability, while the second one affects the fuel conversion and CO_2 separation. Therefore, one of our research interests is to investigate the flow in the channel and the coupling with the reactions.

Figure 5-5 shows the bulk flow velocity distribution in the channel while moving through the different sectors. As the gas flows through the channel, the velocity increases due to the temperature rise. Methane reduction reaction generates two more molecules and hence further increases the flow velocity. The gas velocity in the fuel sector is lower than that in the air sector due to different feed velocities. As seen in Figure 5-5 (a) and (b), there is clearly a steady-state period in each sector where the flow velocity remains almost constant with time. Each two consecutive steady-state periods are connected by a transition region where fast velocity variation is observed. The transition period from the air zone to the fuel zone is smooth. However, strong transient effects are observed in the transition period from the fuel to the air.

This flow response is mainly because of the coupling between the physical and chemical processes in the channel. As the channel moves into another sector, a new feed gas stream enters the channel and the flow becomes fully developed within seconds (see Table 5-1). Due to the relatively slow reduction rate, the methane molecules span throughout the channel and the oxygen carrier continuously releases oxygen to oxidize the fuel until the channel leaves the fuel sector. The reaction rate is almost constant during this period and hence a steady-state velocity profile is obtained. In the fuel purge sector, the fast steam flow pushes the residual fuel to the exit of the channel, leading to faster reduction rates and hence higher flow velocities near the outlet. After the residual fuel is completely removed, a steady-state flow velocity is observed in the fuel purge sector. As the channel leaves the fuel zone and enters the air zone, the slowly propagating oxygen front (as observed in Figure 5-4) rapidly oxidizes the oxygen carrier. The oxidation at the front consumes the majority of oxygen from air and leads to a lower local velocity. When the oxygen carrier is fully regenerated, the oxygen concentration front moves downstream and the local velocity returns to steady-state. Comparing Figure 5-4 (a) and Figure 5-5 (a), it is obvious that the oxygen-fraction contours almost coincide with the velocity curves. Therefore, the flow field fluctuation in the beginning of the air sector is attributed to rapid oxidation and complete oxygen carrier conversion in this region. After 45 seconds, all the oxygen carrier along the channel is fully regenerated and a steady-state flow field is observed.

Fluid velocity oscillation in the air sector suggests stronger transient effects in this region,

in which non-uniform reactivity along the channel as well as the slowly propagating oxygen front causes strong variation of the working condition, such as pressure, mass flow rate, composition, and so on. However, under periodic conditions the combination of a large number of transient flow streams coming out from the channels in the fuel zone (or air zone) mix well into one steady-state flow. Nevertheless, the flow field fluctuation may impact the mechanical stability and these transient effects should be minimized in the design optimization.

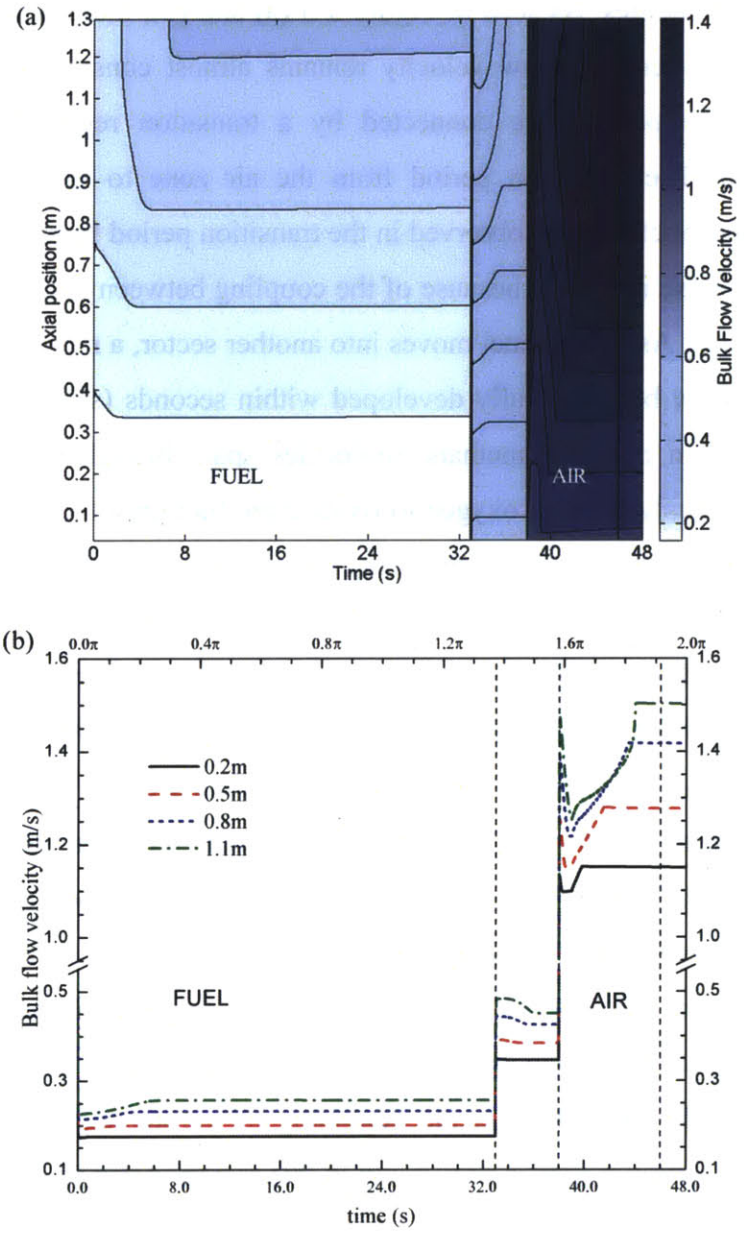

Figure 5-5 Bulk flow velocity variation within one cycle. (a) Contours of velocity field for entire channel; (b) profiles of velocity for four locations.

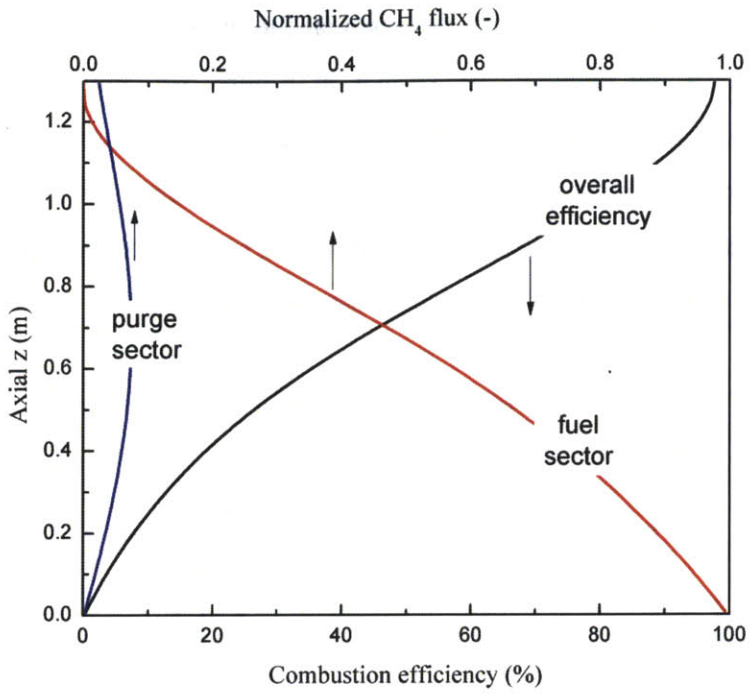

Figure 5-6 The normalized CH_4 concentration in the fuel and purge sectors (solid lines) and the periodic fuel conversion efficiency (dashed line) as a function of axial location.

Figure 5-6 shows the fuel conversion efficiency based on the methane concentration (Figure 5-4) and the flow (Figure 5-5). The conversion efficiency is defined as:

$$\eta_{comb}(z) = 1 - \hat{C}_{CH_4,fuel}(z) - \hat{C}_{CH_4,purge}(z) \tag{5.3}$$

$\hat{C}_{CH_4,fuel}$ and $\hat{C}_{CH_4,purge}$ are the normalized methane concentration:

$$\hat{C}_{CH_4,i}(z) = \frac{\bar{\dot{m}}_{CH_4,i}(z)}{\dot{m}_{CH_4,inlet}} \qquad i = fuel \ or \ purge \tag{5.4}$$

where $\bar{\dot{m}}_{CH_4,i}(z)$ is the time-averaged methane flow rate at location z and $\dot{m}_{CH_4,inlet}$ is the inlet methane feed rate. As seen in Figure 5-6, the fuel conversion efficiency gradually increases. At the outlet of the channel, the fuel conversion is very close to unity. The majority of the methane is consumed in the fuel sector before reaching 1.2 m of the channel, as shown in Figure 5-4 also. The methane concentration decreases monotonically in the fuel sector while a bell-shaped concentration curve is observed in the fuel purge sector with a maximum value of around 0.1 located close to the middle of the channel. Due to the high purge flow rate, residual methane in the channel is pushed to the downstream end of the channel where higher local temperature

significantly enhances the reactivity. Thus, the residual fuel in the purge sector is mostly oxidized near the exit section of the channel. As shown in Figure 5-6, under the current operating conditions, the reactor is long enough to ensure almost complete fuel conversion and at the same time make the most of the oxygen carrier along the entire channel. If a low purge velocity is utilized, the concentration profile is expected to be shifted towards the left but a longer residence time in the fuel purge sector is needed to clean up all the residual fuel.

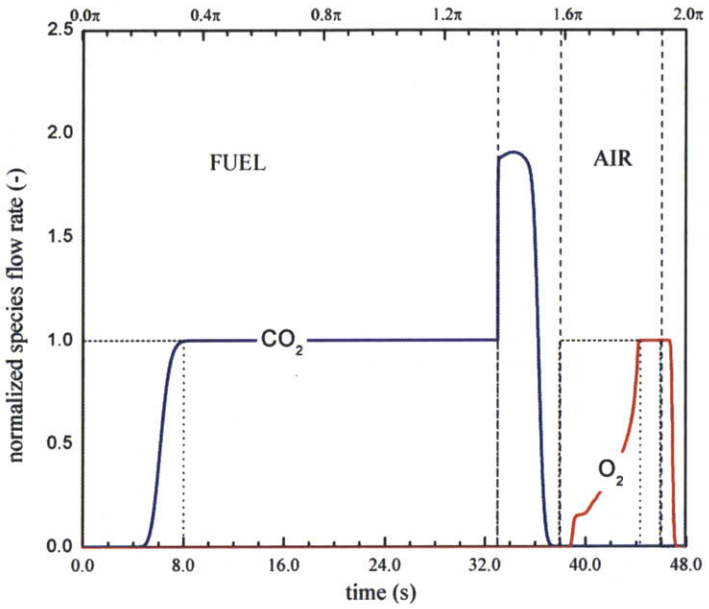

Figure 5-7 CO_2 and O_2 flow rate at the outlet of the channel as a function of time for one cycle.

Figure 5-7 shows the CO_2 and O_2 flux profiles at the outlet of the channel as a function of time. CO_2 flux is normalized by the inlet flow rate in the fuel sector, including both methane and CO_2 while the O_2 flux is normalized by the inlet oxygen flow rate. Thus, at steady state the normalized species flow rate should be unity. As seen in Figure 5-7, carbon is almost completely captured in the fuel zone while unreacted oxygen only exits in the air zone. Therefore, dilution between the oxygen and carbon dioxide is avoided. In the fuel sector, at about 8 seconds, CO_2 flow at the outlet reaches steady state while in the air sector it takes about 7 seconds to reach steady-state. Steady state in the air sector is indicated by the complete regeneration of the oxygen carrier. Because of the high purging velocity, the fuel purging sector has a spike of species flux. In the fuel purge sector, the fuel flow rate drops to zero at about 37 seconds (one second before the channel moves to the air sector). In the air purge sector, the oxygen flux drops to zero after

about one second. Thus, under current operating conditions, the residence time of the channel in each purge sector is long enough to ensure complete separation.

5.4 Temperature Distribution

The temperature distribution within the channel is critical in determining the oxygen carrier reactivity as well as the overall energy balance in repeated cycles. Figure 5-8 (a) compares the time-averaged temperature distribution of the solid and gas phases. The solid temperature increases monotonically from 900K to 1245K. Thus the maximum temperature rise along the channel is within 350K. The gas temperature distribution is directly determined by the solid temperature except at the inlet where the feed gas is much cooler than the solid. Therefore, convective heating at the inlet is significant. The dashed line in Figure 5-8 (a) shows the maximum solid temperature change with time in one cycle. This curve is generally less than $10K$ and therefore the temporal temperature variation is limited, as discussed in Figure 5-1 previously.

The axial temperature variation may have impacts on the stability of the reactor. Different temperatures are accompanied with different thermal expansion rates long the reactor. Thus, the solid matrix near the exit of the reactor tends to expand more than that close to the inlet. In order to deal with the thermal expansion, alternative designs, which are commonly used in gas turbines [134], can be utilized. Figure 5-9 shows two possible options. In Figure 5-9 (a), the container is designed with a small vertical angle to account for the differential thermal expansion of the reactor matrix. The inner diameter of the container is slightly larger at the top chamber. The solid matrix as well as the separation walls in the top and bottom chambers can be shifted vertically by a motor to adjust for the thermal expansion of the wheel with respect to the container. Figure 5-9 (b) shows another option: the container is designed with sufficient size to accommodate the thermal expansion of the solid matrix; peripheral seal brushes are utilized at the feed chamber to reduce the gas bypass. The inlet temperature, i.e. 900K, is below the current material limits for the brush seals [135, 136].

Figure 5-8 (b) shows the overall energy fluxes into the solid phase during one cycle. As shown in Figure 5-8 (b), the overall energy is balanced such that the reaction heat generation is transferred out of the system by convection. The reaction energy generation is highest at the middle of the channel, while convection is important at the inlet. The solid phase acts as a heat reservoir to match the difference: it stores the heat from reaction in the middle and transfers the

heat to the inlet by conduction. At the exit of the channel, however, all of these curves are close to zero, since the majority of the fuel is converted at about 1.2m. Thus, the bulk dense layer in the solid phase with a high thermal inertia and high conductivity plays a key role in maintaining the thermal balance in the channel and in stabilizing the cyclic operation.

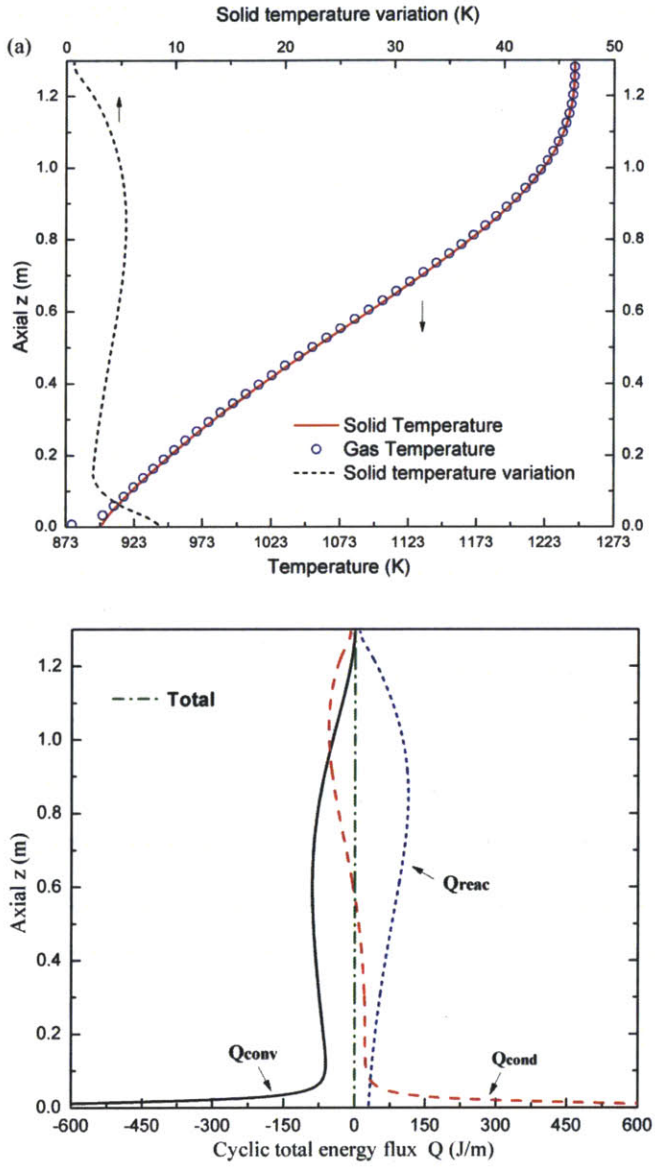

Figure 5-8 (a) The mean temeprature profile as a function of axial location for solid (lines) and flows (circles) and (b) the energy flux in the solid phase within one cycle. The dashed line in (a) is the maximum temperature variation in one cycle.

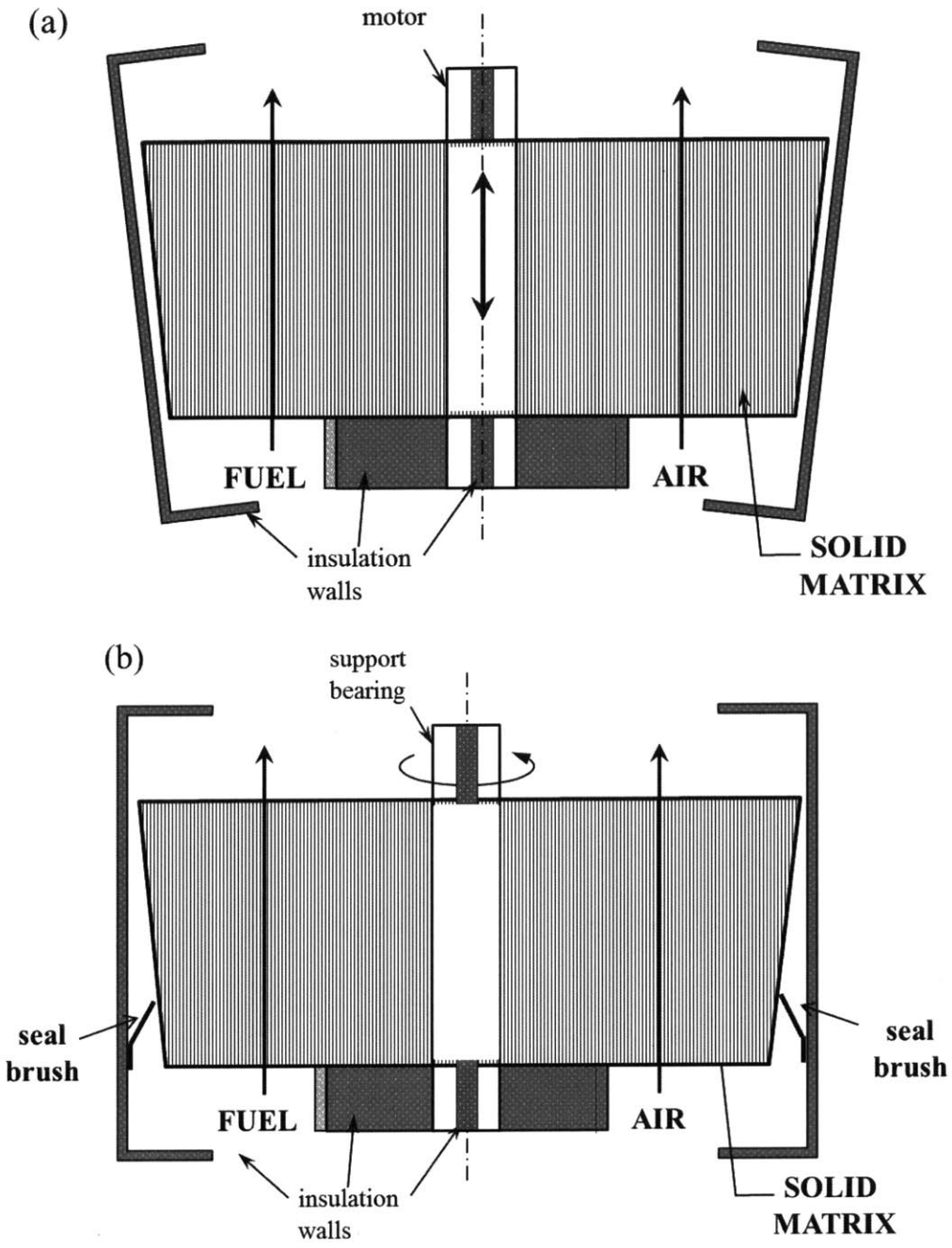

Figure 5-9 Two possible design options to deal with the differential thermal expansion of the reactor.

Page left intentionally blank

Chapter 6

Summary and Conclusion

6.1 Summary

Chemical-looping combustion offers a great opportunity for power generation with inherent CO_2 capture. Its merits, including CO_2 separation, no pollutant emission, as well as potential efficiency enhancement, have made it one of the most promising power generation options. So far the literature on chemical-looping combustion has been mainly focused on designs based on inter-connected fluidized-bed reactors with oxygen carriers particles circulated throughout the reactor. However, the intrinsic complexities associated within the multi-physics reactive flows make the scale-up and commercialization difficult.

In this work, the possibility was investigated to perform chemical-looping combustion using an alternative design based on rotary bed technology. The design of the rotary wheel for CLC was based on the industrial experience of rotary desiccant wheel and the rotary heat exchanger. A horizontal wheel rotates across four sectors: fuel, air, and two purging sectors. The reactor consists of a large number of channels with oxygen carrier coated onto their inner surface. In order to enhance both reactivity and stability, the channel wall has two solid layers with one being highly porous oxygen carrier layer and the other being a bulk dense layer with high thermal inertia and conductivity. A co-current flow pattern is utilized and gas is heated from a low inlet temperature to a high outlet temperature at elevated pressures. Flue streams from a large number of channels merge into two separate streams from the fuel zone and air zone, respectively. Advantages of the rotary design include the intrinsic separation between fuel and air streams, compactness, scale-up feasibility, and periodic and continuous operation without the necessity of particles transport at high pressures.

Simplified one-dimensional models have been constructed to simulate the cyclic performances of one channel with copper oxide as the oxygen carrier and boron nitride as the binder. Simulations have been carried out for repeated cycles until cyclic stationary-state performances are reached. Preliminary analysis shows that high fuel conversion efficiency as

well as high carbon separation efficiency at the outlet of the channel. Due to the relatively low reduction rate of copper oxide, the fuel conversion occurs continuously from the inlet to the end of the reactor, while in the air sector, oxygen carriers are rapidly regenerated, consuming a large amount of oxygen from the air leading to a slow propagating oxygen front. Velocity fluctuation is observed during the transition periods between sectors because of complete reactions of oxygen carriers. Gas temperature increases monotonically from 823K to 1245K, which is mainly determined by the solid temperature. In the periodic state, the solid temperature variations with time are limited within 10K. The overall energy in the solid phase is balanced between reaction heat release, conduction and convective cooling. Preliminary analysis shows great potential for the rotary design for chemical-looping combustion applications. Sensitivity study should be carried out in the further to optimize the design and the operating conditions.

6.2 Areas for Future Work

The simplified model illustrated the feasibility of the rotary reactor design. However, potential challenges still exist for the construction, the operation, the scaling-up and the commercialization of the rotary CLC. The potential challenges may include, for instance, how to assemble a large number of long but small channels into one rotary wheel, how to construct the layered structure inside each channel, how to coat oxygen carrier onto the porous support medium to obtain desirable porosity, loading and good stability, how to insulate the reactor to minimize the leakage and gas bypass, how to heat the wheel into desirable temperature distribution during the start-up period, how to maintain the regenerability during the cyclic operation under high temperature and high pressure, etc. These challenges are significant to the application of the rotary design and they must be approached critically and comprehensively. Experiments must be performed in the future to deal with the above challenges and great care should be exercised to examine all possible pitfalls and flaws.

The simplified channel model can be used to perform sensitivity analysis on the impact of the critical design and operating parameters, such as different oxygen carriers or binders, oxygen carrier loading, temperature, pressure, channel cross-section area, length, feed velocity and rotational velocity. In addition, the models can be used as a design tool for alternative design concepts for the reactor, such as counter-current flow pattern, different shape and arrangement of the channels.

A more elaborate model should be developed for the heterogeneous reactions in the porous OC layer based on the experiments specifically for the channel at elevated pressures. This model should include the effects of pore distribution and variation, film diffusion, and the intrinsic chemical reactions. This model should be integrated with the simplified channel model to provide more robust predictions.

The simplified model can only predict the axial temperature, concentration profiles in the channel in periodic stationary state. Therefore, for a more comprehensive analysis of the reactor performance, it is necessary to develop detailed CFD models including of the radial mass and energy transfer between the gas and the solid. In addition, detailed models should also characterize the radial and peripheral variations along the reactor as well as gas leaking and fuel bypassing effects.

The reactor models should be coupled with the power generation units to analyze the systematic flow-sheet performances. Choice in other components (gas turbine, compressor, etc.) strongly affects the operating conditions and hence influences the reactor performance. Cyclic analysis with power generation integration should be carried out to test the efficiency, and the economic cost of the rotary chemical-looping reactor.

Page left intentionally blank

Bibliography

[1] M. Halmann, Steinberg M. Greenhouse Gas Carbon Dioxide Mitigation: Science and Technology. Boca Raton, FL, USA: Lewis Publishers; 2000.
[2] IEA. Key World Energy Statistics. 2006.
[3] IPCC. Special Report on Carbon Dioxide Capture and Storage. 2005.
[4] IEA. Putting Carbon Back Into the Ground. International Energy Agency Greenhouse Gas R&D Program. 2001.
[5] Herzog H, Golomb D. Carbon Capture and Storage from Fossil Fuel Use. Encyclopeida of Energy. 2004:277-87.
[6] Kvamsdal HM, Jordal K, Bolland O. A quantitative comparison of gas turbine cycles with CO2 capture. Energy. 2007;32:10-24.
[7] Hossain MM, de LHI. Chemical-looping combustion (CLC) for inherent CO2 separations-a review. Chem Eng Sci. 2008;63:4433-51.
[8] He F, Li H, Zhao Z. Advancements in development of chemical-looping combustion: a review. Int J Chem Eng. 2009:No pp. given.
[9] Lyngfelt A, Johansson M, Mattisson T. Chemical-looping Combustion - status of development. 9th International Conference on Circulating Fluidized Beds (CFB-9). Hamburg, Germany2008.
[10] Lyngfelt A. Oxygen Carriers for Chemical Looping Combustion - 4 000 h of Operational Experience. Oil & Gas Science and Technology – Rev IFP Energies nouvelles. 2011.
[11] Fan LS. Chemical looping system for fossil energy conversions: A JOHN WILEY & SONS, INC., PUBLICATION; 2010.
[12] Hurst S. Production of hydrogen by the steam-iron method. Journal of the American Oil Chemists' Society. 1939;16:29-35.
[13] Lewis WK, Gillilandm ER. Production of pure carbon dioxide. US Patent. United States of America1954.
[14] Richter HJ, Knoche KF. Reversibility of combustion processes. ACS Symposium Series1983. p. 71-85.
[15] Ishida M, Zheng D, Akehata T. Evaluation of a chemical-looping-combustion power-generation system by graphic exergy analysis. Energy (Oxford). 1987;12:147-54.
[16] Ishida M, Jin H. A new advanced power-generation system using chemical-looping combustion. Energy (Oxford). 1994;19:415-22.
[17] McGlashan NR. Chemical-looping combustion - a thermodynamic study. Proc Inst Mech Eng, Part C. 2008;222:1005-19.
[18] Chakravarthy VK, Daw CS, Pihl JA. Thermodynamic analysis of alternative approaches to chemical looping combustion. Energy Fuels. 2011;25:656-69.
[19] Lyngfelt A, Leckner B, Mattisson T. A fluidized-bed combustion process with inherent CO2 separation; application of chemical-looping combustion. Chem Eng Sci. 2001;56:3101-13.
[20] Jerndal E, Mattisson T, Lyngfelt A. Thermal analysis of chemical-looping combustion. Chem Eng Res Des. 2006;84:795-806.
[21] Jin H, Ishida M. Reactivity study on a novel hydrogen fueled chemical-looping combustion. Int J Hydrogen Energy. 2001;26:889-94.
[22] de DLF, Garcia-Labiano F, Adanez J, Gayan P, Abad A, Corbella BM, et al. Development of Cu-based oxygen carriers for chemical-looping combustion. Fuel. 2004;83:1749-57.
[23] Ishida M, Jin H. A Novel Chemical-Looping Combustor without NOx Formation. Ind Eng Chem Res. 1996;35:2469-72.

[24] Adanez J, de DLF, Garcia-Labiano F, Gayan P, Abad A, Palacios JM. Selection of Oxygen Carriers for Chemical-Looping Combustion. Energy Fuels. 2004;18:371-7.
[25] Jin H, Ishida M. A new type of coal gas fueled chemical-looping combustion. Fuel. 2004;83:2411-7.
[26] Ishida M, Jin H. A novel combustor based on chemical-looping reactions and its reaction kinetics. J Chem Eng Jpn. 1994;27:296-301.
[27] Ishida M, Jin H, Okamoto T. A Fundamental Study of a New Kind of Medium Material for Chemical-Looping Combustion. Energy Fuels. 1996;10:958-63.
[28] Ishida M, Jin H. CO2 recovery in a power plant with chemical looping combustion. Energy Convers Manage. 1997;38:S187-S92.
[29] Ishida M, Jin H, Okamoto T. Kinetic behavior of solid particle in chemical-looping combustion: suppressing carbon deposition in reduction. Energy Fuels. 1998;12:223-9.
[30] Jin H, Okamoto T, Ishida M. Development of a Novel Chemical-Looping Combustion: Synthesis of a Looping Material with a Double Metal Oxide of CoO-NiO. Energy Fuels. 1998;12:1272-7.
[31] Jin H, Okamoto T, Ishida M. Development of a Novel Chemical-Looping Combustion: Synthesis of a Solid Looping Material of NiO/NiAl2O4. Ind Eng Chem Res. 1999;38:126-32.
[32] Johansson M, Mattisson T, Lyngfelt A, Abad A. Using continuous and pulse experiments to compare two promising nickel-based oxygen carriers for use in chemical-looping technologies. Fuel. 2008;87:988-1001.
[33] Johansson E, Mattisson T, Lyngfelt A, Thunman H. Combustion of syngas and natural gas in a 300 W chemical-looping combustor. Chem Eng Res Des. 2006;84:819-27.
[34] Mattisson T, Johansson M, Lyngfelt A. The use of NiO as an oxygen carrier in chemical-looping combustion. Fuel. 2006;85:736-47.
[35] de DLF, Ortiz M, Adanez J, Garcia-Labiano F, Abad A, Gayan P. Synthesis gas generation by chemical-looping reforming in a batch fluidized bed reactor using Ni-based oxygen carriers. Chem Eng J (Amsterdam, Neth). 2008;144:289-98.
[36] Gayan P, de DLF, Garcia-Labiano F, Adanez J, Abad A, Dueso C. Effect of support on reactivity and selectivity of Ni-based oxygen carriers for chemical-looping combustion. Fuel. 2008;87:2641-50.
[37] Ksepko E, Siriwardane RV, Tian H, Simonyi T, Sciazko M. Comparative Investigation on Chemical Looping Combustion of Coal-Derived Synthesis Gas containing H2S over Supported NiO Oxygen Carriers. Energy Fuels. 2010;24:4206-14.
[38] Corbella BM, de DLF, Garcia-Labiano F, Adanez J, Palacios JM. Performance in a Fixed-Bed Reactor of Titania-Supported Nickel Oxide as Oxygen Carriers for the Chemical-Looping Combustion of Methane in Multicycle Tests. Ind Eng Chem Res. 2006;45:157-65.
[39] Cao Y, Casenas B, Pan W-P. Investigation of Chemical Looping Combustion by Solid Fuels. 2. Redox Reaction Kinetics and Product Characterization with Coal, Biomass, and Solid Waste as Solid Fuels and CuO as an Oxygen Carrier. Energy Fuels. 2006;20:1845-54.
[40] Abad A, Mattisson T, Lyngfelt A, Ryden M. Chemical-looping combustion in a 300W continuously operating reactor system using a manganese-based oxygen carrier. Fuel. 2006;85:1174-85.
[41] Adanez J, Garcia-Labiano F, de DLF, Gayan P, Celaya J, Abad A. Nickel-Copper Oxygen Carriers To Reach Zero CO and H2 Emissions in Chemical-Looping Combustion. Ind Eng Chem Res. 2006;45:2617-25.
[42] Cho P, Mattisson T, Lyngfelt A. Comparison of iron-, nickel-, copper- and manganese-based oxygen carriers for chemical-looping combustion. Fuel. 2004;83:1215-25.
[43] Corbella BM, De DL, Garcia F, Adanez J, Palacios JM. The Performance in a Fixed Bed Reactor of Copper-Based Oxides on Titania as Oxygen Carriers for Chemical Looping Combustion of Methane. Energy Fuels. 2005;19:433-41.
[44] Corbella BM, de DLF, Garcia-Labiano F, Adanez J, Palacios JM. Characterization Study and Five-Cycle Tests in a Fixed-Bed Reactor of Titania-Supported Nickel Oxide as Oxygen Carriers for the Chemical-Looping Combustion of Methane. Environ Sci Technol. 2005;39:5796-803.

[45] de DLF, Gayan P, Garcia-Labiano F, Celaya J, Abad A, Adanez J. Impregnated CuO/Al2O3 Oxygen Carriers for Chemical-Looping Combustion: Avoiding Fluidized Bed Agglomeration. Energy Fuels. 2005;19:1850-6.
[46] Garcia-Labiano F, Adanez J, de DLF, Gayan P, Abad A. Effect of Pressure on the Behavior of Copper-, Iron-, and Nickel-Based Oxygen Carriers for Chemical-Looping Combustion. Energy Fuels. 2006;20:26-33.
[47] Mattisson T, Jaerdnaes A, Lyngfelt A. Reactivity of Some Metal Oxides Supported on Alumina with Alternating Methane and Oxygen-Application for Chemical-Looping Combustion. Energy Fuels. 2003;17:643-51.
[48] Chuang SY, Dennis JS, Hayhurst AN, Scott SA. Development and performance of Cu-based oxygen carriers for chemical-looping combustion. Combust Flame. 2008;154:109-21.
[49] Corbella BM, De DL, Garcia F, Adanez J, Palacios JM. Characterization and Performance in a Multicycle Test in a Fixed-Bed Reactor of Silica-Supported Copper Oxide as Oxygen Carrier for Chemical-Looping Combustion of Methane. Energy Fuels. 2006;20:148-54.
[50] Zafar Q, Mattisson T, Gevert B. Integrated Hydrogen and Power Production with CO2 Capture Using Chemical-Looping Reforming-Redox Reactivity of Particles of CuO, Mn2O3, NiO, and Fe2O3 Using SiO2 as a Support. Ind Eng Chem Res. 2005;44:3485-96.
[51] Zafar Q, Mattisson T, Gevert B. Redox Investigation of Some Oxides of Transition-State Metals Ni, Cu, Fe, and Mn Supported on SiO2 and MgAl2O4. Energy & Fuels. 2006;20:34-44.
[52] Son SR, Go KS, Kim SD. Thermogravimetric Analysis of Copper Oxide for Chemical-Looping Hydrogen Generation. Ind Eng Chem Res. 2009;48:380-7.
[53] Mattisson T, Johansson M, Lyngfelt A. CO2 capture from coal combustion using chemical-looping combustion - Reactivity investigation of Fe, Ni and Mn based oxygen carriers using syngas. Proc Int Tech Conf Coal Util Fuel Syst. 2006;31st:879-90.
[54] Johansson M, Mattisson T, Lyngfelt A. Investigation of Fe2O3 with MgAl2O4 for Chemical-Looping Combustion. Ind Eng Chem Res. 2004;43:6978-87.
[55] Mattisson T, Lyngfelt A, Cho P. The use of iron oxide as an oxygen carrier in chemical-looping combustion of methane with inherent separation of CO2. Fuel. 2001;80:1953-62.
[56] Mattisson T, Johansson M, Lyngfelt A. Multicycle Reduction and Oxidation of Different Types of Iron Oxide Particles-Application to Chemical-Looping Combustion. Energy Fuels. 2004;18:628-37.
[57] Ryden M, Cleverstam E, Johansson M, Lyngfelt A, Mattisson T. Fe2O3 on Ce-, Ca-, or Mg-stabilized ZrO2 as oxygen carrier for chemical-looping combustion using NiO as additive. AIChE J. 2010;56:2211-20.
[58] Ryden M, Lyngfelt A, Mattisson T, Chen D, Holmen A, Bjoergum E. Novel oxygen-carrier materials for chemical-looping combustion and chemical-looping reforming: LaxSr1-xFeyCo1-yO3-δ perovskites and mixed-metal oxides of NiO, Fe2O3 and Mn3O4. Int J Greenhouse Gas Control. 2008;2:21-36.
[59] Abad A, Garcia-Labiano F, de DLF, Gayan P, Adanez J. Reduction Kinetics of Cu-, Ni-, and Fe-Based Oxygen Carriers Using Syngas (CO + H2) for Chemical-Looping Combustion. Energy Fuels. 2007;21:1843-53.
[60] Kolbitsch P, Bolhar-Nordenkampf J, Proell T, Hofbauer H. Operating experience with chemical looping combustion in a 120 kW dual circulating fluidized bed (DCFB) unit. Int J Greenhouse Gas Control. 2010;4:180-5.
[61] Berguerand N, Lyngfelt A. Design and operation of a 10kWth chemical-looping combustor for solid fuels - Testing with South African coal. Fuel. 2008;87:2713-26.
[62] Berguerand N, Lyngfelt A. The use of petroleum coke as fuel in a 10 kWth chemical-looping combustor. Int J Greenhouse Gas Control. 2008;2:169-79.
[63] Berguerand N, Lyngfelt A. Chemical-Looping Combustion of Petroleum Coke Using Ilmenite in a 10 kWth Unit-High-Temperature Operation. Energy Fuels. 2009;23:5257-68.
[64] Berguerand N, Lyngfelt A. Batch testing of solid fuels with ilmenite in a 10 kWth chemical-looping combustor. Fuel. 2010;89:1749-62.

[65] Leion H, Lyngfelt A, Johansson M, Jerndal E, Mattisson T. The use of ilmenite as an oxygen carrier in chemical-looping combustion. Chem Eng Res Des. 2008;86:1017-26.
[66] Leion H, Mattisson T, Lyngfelt A. Solid fuels in chemical-looping combustion. Int J Greenhouse Gas Control. 2008;2:180-93.
[67] Adanez J, Cuadrat A, Abad A, Gayan P, de DLF, Garcia-Labiano F. Ilmenite Activation during Consecutive Redox Cycles in Chemical-Looping Combustion. Energy Fuels. 2010;24:1402-13.
[68] Leion H, Mattisson T, Lyngfelt A. CO2 capture from direct combustion of solid fuels with chemical-looping combustion. Proc Int Tech Conf Coal Util Fuel Syst. 2008;33rd:221-32.
[69] Berguerand N, Lyngfelt A. Operation in a 10 kWth chemical-looping combustor for solid fuel-testing with a Mexican petroleum coke. Energy Procedia. 2009;1:407-14.
[70] Xiao R, Song Q-L, Song M, Lu Z-J, Zhang S-A, Shen L-H. Pressurized chemical-looping combustion of coal with an iron ore-based oxygen carrier. Combust Flame. 2010;157:1140-53.
[71] Leion H, Jerndal E, Steenari B-M, Hermansson S, Israelsson M, Jansson E, et al. Solid fuels in chemical-looping combustion using oxide scale and unprocessed iron ore as oxygen carriers. Fuel. 2009;88:1945-54.
[72] Xiao R, Song Q, Zhang S, Zheng W, Yang Y. Pressurized Chemical-Looping Combustion of Chinese Bituminous Coal: Cyclic Performance and Characterization of Iron Ore-Based Oxygen Carrier. Energy Fuels. 2010;24:1449-63.
[73] Yang Y-c, Xiao R, Song Q-l, Zheng W-g. Pressurized chemical-looping combustion of coal using iron ore as an oxygen carrier. Dongli Gongcheng Xuebao. 2010;30:56-62.
[74] Leion H, Mattisson T, Lyngfelt A. Use of Ores and Industrial Products As Oxygen Carriers in Chemical-Looping Combustion. Energy Fuels. 2009;23:2307-15.
[75] Ryden M, Cleverstam E, Lyngfelt A, Mattisson T. Waste products from the steel industry with NiO as additive as oxygen carrier for chemical-looping combustion. Int J Greenhouse Gas Control. 2009;3:693-703.
[76] Ortiz M, Gayan P, de DLF, Garcia-Labiano F, Abad A, Pans MA, et al. Hydrogen production with CO2 capture by coupling steam reforming of methane and chemical-looping combustion: Use of an iron-based waste product as oxygen carrier burning a PSA tail gas. J Power Sources. 2011;196:4370-81.
[77] Johansson M, Mattisson T, Lyngfelt A. Investigation of Mn3O4 with stabilized ZrO2 for chemical-looping combustion. Chem Eng Res Des. 2006;84:807-18.
[78] Cho P, Mattisson T, Lyngfelt A. Defluidization Conditions for a Fluidized Bed of Iron Oxide-, Nickel Oxide-, and Manganese Oxide-Containing Oxygen Carriers for Chemical-Looping Combustion. Ind Eng Chem Res. 2006;45:968-77.
[79] Stobbe ER, de Boer BA, Geus JW. The reduction and oxidation behaviour of manganese oxides. Catalysis Today. 1999;47:161-7.
[80] Stobbe E. Catalytic routes for the conversion of methane to synthesis gas. Utrecht: University of Utrecht; 1999.
[81] Adanez J, Abad A, Garcia-Labiano F, Gayan P, de Diego LF. Progress in Chemical-Looping Combustion and Reforming technologies. Progress in Energy and Combustion Science. 2012;38:215-82.
[82] Shen L, Wu J, Gao Z, Xiao J. Characterization of chemical looping combustion of coal in a 1 kWth reactor with a nickel-based oxygen carrier. Combust Flame. 2010;157:934-42.
[83] Li F, Zeng L, Velazquez-Vargas LG, Yoscovits Z, Fan L-S. Syngas chemical looping gasification process: bench-scale studies and reactor simulations. AIChE J. 2010;56:2186-99.
[84] Li F, Zeng L, Fan L-S. Biomass direct chemical looping process: Process simulation. Fuel. 2010;89:3773-84.
[85] Noorman S, van SAM, Kuipers H. Packed Bed Reactor Technology for Chemical-Looping Combustion. Ind Eng Chem Res. 2007;46:4212-20.

[86] Noorman S, van SAM, Kuipers JAM. Experimental validation of packed bed chemical-looping combustion. Chem Eng Sci. 2010;65:92-7.
[87] Noorman S, Gallucci F, van SAM, Kuipers JAM. Experimental Investigation of Chemical-Looping Combustion in Packed Beds: A Parametric Study. Ind Eng Chem Res. 2011;50:1968-80.
[88] Dahl IM, Bakken E, Larring Y, Spjelkavik AI, Haakonsen SF, Blom R. On the development of novel reactor concepts for chemical looping combustion. Energy Procedia. 2009;1:1513-9.
[89] Håkonsen SF, Blom R. Chemical Looping Combustion in a Rotating Bed Reactor – Finding Optimal Process Conditions for Prototype Reactor. Environmental Science & Technology. 2011;45:9619-26.
[90] Lyngfelt A, Thunman H. Construction and 100 h of operational experience of a 10-kW chemical-looping combustor. Elsevier Ltd.; 2005. p. 625-45.
[91] Adanez J, Dueso C, de DLF, Garcia-Labiano F, Gayan P, Abad A. Methane Combustion in a 500 Wth Chemical-Looping Combustion System Using an Impregnated Ni-Based Oxygen Carrier. Energy Fuels. 2009;23:130-42.
[92] Linderholm C, Jerndal E, Mattisson T, Lyngfelt A. Investigation of NiO-based mixed oxides in a 300-W chemical-looping combustor. Chem Eng Res Des. 2010;88:661-72.
[93] Johansson E, Mattisson T, Lyngfelt A, Thunman H. A 300W laboratory reactor system for chemical-looping combustion with particle circulation. Fuel. 2006;85:1428-38.
[94] Kunii D, Levenspiel O. Fluidization Engineering: Butterworth-Heinemann; 1991.
[95] Adanez J, Gayan P, Celaya J, De DLF, Garcia-Labiano F, Abad A. Chemical Looping Combustion in a 10 kWth Prototype Using a CuO/Al2O3 Oxygen Carrier: Effect of Operating Conditions on Methane Combustion. Ind Eng Chem Res. 2006;45:6075-80.
[96] Noorman S, Gallucci F, van Sint Annaland M, Kuipers JAM. A theoretical investigation of CLC in packed beds. Part 2: Reactor model. Chemical Engineering Journal. 2011;167:369-76.
[97] Proell T, Kolbitsch P, Bolhar-Nordenkampf J, Hofbauer H. A novel dual circulating fluidized bed system for chemical looping processes. AIChE J. 2009;55:3255-66.
[98] Shen L, Wu J, Gao Z, Xiao J. Reactivity deterioration of NiO/Al2O3 oxygen carrier for chemical looping combustion of coal in a 10 kWth reactor. Combust Flame. 2009;156:1377-85.
[99] Gidaspow D. Multiphase Flow and Fluidization - Continuum and Kinetic Theory Descriptions: Academic Press; 1994.
[100] Jung J, Gamwo IK. Multiphase CFD-based models for chemical looping combustion process: Fuel reactor modeling. Powder Technol. 2008;183:401-9.
[101] Kruggel-Emden H, Rickelt S, Stepanek F, Munjiza A. Development and testing of an interconnected multiphase CFD-model for chemical looping combustion. Chem Eng Sci. 2010;65:4732-45.
[102] Naqvi R, Bolland O, Brandvoll O, Helle K. Chemical looping combustion analysis of natural gas fired power cycle with inherent CO_2-capture. Proceedings of ASME turbo EXPO 2004. Vienna, Austria.: Atlanta: American Society of Mechanical Engineers; 2004.
[103] Naqvi R, Wolf J, Bolland O. Part-load analysis of a chemical looping combustion combined cycle with CO2 capture. Energy (Oxford, U K). 2007;32:360-70.
[104] Wolf J, Anheden M, Yan J. Comparison of nickel- and iron-based oxygen carriers in chemical looping combustion for CO2 capture in power generation. Fuel. 2005;84:993-1006.
[105] Consonni S, Lozza G, Pelliccia G, Rossini S, Saviano F. Chemical-Looping Combustion for Combined Cycles With CO2 Capture. J Eng Gas Turbines Power. 2006;128:525-34.
[106] Naqvi R, Bolland O. Multi-stage chemical looping combustion (CLC) for combined cycles with CO2 capture. Int J Greenhouse Gas Control. 2007;1:19-30.
[107] Anheden M, Svedberg G. Exergy analysis of chemical-looping combustion systems. Energy Convers Manage. 1998;39:1967-80.
[108] Naqvi R. Analysis of Natural Gas-Fired Power Cycles with Chemical Looping Combustion for CO2 Capture.: Norwegian University of Science and Technology; 2006.

[109] Jin H, Zhang X, Hong H, Han W. An Innovative Gas Turbine Cycle With Methanol-Fueled Chemical-Looping Combustion. J Eng Gas Turbines Power. 2009;131:061701/1-/8.
[110] Jin H, Ishida M. A novel gas turbine cycle with hydrogen-fueled chemical-looping combustion. Int J Hydrogen Energy. 2000;25:1209-15.
[111] Brandvoll O, Bolland O. Inherent CO2 capture by using chemical looping combustion in a natural gas fired power cycle. J Eng Gas Turbines Power. 2004;126:316-21.
[112] Zhang X, Han W, Hong H, Jin H. A chemical intercooling gas turbine cycle with chemical-looping combustion. Energy (Oxford, U K). 2009;34:2131-6.
[113] Hong H, Han T, Jin H. A Low Temperature Solar Thermochemical Power Plant With CO2 Recovery Using Methanol-Fueled Chemical Looping Combustion. J Sol Energy Eng. 2010;132:031002/1-/8.
[114] Hong H, Jin H. A Novel Solar Thermal Cycle with Chemical Looping Combustion. Int J Green Energy. 2005;2:397-407.
[115] Hong H, Jin H, Liu B. A novel solar-hybrid gas turbine combined cycle with inherent CO2 separation using chemical-looping combustion by solar heat source. J Sol Energy Eng. 2006;128:275-84.
[116] Ge TS, Li Y, Wang RZ, Dai YJ. A review of the mathematical models for predicting rotary desiccant wheel. Renewable and Sustainable Energy Reviews. 2008;12:1485-528.
[117] Hoval. Hoval Rotary Heat Exchanger for Heat Recovery in Ventilation Systems.: www.hoval.com/docs/Waermerueck_pdf/rotor_en_4208534.pdf.
[118] Drobnic B, Oman J, Tuma M. A numerical model for the analyses of heat transfer and leakages in a rotary air preheater. International Journal of Heat and Mass Transfer. 2006;49:5001-9.
[119] Shah RK, Skiepko T. Influence of leakage distribution on the thermal performance of a rotary regenerator. Applied Thermal Engineering. 1999;19:685-705.
[120] Skiepko T. Effect of reduction in seal clearances on leakages in a rotary heat exchanger. Heat Recovery Systems and CHP. 1989;9:553-9.
[121] Skiepko T. Method of monitoring and measuring seal clearances in a rotary heat exchanger. Heat Recovery Systems and CHP. 1988;8:469-73.
[122] Pavone D. CO2 capture by means of chemical looping combustion. Proceedings of the COMSOL Multiphysics User's Conference. Paris, France2005.
[123] Pavone D, Rolland M, Lebas E. CO2 capture using chemical looping combustion for gas turbine application. Proceedings of 8th International Conference of Greenhouse Gas Control Technologies (GHGT-8). Trondheim, Norway2006.
[124] Cichanowicz JE, Muzio LJ. Rotary regenerative chemical looping combustion. USA . 2009. p. 9pp.
[125] Garcia-Labiano F, De DLF, Adanez J, Abad A, Gayan P. Reduction and Oxidation Kinetics of a Copper-Based Oxygen Carrier Prepared by Impregnation for Chemical-Looping Combustion. Ind Eng Chem Res. 2004;43:8168-77.
[126] Cravalho EG, Smith JL. Engineering thermodynamics: Pitman; 1981.
[127] Mills AF. Heat Transfer (2nd Edition): Prentice Hall; 1998.
[128] Levenspiel O. Chemical Reaction Engineering. New York: John Willey and Sons; 1999.
[129] Garcia-Labiano F, de DLF, Adanez J, Abad A, Gayan P. Temperature variations in the oxygen carrier particles during their reduction and oxidation in a chemical-looping combustion system. Chem Eng Sci. 2005;60:851-62.
[130] Siriwardane R, Poston J, Chaudhari K, Zinn A, Simonyi T, Robinson C. Chemical-Looping Combustion of Simulated Synthesis Gas Using Nickel Oxide Oxygen Carrier Supported on Bentonite. Energy Fuels. 2007;21:1582-91.
[131] Shampine LF, Reichelt MW. The MATLAB ODE Suite. SIAM Journal on Scientific Computing. 1997;18:1-22.
[132] NIST Standard Reference Database Number 69, webbook.nist.gov/chemistry, accessed 12/2011.

[133] Fuller EN, Schettler PD, Giddings JC. NEW METHOD FOR PREDICTION OF BINARY GAS-PHASE DIFFUSION COEFFICIENTS. Industrial & Engineering Chemistry. 1966;58:18-27.
[134] Chupp RE, Hendricks RC, Lattime SB, Steinetz BM. Sealing in turbomachinery. J Propul Power. 2006;22:313-49.
[135] Dinc S, Demiroglu M, Turnquist N, Mortzheim J, Goetze G, Maupin J, et al. Fundamental Design Issues of Brush Seals for Industrial Applications. Journal of Turbomachinery. 2002;124:293-300.
[136] Fellenstein JA, DellaCorte C, Moore KD, Boyes E. High Temperature Brush Seal Tuft Testing of Metallic Bristles Versus Chrome Carbide. AIAA Paper No AIAA-96-29081996.
[137] Hatanka T, Matsuda S, Hatano H. A new-concept gas-solid combustion system "MERIT" for high combustion efficiency and low emissions. Proc Intersoc Energy Convers Eng Conf. 1997;32nd:944-8.
[138] Mattisson T, Lyngfelt A, Cho P. Possibility of using iron oxide as an oxygen carrier for combustion of methane with removal of CO2 - Application of chemical-looping combustion. Fifth International Conference on Greenhouse Gas Control Technologies. Cairns, Australia2000. p. 205-10.
[139] Ryu H-J, Bae D-H, Han K-H, Lee S-Y, Jin G-T, Choi J-H. Oxidation and reduction characteristics of oxygen carrier particles and reaction kinetics by unreacted core model. Korean J Chem Eng. 2001;18:831-7.
[140] Ishida M, Yamamoto M, Ohba T. Experimental results of chemical-looping combustion with NiO/NiAl2O4 particle circulation at 1200 °C. Energy Convers Manage. 2002;43:1469-78.
[141] Jin H, Ishida M. Reactivity Study on Natural-Gas-Fueled Chemical-Looping Combustion by a Fixed-Bed Reactor. Ind Eng Chem Res. 2002;41:4004-7.
[142] Ryu H-j, Bae D-h, Jin G-t. Effect of temperature on reduction reactivity of oxygen carrier particles in a fixed bed chemical-looping combustor. Korean J Chem Eng. 2003;20:960-6.
[143] Ryu H-J, Lim N-Y, Bae D-H, Jin G-T. Carbon deposition characteristics and regenerative ability of oxygen carrier particles for chemical-looping combustion. Korean J Chem Eng. 2003;20:157-62.
[144] Song KS, Seo YS, Yoon HK, Cho SJ. Characteristics of the NiO/hexaaluminate for chemical looping combustion. Korean J Chem Eng. 2003;20:471-5.
[145] Villa R, Cristiani C, Groppi G, Lietti L, Forzatti P, Cornaro U, et al. Ni based mixed oxide materials for CH4 oxidation under redox cycle conditions. Journal of Molecular Catalysis A: Chemical. 2003;204-205:637-46.
[146] Adanez J, Garca-Labiano F, De Diego LF, Gayan P, Celaya J, Abad A. Characterization of Oxygen Carriers for Chemical-Looping Combustion. Proceedings of the 7th International Conference on Greenhouse Gas Control Technologies. Vancouver, Canada2004.
[147] Brandvoll O. Chemical looping combustion: Fuel conversion with inherent carbon dioxide capture 2005.
[148] Cho P, Mattisson T, Lyngfelt A. Carbon Formation on Nickel and Iron Oxide-Containing Oxygen Carriers for Chemical-Looping Combustion. Ind Eng Chem Res. 2005;44:668-76.
[149] De lRT, Gutierrez DL, Martinez VC, Ortiz AL. Redox stabilization effect of TiO2 in Co3O4 as oxygen carrier for the production of hydrogen through POX and chemical looping processes. Int J Chem React Eng. 2005;3:No pp. given.
[150] Ishida M, Takeshita K, Suzuki K, Ohba T. Application of Fe2O3−Al2O3 Composite Particles as Solid Looping Material of the Chemical-Loop Combustor. Energy & Fuels. 2005;19:2514-8.
[151] Lee J-B, Park C-S, Choi S-I, Song Y-W, Kim Y-H, Yang H-S. Redox characteristics of various kinds of oxygen carriers for hydrogen fueled chemical-looping combustion. J Ind Eng Chem (Seoul, Repub Korea). 2005;11:96-102.
[152] Readman JE, Olafsen A, Larring Y, Blom R. La0.8Sr0.2Co0.2Fe0.8O3-δ as a potential oxygen carrier in a chemical looping type reactor, an in-situ powder X-ray diffraction study. J Mater Chem. 2005;15:1931-7.

[153] Johansson M, Mattisson T, Lyngfelt A. Comparison of Oxygen Carriers for Chemical-looping combustion. Thermal Science. 2006;10:93-107.
[154] Johansson M, Mattisson T, Lyngfelt A. Use of NiO/NiAl2O4 Particles in a 10 kW Chemical-Looping Combustor. Ind Eng Chem Res. 2006;45:5911-9.
[155] Johansson M, Mattisson T, Lyngfelt A. Creating a Synergy Effect by Using Mixed Oxides of Iron- and Nickel Oxides in the Combustion of Methane in a Chemical-Looping Combustion Reactor. Energy Fuels. 2006;20:2399-407.
[156] Readman JE, Olafsen A, Smith JB, Blom R. Chemical Looping Combustion Using NiO/NiAl2O4: Mechanisms and Kinetics of Reduction-Oxidation (Red-Ox) Reactions from In Situ Powder X-ray Diffraction and Thermogravimetry Experiments. Energy Fuels. 2006;20:1382-7.
[157] Ryden M, Lyngfelt A, Mattisson T. Synthesis gas generation by chemical-looping reforming in a continuously operating laboratory reactor. Fuel. 2006;85:1631-41.
[158] Scott SA, Dennis JS, Hayhurst AN, Brown T. In situ gasification of a solid fuel and CO2 separation using chemical looping. AIChE J. 2006;52:3325-8.
[159] Son SR, Kim SD. Chemical-Looping Combustion with NiO and Fe2O3 in a Thermobalance and Circulating Fluidized Bed Reactor with Double Loops. Ind Eng Chem Res. 2006;45:2689-96.
[160] Song Y-W, Lee J-B, Park C-S, Hwang G-J, Choi S-I, Yang H-S, et al. Synthesis and redox properties of NiO/NiAl2O4 oxygen carriers for hydrogen-fueled chemical-looping combustion. J Ind Eng Chem (Seoul, Repub Korea). 2006;12:255-60.
[161] Abad A, Mattisson T, Lyngfelt A, Johansson M. The use of iron oxide as oxygen carrier in a chemical-looping reactor. Fuel. 2007;86:1021-35.
[162] Abad A, Adanez J, Garcia-Labiano F, de DLF, Gayan P, Celaya J. Mapping of the range of operational conditions for Cu-, Fe-, and Ni-based oxygen carriers in chemical-looping combustion. Chem Eng Sci. 2007;62:533-49.
[163] Corbella BM, Palacios JM. Titania-supported iron oxide as oxygen carrier for chemical-looping combustion of methane. Fuel. 2007;86:113-22.
[164] de DLF, Garcia-Labiano F, Gayan P, Celaya J, Palacios JM, Adanez J. Operation of a 10 kWth chemical-looping combustor during 200 h with a CuO-Al2O3 oxygen carrier. Fuel. 2007;86:1036-45.
[165] Erri P, Varma A. Solution combustion synthesized oxygen carriers for chemical looping combustion. Chem Eng Sci. 2007;62:5682-7.
[166] Erri P, Varma A. Spinel-Supported Oxygen Carriers for Inherent CO2 Separation during Power Generation. Industrial & Engineering Chemistry Research. 2007;46:8597-601.
[167] Hossain MM, Sedor KE, de LHI. Co-Ni/Al2O3 oxygen carrier for fluidized bed chemical-looping combustion: desorption kinetics and metal-support interaction. Chem Eng Sci. 2007;62:5464-72.
[168] Hossain MM, de Lasa HI. Reactivity and stability of Co-Ni/Al2O3 oxygen carrier in multicycle CLC. AIChE Journal. 2007;53:1817-29.
[169] Jin GT, Ryu H-J, Jo S-H, Lee S-Y, Son SR, Kim SD. Hydrogen production in fluidized bed by chemical-looping cycle. Korean J Chem Eng. 2007;24:542-6.
[170] Leion H, Mattisson T, Lyngfelt A. The use of petroleum coke as fuel in chemical-looping combustion. Fuel. 2007;86:1947-58.
[171] Zafar Q, Abad A, Mattisson T, Gevert B. Reaction Kinetics of Freeze-Granulated NiO/MgAl2O4 Oxygen Carrier Particles for Chemical-Looping Combustion. Energy Fuels. 2007;21:610-8.
[172] Zafar Q, Abad A, Mattisson T, Gevert B, Strand M. Reduction and oxidation kinetics of Mn3O4/Mg-ZrO2 oxygen carrier particles for chemical-looping combustion. Chem Eng Sci. 2007;62:6556-67.
[173] Gao Z, Shen L, Xiao J, Qing C, Song Q. Use of Coal as Fuel for Chemical-Looping Combustion with Ni-Based Oxygen Carrier. Ind Eng Chem Res. 2008;47:9279-87.
[174] Leion H, Mattisson T, Lyngfelt A. Combustion of a German lignite using chemical-looping with oxygen uncoupling (CLOU). Proc Int Tech Conf Coal Util Fuel Syst. 2008;33rd:189-99.

[175] Li F, Kim H, Sridhar D, Zeng L, Wang F, Fan LS. Coal Direct Chemical Looping (CDCL) process. American Institute of Chemical Engineers; 2008. p. 540/1-/6.
[176] Linderholm C, Abad A, Mattisson T, Lyngfelt A. 160 h of chemical-looping combustion in a 10 kW reactor system with a NiO-based oxygen carrier. Int J Greenhouse Gas Control. 2008;2:520-30.
[177] Mattisson T, Johansson M, Jerndal E, Lyngfelt A. The reaction of NiO/NiAl2O4 particles with alternating methane and oxygen. The Canadian Journal of Chemical Engineering. 2008;86:756-67.
[178] Ryden M, Lyngfelt A, Mattisson T. Chemical-Looping Combustion and Chemical-Looping Reforming in a Circulating Fluidized-Bed Reactor Using Ni-Based Oxygen Carriers. Energy Fuels. 2008;22:2585-97.
[179] Sedor KE, Hossain MM, de LHI. Reduction kinetics of a fluidizable nickel-alumina oxygen carrier for chemical-looping combustion. Can J Chem Eng. 2008;86:323-34.
[180] Sedor KE, Hossain MM, de LHI. Reactivity and stability of Ni/Al2O3 oxygen carrier for chemical-looping combustion (CLC). Chem Eng Sci. 2008;63:2994-3007.
[181] Shen L, Zheng M, Xiao J, Xiao R. A mechanistic investigation of a calcium-based oxygen carrier for chemical looping combustion. Combust Flame. 2008;154:489-506.
[182] Song Q, Xiao R, Deng Z, Zheng W, Shen L, Xiao J. Multicycle Study on Chemical-Looping Combustion of Simulated Coal Gas with a CaSO4 Oxygen Carrier in a Fluidized Bed Reactor. Energy Fuels. 2008;22:3661-72.
[183] Song Q, Xiao R, Deng Z, Shen L, Xiao J, Zhang M. Effect of Temperature on Reduction of CaSO4 Oxygen Carrier in Chemical-Looping Combustion of Simulated Coal Gas in a Fluidized Bed Reactor. Ind Eng Chem Res. 2008;47:8148-59.
[184] Song Q, Xiao R, Deng Z, Zhang H, Shen L, Xiao J, et al. Chemical-looping combustion of methane with CaSO4 oxygen carrier in a fixed bed reactor. Energy Convers Manage. 2008;49:3178-87.
[185] Tian H, Chaudhari K, Simonyi T, Poston J, Liu T, Sanders T, et al. Chemical-looping Combustion of Coal-derived Synthesis Gas Over Copper Oxide Oxygen Carriers. Energy Fuels. 2008;22:3744-55.
[186] Tian H, Guo Q, Chang J. Investigation into Decomposition Behavior of CaSO4 in Chemical-Looping Combustion. Energy Fuels. 2008;22:3915-21.
[187] Yang J-b, Cai N-s, Li Z-s. Hydrogen Production from the Steam-Iron Process with Direct Reduction of Iron Oxide by Chemical Looping Combustion of Coal Char. Energy Fuels. 2008;22:2570-9.
[188] Zhao H, Liu L, Wang B, Xu D, Jiang L, Zheng C. Sol-Gel-Derived NiO/NiAl2O4 Oxygen Carriers for Chemical-Looping Combustion by Coal Char. Energy Fuels. 2008;22:898-905.
[189] Adanez J, Dueso C, de DLF, Garcia-Labiano F, Gayan P, Abad A. Effect of Fuel Gas Composition in Chemical-Looping Combustion with Ni-Based Oxygen Carriers. 2. Fate of Light Hydrocarbons. Ind Eng Chem Res. 2009;48:2509-18.
[190] Chandel MK, Hoteit A, Delebarre A. Experimental investigation of some metal oxides for chemical looping combustion in a fluidized bed reactor. Fuel. 2009;88:898-908.
[191] Chuang SY, Dennis JS, Hayhurst AN, Scott SA. Kinetics of the chemical looping oxidation of CO by a co-precipitated mixture of CuO and Al2O3. Proc Combust Inst. 2009;32:2633-40.
[192] de DLF, Ortiz M, Garcia-Labiano F, Adanez J, Abad A, Gayan P. Hydrogen production by chemical-looping reforming in a circulating fluidized bed reactor using Ni-based oxygen carriers. J Power Sources. 2009;192:27-34.
[193] Dueso C, Garcia-Labiano F, Adanez J, de DLF, Gayan P, Abad A. Syngas combustion in a chemical-looping combustion system using an impregnated Ni-based oxygen carrier. Fuel. 2009;88:2357-64.
[194] Forero CR, Gayan P, de DLF, Abad A, Garcia-Labiano F, Adanez J. Syngas combustion in a 500 Wth Chemical-Looping Combustion system using an impregnated Cu-based oxygen carrier. Fuel Process Technol. 2009;90:1471-9.
[195] Garcia-Labiano F, de DLF, Gayan P, Adanez J, Abad A, Dueso C. Effect of Fuel Gas Composition in Chemical-Looping Combustion with Ni-Based Oxygen Carriers. 1. Fate of Sulfur. Ind Eng Chem Res. 2009;48:2499-508.

[196] Gayan P, Dueso C, Abad A, Adanez J, de DLF, Garcia-Labiano F. NiO/Al2O3 oxygen carriers for chemical-looping combustion prepared by impregnation and deposition-precipitation methods. Fuel. 2009;88:1016-23.
[197] He F, Wei Y, Li H, Wang H. Synthesis Gas Generation by Chemical-Looping Reforming Using Ce-Based Oxygen Carriers Modified with Fe, Cu, and Mn Oxides. Energy Fuels. 2009;23:2095-102.
[198] Hoteit A, Chandel MK, Durecu S, Delebarre A. Biogas combustion in a chemical looping fluidized bed reactor. Int J Greenhouse Gas Control. 2009;3:561-7.
[199] Hoteit A, Chandel MK, Delebarre A. Nickel- and copper-based oxygen carriers for chemical looping combustion. Chem Eng Technol. 2009;32:443-9.
[200] Jerndal E, Mattisson T, Lyngfelt A. Investigation of Different NiO/NiAl2O4 Particles as Oxygen Carriers for Chemical-Looping Combustion. Energy Fuels. 2009;23:665-76.
[201] Kolbitsch P, Bolhar-Nordenkampf J, Proll T, Hofbauer H. Comparison of Two Ni-Based Oxygen Carriers for Chemical Looping Combustion of Natural Gas in 140 kW Continuous Looping Operation. Ind Eng Chem Res. 2009;48:5542-7.
[202] Leion H, Larring Y, Bakken E, Bredesen R, Mattisson T, Lyngfelt A. Use of CaMn0.875Ti0.125O3 as Oxygen Carrier in Chemical-Looping with Oxygen Uncoupling. Energy Fuels. 2009;23:5276-83.
[203] Leion H, Lyngfelt A, Mattisson T. Solid fuels in chemical-looping combustion using a NiO-based oxygen carrier. Chem Eng Res Des. 2009;87:1543-50.
[204] Li F, Kim HR, Sridhar D, Wang F, Zeng L, Chen J, et al. Syngas chemical looping gasification process: oxygen carrier particle selection and performance. Energy Fuels. 2009;23:4182-9.
[205] Linderholm C, Mattisson T, Lyngfelt A. Long-term integrity testing of spray-dried particles in a 10-kW chemical-looping combustor using natural gas as fuel. Fuel. 2009;88:2083-96.
[206] Mattisson T, Leion H, Lyngfelt A. Chemical-looping with oxygen uncoupling using CuO/ZrO2 with petroleum coke. Fuel. 2009;88:683-90.
[207] Mattisson T, Lyngfelt A, Leion H. Chemical-looping with oxygen uncoupling for combustion of solid fuels. Int J Greenhouse Gas Control. 2009;3:11-9.
[208] Rubel A, Liu K, Neathery J, Taulbee D. Oxygen carriers for chemical looping combustion of solid fuels. Fuel. 2009;88:876-84.
[209] Ryden M, Johansson M, Lyngfelt A, Mattisson T. NiO supported on Mg-ZrO2 as oxygen carrier for chemical-looping combustion and chemical-looping reforming. Energy Environ Sci. 2009;2:970-81.
[210] Shen L, Wu J, Xiao J. Experiments on chemical looping combustion of coal with a NiO based oxygen carrier. Combust Flame. 2009;156:721-8.
[211] Shen L, Wu J, Xiao J, Song Q, Xiao R. Chemical-Looping Combustion of Biomass in a 10 kWth Reactor with Iron Oxide As an Oxygen Carrier. Energy Fuels. 2009;23:2498-505.
[212] Shulman A, Cleverstam E, Mattisson T, Lyngfelt A. Manganese/Iron, Manganese/Nickel, and Manganese/Silicon Oxides Used in Chemical-Looping With Oxygen Uncoupling (CLOU) for Combustion of Methane. Energy Fuels. 2009;23:5269-75.
[213] Siriwardane R, Tian H, Richards G, Simonyi T, Poston J. Chemical-Looping Combustion of Coal with Metal Oxide Oxygen Carriers. Energy Fuels. 2009;23:3885-92.
[214] Solunke RD, Veser G. Nanocomposite Oxygen Carriers for Chemical-Looping Combustion of Sulfur-Contaminated Synthesis Gas. Energy Fuels. 2009;23:4787-96.
[215] Song Q, Xiao R, Deng Z, Shen L, Zhang M. Reactivity of a CaSO4-oxygen carrier in chemical-looping combustion of methane in a fixed bed reactor. Korean J Chem Eng. 2009;26:592-602.
[216] Tian H, Guo Q. Investigation into the Behavior of Reductive Decomposition of Calcium Sulfate by Carbon Monoxide in Chemical-Looping Combustion. Ind Eng Chem Res. 2009;48:5624-32.
[217] Tian H, Simonyi T, Poston J, Siriwardane R. Effect of Hydrogen Sulfide on Chemical Looping Combustion of Coal-Derived Synthesis Gas over Bentonite-Supported Metal-Oxide Oxygen Carriers. Ind Eng Chem Res. 2009;48:8418-30.

[218] Azis MM, Jerndal E, Leion H, Mattisson T, Lyngfelt A. On the evaluation of synthetic and natural ilmenite using syngas as fuel in chemical-looping combustion (CLC). Chem Eng Res Des. 2010;88:1505-14.
[219] Brown TA, Dennis JS, Scott SA, Davidson JF, Hayhurst AN. Gasification and Chemical-Looping Combustion of a Lignite Char in a Fluidized Bed of Iron Oxide. Energy Fuels. 2010;24:3034-48.
[220] Chuang SY, Dennis JS, Hayhurst AN, Scott SA. Kinetics of the oxidation of a co-precipitated mixture of Cu and Al2O3 by O2 for chemical-looping combustion. Energy Fuels. 2010;24:3917-27.
[221] Dennis JS, Mueller CR, Scott SA. In situ gasification and CO2 separation using chemical looping with a Cu-based oxygen carrier: Performance with bituminous coals. Fuel. 2010;89:2353-64.
[222] Dennis JS, Scott SA. In situ gasification of a lignite coal and CO2 separation using chemical looping with a Cu-based oxygen carrier. Fuel. 2010;89:1623-40.
[223] Dueso C, Abad A, Garcia-Labiano F, de DLF, Gayan P, Adanez J, et al. Reactivity of a NiO/Al2O3 oxygen carrier prepared by impregnation for chemical-looping combustion. Fuel. 2010;89:3399-409.
[224] Forero CR, Gayan P, Garcia-Labiano F, de DLF, Abad A, Adanez J. Effect of gas composition in chemical-looping combustion with copper-based oxygen carriers: Fate of sulphur. Int J Greenhouse Gas Control. 2010;4:762-70.
[225] Gayan P, Forero CR, de DLF, Abad A, Garcia-Labiano F, Adanez J. Effect of gas composition in chemical-looping combustion with copper-based oxygen carriers: fate of light hydrocarbons. Int J Greenhouse Gas Control. 2010;4:13-22.
[226] Hossain MM, de LHI. Reduction and oxidation kinetics of Co-Ni/Al2O3 oxygen carrier involved in a chemical-looping combustion cycles. Chem Eng Sci. 2010;65:98-106.
[227] Hossain MM, Quddus MR, de LHI. Reduction Kinetics of La Modified NiO/La-γAl2O3 Oxygen Carrier for Chemical-Looping Combustion. Ind Eng Chem Res. 2010;49:11009-17.
[228] Iggland M, Leion H, Mattisson T, Lyngfelt A. Effect of fuel particle size on reaction rate in chemical looping combustion. Chem Eng Sci. 2010;65:5841-51.
[229] Jerndal E, Mattisson T, Thijs I, Snijkers F, Lyngfelt A. Investigation of NiO/NiAl2O4 oxygen carriers for chemical-looping combustion produced by spray-drying. International Journal of Greenhouse Gas Control. 2010;4:23-35.
[230] Jing C, Dejie C. Thermodynamic and kinetic analysis of Ca-based oxygen carrier in chemical-looping combustion. Int J Chem React Eng. 2010;8:No pp. given.
[231] Kierzkowska AM, Bohn CD, Scott SA, Cleeton JP, Dennis JS, Muller CR. Development of Iron Oxide Carriers for Chemical Looping Combustion Using Sol-Gel. Ind Eng Chem Res. 2010;49:5383-91.
[232] Liu S, Lee D, Liu M, Li L, Yan R. Selection and Application of Binders for CaSO4 Oxygen Carrier in Chemical-Looping Combustion. Energy Fuels. 2010;24:6675-81.
[233] Markstroem P, Berguerand N, Lyngfelt A. The application of a multistage-bed model for residence-time analysis in chemical-looping combustion of solid fuel. Chem Eng Sci. 2010;65:5055-66.
[234] Moghtaderi B, Song H. Reduction Properties of Physically Mixed Metallic Oxide Oxygen Carriers in Chemical Looping Combustion. Energy Fuels. 2010;24:5359-68.
[235] Noorman S, Gallucci F, van SAM, Kuipers HJAM. Experimental Investigation of a CuO/Al2O3 Oxygen Carrier for Chemical-Looping Combustion. Ind Eng Chem Res. 2010;49:9720-8.
[236] Ortiz M, de DLF, Abad A, Garcia-Labiano F, Gayan P, Adanez J. Hydrogen production by auto-thermal chemical-looping reforming in a pressurized fluidized bed reactor using Ni-based oxygen carriers. Int J Hydrogen Energy. 2010;35:151-60.
[237] Park J-N, Zhang P, Hu Y-S, McFarland EW. Synthesis and characterization of sintering-resistant silica-encapsulated Fe3O4 magnetic nanoparticles active for oxidation and chemical looping combustion. Nanotechnology. 2010;21:225708/1-/8, S/1-S/5.
[238] Pimenidou P, Rickett G, Dupont V, Twigg MV. High purity H2 by sorption-enhanced chemical looping reforming of waste cooking oil in a packed bed reactor. Bioresour Technol. 2010;101:9279-86.

[239] Pimenidou P, Rickett G, Dupont V, Twigg MV. Chemical looping reforming of waste cooking oil in packed bed reactor. Bioresour Technol. 2010;101:6389-97.
[240] Proell T, Bolhar-Nordenkampf J, Kolbitsch P, Hofbauer H. Syngas and a separate nitrogen/argon stream via chemical looping reforming - A 140kW pilot plant study. Fuel. 2010;89:1249-56.
[241] Ryden M, Johansson M, Cleverstam E, Lyngfelt A, Mattisson T. Ilmenite with addition of NiO as oxygen carrier for chemical-looping combustion. Fuel. 2010;89:3523-33.
[242] Shen L, Gao Z, Wu J, Xiao J. Sulfur behavior in chemical looping combustion with NiO/Al2O3 oxygen carrier. Combust Flame. 2010;157:853-63.
[243] Siriwardane R, Tian H, Miller D, Richards G, Simonyi T, Poston J. Evaluation of reaction mechanism of coal-metal oxide interactions in chemical-looping combustion. Combust Flame. 2010;157:2198-208.
[244] Solunke RD, Veser G. Hydrogen Production via Chemical Looping Steam Reforming in a Periodically Operated Fixed-Bed Reactor. Ind Eng Chem Res. 2010;49:11037-44.
[245] Sun X, Xiang W, Wang S, Tian W, Xu X, Xu Y, et al. Investigation of coal fueled chemical looping combustion using Fe3O4 as oxygen carrier: Influence of variables. J Therm Sci. 2010;19:266-75.
[246] Tian H, Guo Q, Yue X, Liu Y. Investigation into sulfur release in reductive decomposition of calcium sulfate oxygen carrier by hydrogen and carbon monoxide. Fuel Processing Technology. 2010;91:1640-9.
[247] Zheng M, Shen L, Xiao J. Reduction of CaSO4 oxygen carrier with coal in chemical-looping combustion: Effects of temperature and gasification intermediate. Int J Greenhouse Gas Control. 2010;4:716-28.
[248] Zhu X, Wang H, Wei Y, Li K, Cheng X. Hydrogen and syngas production from two-step steam reforming of methane over CeO2-Fe2O3 oxygen carrier. Journal of Rare Earths. 2010;28:907-13.
[249] Abad A, Adanez J, Cuadrat A, Garcia-Labiano F, Gayan P, de DLF. Kinetics of redox reactions of ilmenite for chemical-looping combustion. Chem Eng Sci. 2011;66:689-702.
[250] Gu H, Shen L, Xiao J, Zhang S, Song T. Chemical Looping Combustion of Biomass/Coal with Natural Iron Ore as Oxygen Carrier in a Continuous Reactor. Energy Fuels. 2011;25:446-55.
[251] Keller M, Leion H, Mattisson T, Lyngfelt A. Gasification inhibition in chemical-looping combustion with solid fuels. Combust Flame. 2011;158:393-400.
[252] Mendiara T, Johansen JM, Utrilla R, Geraldo P, Jensen AD, Glarborg P. Evaluation of different oxygen carriers for biomass tar reforming (I): Carbon deposition in experiments with toluene. Fuel. 2011;90:1049-60.
[253] Mendiara T, Johansen JM, Utrilla R, Jensen AD, Glarborg P. Evaluation of different oxygen carriers for biomass tar reforming (II): Carbon deposition in experiments with methane and other gases. Fuel. 2011;90:1370-82.
[254] Müller CR, Bohn CD, Song Q, Scott SA, Dennis JS. The production of separate streams of pure hydrogen and carbon dioxide from coal via an iron-oxide redox cycle. Chemical Engineering Journal. 2011;166:1052-60.
[255] Mihai O, Chen D, Holmen A. Catalytic consequence of oxygen of lanthanum ferrite perovskite in chemical looping reforming of methane. Ind Eng Chem Res. 2011;50:2613-21.
[256] Ryden M, Lyngfelt A, Mattisson T. CaMn0.875Ti0.125O3 as oxygen carrier for chemical-looping combustion with oxygen uncoupling (CLOU)-Experiments in a continuously operating fluidized-bed reactor system. Int J Greenhouse Gas Control. 2011;5:356-66.
[257] Saha C, Roy B, Bhattacharya S. Chemical looping combustion of Victorian brown coal using NiO oxygen carrier. Int J Hydrogen Energy. 2011;36:3253-9.
[258] Solunke RD, Veser G. Integrating desulfurization with CO2-capture in chemical-looping combustion. Fuel. 2011;90:608-17.
[259] Shulman A, Cleverstam E, Mattisson T, Lyngfelt A. Chemical - Looping with oxygen uncoupling using Mn/Mg-based oxygen carriers - Oxygen release and reactivity with methane. Fuel. 2011;90:941-50.

[260] Wen D, Song P, Zhang K, Qian J. Thermal oxidation of iron nanoparticles and its implication for chemical-looping combustion. J Chem Technol Biotechnol. 2011;86:375-80.
[261] Bolhar-Nordenkampf J, Proell T, Kolbitsch P, Hofbauer H. Performance of a NiO-based oxygen carrier for chemical looping combustion and reforming in a 120kW unit. Energy Procedia. 2009;1:19-25.
[262] Xiang W, Wang S, Di T. Investigation of Gasification Chemical Looping Combustion Combined Cycle Performance. Energy Fuels. 2008;22:961-6.
[263] Rezvani S, Huang Y, McIlveen-Wright D, Hewitt N, Mondol JD. Comparative assessment of coal fired IGCC systems with CO2 capture using physical absorption, membrane reactors and chemical looping. Fuel. 2009;88:2463-72.
[264] Cormos C-C. Evaluation of power generation schemes based on hydrogen-fuelled combined cycle with carbon capture and storage (CCS). International Journal of Hydrogen Energy. 2011;36:3726-38.
[265] Kobayashi N, Fan L-S. Biomass direct chemical looping process: A perspective. Biomass Bioenergy. 2011;35:1252-62.

Appendix A

Literature summary of experimental work on oxygen carriers

Ref.	Oxygen carriers	synthesis	Apparatus	Fuel	Dp(mm)	T_{red}(°C)	
Ishida and Jin 1994 [26]	N, NYSZ, FYSZ	MM	TGA	H_2 H_2O	1.3-2.8	550-950	a
Ishida et al. 1996 [27]	NYSZ	SG DM	TGA	H_2	1.0-3.2	600-1000	a, b
Ishida and Jin 1996[23]	NYSZ	MM	TGA	H_2	2	600	
Hatanka et al. 1997[137]	N	-	FxB	CH_4	0.074	400-700	
Ishida and Jin 1997[28]	FYSZ, NA, NYSZ	MM	TGA	H_2 CH_4 H_2O	2	600-750	c
Ishida et al. 1998 [29]	NYSZ, NA, FYSZ, FA, NT, FT	DM MM	TGA	H_2 CO N_2 CO_2 H_2O	1.6	550-900	c
Jin et al. 1998 [30]	NYSZ, CoYSZ, FYZ, NCoYSZ	DM	TGA	H_2 CH_4	1	600	c, d
Jin et al. 1999 [31]	NTi, FTi, CoTi, NA, NMg, FA, CoA, CoO/MgO, NAN, NYSZ, Fe_2O_3/MgO	MM DM	TGA	H_2 CH_4 H_2O	1.8	600,700	c, e
Mattisson et al. 2000[138]	F, FA, Natural Iron ore, Fe_3O_4	MM	FxB	CH_4	0.125-0.5	950	
Jin and Ishida 2001[21]	N,NYSZ, NAN	DM	TGA FxB	H_2 Ar	1.8, 2.1,4	600	e
Mattisson et al. 2001[55]	Natural Iron ore	-	FxB	CH_4	0.18-0.25	950	
Ryu et al. 2001 [139]	Nbe	MM	TGA	CH_4 N_2	0.08	650-900	b
Ishida et al. 2002[140]	NAN	DM	TGA CFzB	H_2 Ar	0.097	600-1200	
Jin and Ishida 2002 [141]	NYZ, NAN, NcoYZ	DM	FxB	CH_4 H_2O	4.0	600-800	c, e
Mattisson et al. 2003[47]	CA, CoA, MA, NA	DI	TGA	CH_4 CO_2 H_2O	0.1-0.5	750-950	f
Ryu et al. 2003 [142]	NBe	MM	TGA FxB	CH_4 N_2 H_2	0.4,0.128,0.091	500-1000	c
Ryu et al. 2003 [143]	NBe	MM	TGA	CH_4 N_2	0.091	650-1000	c
Song et al. 2003[144]	NiO/hexaaluminate	WI	TGA	H_2 Ar	-	0-1000	
Villa et al. 2003 [145]	NAN, NAM	CP	TGA	CH_4 H_2 He H_2O	-	0-1000	c
Adanez et al. 2004 [24]	CA, CSe, CSi, CTi, CZr, FA, FSe, FSi, FTi, FZr, MA, MSe, MSi, MTi, MZr, NA, NSe, NSi, NTi, NZr	MM	TGA	CH_4 H_2O	2	800-950	
Adanez et al. 2004 [146]	CA, CSi, CTi, CZr, FA, FSi, FTi, FZr, MA, MSi, MTi, MZr, NA, NSi, NTi, NZr	MM WI CP	TGA FzB	CH_4 N_2 H_2O	0.1-0.3	800-950	
Cho et al. 2004 [42]	FA, FAS, Fe_2O_3/kaolin, NAN MAMn, $CuO/CuAl_2O_4$	FG	FzB	CH_4 H_2O	0.125-0.180	850-950	f
de Diego et al. 2004 [22]	CSi, CTi, CZr, CA, CSe	MM,WI, CP	TGA	CH_4 H_2 CO H_2O	2, 0.2-0.4	800	
Garcia-Labiano et al. 2004 [125]	CA	WI	TGA	CH_4 H_2 CO CO_2 H_2O	0.1-0.3	450-800	b, f
Jin and Ishida 2004 [25]	NAN, NCoYZ	DM	FxB	CO H_2 CO_2 H_2O CH_4 Ar	4	600-1000	c, e
Johansson et al. 2004[54]	FAM	FG	FzB	CH_4 H_2O	0.09-0.125,0.125-0.18,0.18-0.25	650-950	a, f
Mattisson et al. 2004[56]	FA, FAK, FAM, FZr, FTi	FG	FzB	CH_4 H_2O	0.125-0.180	950	f
Brandvoll 2005[147]	NAN, Perovskite	DM	FxB FzB	H_2 CH_4 CH_4 H_2O	0.106-0.212	750-869	
Cho et al. 2005 [148]	NAN, FA	FG	FzB	CH_4 CH_4 H_2O	0.125-0.18	750-950	c
Corbella et al. 2005 [43]	CTi	DI	FxB	CH_4	0.2-0.4	800-900	
Corbella et al. 2005 [44]	NTi	DI	FxB	CH_4	0.2-0.4	900	c
de Diego et al. 2005 [45]	CA	WI DI	TGA FzB	H_2 CH_4 N_2	0.1-0.32	800-950	g, h
De los Rios et al. 2005[149]	Co_xTiO_y	MM	TGA	H_2 AR	-	700	i
Ishida et al. 2005 [150]	FA	SD	TGA	H_2	0.07	900	g
Lee et al. 2005 [151]	CoYZ, FYZ, N, NZr, NYZ, NAN, $NiO/AlPO_4$	SG DM	TGA	H_2	2	600	

Lyngfelt and Thunman 2005 [90]	Ni-based, Fe-based	-	cFzB	NG	-	560-900	f, h, j
Readman et al. 2005 [152]	$La_{0.8}Sr_{0.2}Co_{0.2}Fe_{0.8}O_{3-\delta}$	citric-acid method	TGA	H_2 He	-	800	
Zafar et al. 2005[50]	NSi, CSi, MSi, FSi	DI	FzB	CH_4 H_2O	0.18-0.25	700-950	i
Abad et al. 2006 [40]	MZrMg	FG	CFzB	NG, Syngas	0.09-0.212	800-950	f , h, j
Adanez et al. 2006 [41]	NA, $NiO/CuAl_2O_4$, CA	DI	TGA FxB FzB	CH_4 CO H_2 H_2O N_2	0.1-0.3	950	d, h
Adanez et al.2006 [95]	CA	DI	CFzB TGA	CH_4 N_2	0.1-0.3,0.2-0.5	700-800	a, h, j
Cao et al. [39]	C	-	TGA	PRB Coal Wood, Polyethene, N_2, CO_2	0.05-0.15	0-1000	k
Cho et al. 2006 [78]	FA, NAN, MZrMg	FG	FzB	CH_4	0.125-0.18	950	c, g
Corbella et al. 2006 [38]	NTi	DI	FxB	CH_4 N_2	0.2-0.4	900	c
Corbella et al. 2006 [49]	CSi	WI	FxB	CH_4	0.2-0.4	800	
Garcia-Labiano et al. 2006 [46]	FA, NA, CA	FG I	TGA	H_2 CO CO_2 N_2	0.15-0.2	450-950	b, e
Johansson et al. 2006 [93]	NAM	FG	CFzB	NG	0.09-0.212	800-950	h, j
Johansson et al. 2006 [33]	NAN, NAM	FG	CFzB FzB	NG Syngas	0.09-0.212	800-950	h, j
Johansson et al. 2006 [153]	FSi, FZr, FABe, FAM, MSi, MZr, MZrCa, MZrMg, MZrCe, NAN, $NiO/Ca\text{-}NiAl_2O_4$, NBe, NAM, NMg	FG	FzB	CH_4 H_2O	0.125-0.180	950	
Johansson et al. 2006 [77]	MZr, MzrCa, MZrMg, MzrCe	FG	FzB	CH_4 H_2O	0.125-0.180	950	
Johansson et al. 2006 [154]	NAN	FG	FzB CFzB	CH_4 H_2O	0.090-0.212	750-950	g, h, j
Johansson et al. 2006 [155]	NAM, FAM	FG	FzB	CH_4 H_2O	0.125-0.180	650-950	c, d
Mattisson et al. 2006 [34]	NAN, $NiO/NiAl_2O_4$-Kaolin, NAM, NTi, NZr	FG	FzB	CH_4 H_2O	0.18-0.25	950	
Readman et al. 2006 [156]	NAN	DM	TGA	CH_4 H_2	0.09-0.21	800	B
Ryden et al. 2006 [157]	NAM	FG	CFzB	NG H_2O	0.09-0.212	820-930	c h i j
Scott et al. 2006 [158]	Fe_2O_3	-	FzB	Lignite H_2O CO_2 N_2	0.3-0.71	900	k
Son and Kim 2006 [159]	NTi, FTi, NA, FA	MM	TGA CFzB	CH_4 H_2O CO_2 N_2	0.106-0.150	650-950	b,d, j
Song et al. 2006 [160]	NAN	SG	TGA	H_2	1-2	600	
Zafar et al. 2006 [51]	NAM, FAM, MAMg, NSi, FSi, CSi, MSi, $CuO/MgAl_2O_4$	FG DI	TGA	CH_4 H_2O CO_2 N_2	0.18-0.25	800-1000	f,i
Abad et al. 2007 [161]	FA	FG	CFzB FzB	NG CH_4 Syngas	0.09-0.212	800-950	f, j
Abad et al. 2007 [162]	CA, FA, NAN	I FG	TGA	CH_4 CO H_2 H_2O CO_2	0.15-0.2	500-950	b,e,f
Abad et al. 2007 [59]	CA, FA, NAN	I FG	TGA	H_2 CO N_2 CO_2 H_2O	0.15-0.2	450-950	b,e,f
Corbella et al. 2007 [163]	F, FTi,	DI	FxB	CH_4	0.2-0.4	900	
de Diego et al. 2007 [164]	CA	DI	TGA CFzB	CH_4 N_2 H_2O	0.1-0.3 0.2-0.5	700-800	a, h, j
Erri and Varma 2007 [165]	NAN, $NiO/Ni_{1-x}Mg_xAl_2O_4$	solution combustion	TGA	CH_4 H_2O Ar	0.21-0.43	800-1200	
Erri and Varma 2007 [166]	NAN, $NiO/Ni_{1-x}Mg_xAl_2O_4$	solution combustion	TGA	CH_4 H_2 CO CO_2 H_2 Ar	0.21-0.43	800-1200	
Hossain et al. 2007 [167]	NAN, $CoO\text{-}NiO/NiAl_2O_4$	DI	FzB	CH_4	0.06-0.1	680	d
Hossain and Lasa 2007 [168]	NA, $CoO\text{-}NiO/Al_2O_3$	DI	FzB	CH_4	0.07	650	b, d
Jin et al. 2007 [169]	NBe, FBe, $NiO\text{-}Fe_2O_3$/bentonite	MM	FzB	H_2 CO N_2	0.09-0.212	800-900	i
Leion et al. 2007 [170]	FAM	FG	FzB	Coke H_2O	0.09-0.125	850-	a,f,g

				syngas	0.18-0.25	1000	,k,l
Siriwardane et al. 2007 [130]	NBe	MM	TGA	CO_2 CO H_2O H_2	0.074-0.84	700-900	a,e
Zafar et al. 2007 [171]	NAM	FG	TGA	CH_4 H_2O N_2	0.125-0.18	800-1000	b, f
Zafar et al. 2007 [172]	MZrMg	FG	TGA	CH_4 H_2O N_2	0.09-0.25	800-950	a, b, f
Berguerand and Lyngfelt 2008 [62]	Ilmenite	-	CFzB	petroleum coke	0.09-0.25	950	h, j, k
Berguerand and Lyngfelt 2008 [61]	Ilmenite	-	CFzB	South African coal	0.09-0.25	950	j, k
Chuang et al. 2008 [48]	CA	MM WI CP	FzB	CO N_2	0.5-0.71	800-900	
de Diego et al. 2008 [35]	NA	DI DP	TGA FzB	CH_4 H_2O N_2	0.1-0.3	800-950	i
Gao et al. 2008 [173]	NAN	DI	FzB	bituminous coal, H_2O	0.3-0.45	800-960	k
Gayan et al. 2008 [36]	NA, NAM, $NiO/CaAl_2O_4$	DI	TGA FzB	CH_4 H_2O N_2	0.1-0.3, 0.1-0.5	800-950	h
Johansson et al. 2008 [32]	NAN, NAM	FG	FzB	CH_4 H_2O	0.125-0.18	950	c, i
Leion et al. 2008 [65]	ilmenite	-	FzB	CH_4 CO H_2	0.125-0.18	970-980	
Leion et al. 2008 [174]	CZr	FG	FzB	German lignite	0.125-0.18	850-985	k
Leion et al. 2008 [66]	FAM, ilmenite	FG	FzB	Coke coals N_2 H_2O H_2 CO	0.09-0.125	850-1000	k
Li et al. 2008 [175]	F	-	MvB TGA	CH_4 Coal	-	-	i, k
Linderholm et al. 2008 [176]	NAN	Spin flash	CFzB	NG N_2 H_2O	0.125-0.18	660-950	g, h, j
Mattisson et al. 2008 [177]	NAN	FG	TGA FzB	CH_4 H_2O CO_2 N_2	0.09-0.125,0.125-0.18,0.18-0.25	750-950	a,b, c
Ryden et al. 2008 [178]	NAM, NAN	FG, DI	CFzB	NA CO_2 H_2O N_2	0.09-0.212 0.09-0.25	800-960	c, i, j
Ryden et al. 2008 [58]	NAM, FAM, MZrMg, $La_xSr_{1-x}Fe_yCo_{1-y}O_{3-\delta}$	glycine-nitrate combustion, SD	FxB	CH_4 Ar	0.15-0.25, 0.09-0.15 0.09-0.125	900	c, d, i
Sedor et al. 2008 [179]	NA	DI	FzB	CH_4	0.01-0.11	600-680	b
Sedor et al. 2008[180]	NA	DI	FzB	CH_4	0.095	680	
Shen et al. 2008 [181]	$CaSO_4$	-	TGA	CO H_2 N_2	0.05-0.1	850-1050	l
Song et al. 2008 [182]	natural anhydrite ore	-	FzB	H_2 CO CO_2	0.15-0.2	950	l
Song et al. 2008 [183]	natural anhydrite ore	-	FzB	H_2 CO CO_2	0.15-0.2	890-950	b,c,l
Song et al. 2008 [184]	natural anhydrite ore	-	FxB	CH_4	0.2-0.8	850-1000	a,l
Tian et al. 2008 [185]	CBe, CBHA	MM	TGA FxB	CO_2 CO He H_2	-	700-900	a,b,e
Tian et al. 2008 [186]	$CaSO_4$	-	TGA	CO_2 N_2 CO	0.005-0.05	850-1200	b
Yang et al. 2008 [187]	F	-	FzB	Lignite Ar H_2O CO_2	0.2-0.45	25-900	i,k
Zhao et al. 2008 [188]	NAN	SG	TGA	Coal H_2 N_2	0.125-0.18	850-900	k
Adanez et al. 2009 [189]	NA	DI	TGA FzB CFzB	CH_4 C_2H_6 C_3H_8 H_2O N_2	0.1-0.3	700-950	c,j
Adanez et al. 2009 [91]	NA	DI	TGA CFzB	CH_4 N_2	0.1-0.3	800-880	c,f,h ,j
Berguerand and Lyngfelt 2009 [63]	ilmenite	-	CFzB	petroleum coke, N_2, H_2O	0.125-0.25	950-1000	k,l
Chandel et al. 2009 [190]	NAN, $Cu_{0.95}Fe_{1.05}AlO_4$,CuO-$Cu_{0.95}Fe_{1.05}AlO_4$	-	FzB	CH_4 H_2O	0.1-0.3	800-900	c,d,g
Chuang et al. 2009 [191]	CA, Cu_2O/Al_2O_3	CP	FzB	CO N_2	0.355-0.5,0.85-1	250-900	a, b
de Diego et al. 2009 [192]	NA	DI	TGA CFzB	CH_4 H_2O N_2	-	800-900	i, j
Dueso et al. 2009 [193]	NA	DI	TGA FzB CFzB	CO H_2 CO_2 N_2	0.1-0.3	800-950	j
Forero et al. 2009 [194]	CA	DI	TGA CFzB	H_2 CO CO_2 H_2O	0.3-0.5	800-880	f, j
Garcia-Labiano et al. 2009 [195]	NA	DI	CFzB	CH_4 N_2 H_2S	0.1-0.3	830-870	j,l
Gayan et al. 2009 [196]	NA	DI DP	TGA FzB	CH_4 H_2O N_2	0.1-0.3	950	g, h
He et al. 2009 [197]	CeO_2, C, F, Mn_2O_3	CP	TGA FxB	CH_4	0.004-0.01	200-1000	d, i
Hoteit et al. 2009 [198]	NAN, $Cu_{0.95}Fe_{1.05}AlO_4$	-	TGA FzB	CH_4 CO_2 N_2	0.171,0.15	800-900	i

				O_2			
Hoteit et al. 2009 [199]	NAN, $Cu_{0.95}Fe_{1.05}AlO_4$	-	FzB	CH_4 H_2O	0.171, 0.234	800-900	c
Jerndal et al. 2009 [200]	NA, NAM, NiO/Al_2O_3-$Ca(OH)_2$	FG	FzB	CH_4	0.125-0.18	950	c, d
Kolbitsch et al. 2009 [201]	NAN, NAM	-	CFzB	NG	-	800-950	j
Leion et al. 2009 [71]	Iron ore, oxide scale from steel production	-	FzB	H_2O, N_2, CO, H_2, coal, petroleum coke	0.09-0.125 0.125-0.18	900-1000	k
Leion et al. 2009 [202]	$CaMn_{0.875}Ti_{0.125}O_3$	spray pyrolysis, FG	TGA,FzB	CH_4 CO_2 H_2 Ar coke H_2O N_2	0.09-0.125 0.125-0.18	800-1000	k
Leion et al. 2009 [203]	NAN	Spin flash	FzB	CH_4 H_2 CO N_2 H_2O coke coal	0.125-0.18 0.09-0.125	970	k, l
Leion et al. 2009 [74]	Fe-, Mn-based ores and industrial products	FG	FzB	CO H_2 CH_4	0.125-0.18	930-950	
Li et al. 2009 [204]	F, FA	SG	TGA FxB	H_2 N_2 CO_2 CO H_2O	0.71-1	830,900	h, i
Linderholm et al. 2009 [205]	NAN, NAM	SD	CFzB	NG	0.125-0.18	700-950	f,g,h ,j
Mattisson et al. 2009 [206]	CZr	FG	FzB	Petroleum coke,N_2	0.125-0.18	880-985	f, k
Mattisson et al. 2009 [207]	CA	FG	FzB	CH_4, petroleum coke, N_2	0.125-0.18	950-985	k
Proell et al. 2009 [97]	NAN, NAM	SD	CFzB	NG H_2O C_3H_8	0.135	800-950	j
Rubel et al. 2009 [208]	N, F, Co, Cu	-	TGA	H_2 CO CO_2 Ar coal	-	800-950	k
Ryden et al. 2009 [75]	Fe-based industry waste with Ni	FG	FzB	CH_4	0.125-0.18	800-950	d
Ryden et al. 2009 [209]	NMgZr	FG	FzB CFzB	CH_4 H_2O N_2 NG	0.125-0.18 0.09-0.212	670-950	i,j
Shen et al. 2009 [98]	NA	CP	CFzB	Coal H_2O CO_2	0.2-0.4	920-980	j, k, l
Shen et al. 2009 [210]	NAN	I	CFzB	Coal H_2O CO_2	0.2-0.4	870-970	j, k
Shen et al. 2009 [211]	F	-	CFzB	Biomass H_2O CO_2	0.3-0.6	740-920	j, k
Shulman et al. 2009 [212]	Mn_3O_4-Fe_2O_3, Mn_3O_4-NiO, MSi	FG	FzB	CH_4 N_2	0.125-0.18	810-900	d
Siriwardane et al. 2009 [213]	Cu, N, Mn_2O_3, F, Co	-	TGA FxB	Coal Ar N_2 CO_2	0.005-0.07	25-1000	k
Solunke and Veser 2009 [214]	NBHA, CBHA	SG-based	TGA	H_2 CO CO_2 He H_2S	0.01-1	300-800	l
Son et al. 2009 [52]	CA, CSi	MM WI CP	TGA	H_2 CO	0.09-0.21	350-850	b, i
Song et al. 2009 [215]	$CaSO_4$	-	FxB	CH_4	0.15-0.2	950	c, l
Tian and Guo 2009 [216]	$CaSO_4$	-	TGA	CO_2 N_2 CO	0.0089	20-1200	b, l
Tian et al. 2009 [217]	CBe, NBe, Mn_2O_3/betonite, FBe	MM	TGA	CO_2 CO H_2 He H_2S	0.075-0.089, 0.251-0.5	800-900	a, l
Adanez et al. 2010[67]	ilmenite	-	TGA	CH_4 H_2 CO CO_2 H_2O N_2	0.15-0.30	900	f
Azis et al. 2010 [218]	Ilmenite	FG	FzB	CO H_2	0.125-0.18	950	
Berguerand and Lyngfelt 2010 [64]	Ilmenite	-	CFzB	Petroleum coke, coal, H_2O	0.125-0.25	950-1030	k,j
Brown et al. 2010 [219]	F	-	FzB	Lignite CO_2 N_2 CO	0.3-0.425	800	b, k
Chuang et al. 2010 [220]	CA	CP	FzB	N_2 O_2	0.355-0.5, 0.85-1	300-750	a,b
Dennis et al. 2010 [221]	CA	DI	FzB	Bituminous coals, lignite N_2 CO_2	0.71-1.119	900-977	b, k
Dennis and Scott 2010 [222]	CA	DI	FzB	lignite coal N_2 CO_2	0.6-1.19	900	b, k
Dueso et al. 2010 [223]	NA	DI	FzB TGA	CH_4 H_2 N_2	0.1-0.3	950	f
Forero et al. 2010 [224]	CA	DI	CFzB	CH_4 N_2 H_2 H_2S	0.3-0.5	800	j, l
Gayan et al. 2010 [225]	CA	DI	CFzB TGA FzB	CH_4 C_2H_6 C_3H_8 H_2O N_2	0.3-0.5	700-880	c, j
Hossain and Lasa 2010 [226]	CoO-NiO/Al_2O_3	DI	FzB	H_2 CH_4	0.01-0.11	550-650	b, d
Hossain et al. 2010 [227]	NiO/La-Al_2O_3	DI	FzB	H_2 CH_4	0.05-0.11	550-680	b, d
Iggland et al. 2010 [228]	ilmenite	FG	FzB	Petroleum	0.125-0.18	970	k

				coke, coal, wood, char, H_2O,N_2			
Jerndal et al. 2010 [229]	NA	SD	FzB	CH_4	0.125-0.18	950	g
Jing et al. 2010 [230]	$CaSO_4$	-	TGA	H_2 N_2	0.0089	900-1100	b
Kierzkowska et al. 2010 [231]	F,FA	SG	FxB	CO N_2 CO_2	0.3-0.425	850	i
Kolbitsch et al. 2010 [60]	Ilmenite, Ni-based	-	CFzB	CO H_2 CH_4	0.2-0.3	850-900	j
Ksepko et al. 2010 [37]	NSi, NZr, NTi, NSe	MM	TGA	H_2 CO He CO_2 H_2S	<0.25	800-900	l
Linderholm et al. 2010 [92]	NAN, NAM	SD DI FG	CFzB FzB	NG CH_4	0.125-0.18	750-950	d, j
Liu et al 2010 [232]	$CaSO_4/Al_2O_3$, $CaSO_4/ZrO_2$, $CaSO_4/SiO_2$	MM	TGA	CH_4 H_2 CO N_2	0.125-0.25	840-950	
Markstroem et al. 2010 [233]	Ilmenite	-	CFzB	Coke coal H_2O N_2	0.125-0.25	950-970	f, j, k
Moghtaderi and Song 2010 [234]	CA, NA, FA	MM	TGA	H_2 CO CH_4 Ar	0.09-0.106	500-950	b, d
Noorman et al. 2010 [235]	CA	-	TGA	H_2 N_2	1.1	500-900	b
Noorman et al. 2010 [86]	CA	-	PcB	CH_4 N_2	1.1	650-850	
Ortiz et al. 2010 [236]	NA	DI	TGA FzB	CH_4 H_2O N_2	0.1-0.5	800-900	e, i
Park et al. 2010 [237]	FSi	microemulsion-based	FxB TGA	CO Ar CH_4 N_2	0.25-0.4	25-500	
Pimenidou et al. 2010 [238]	NA	-	PcB	waste cooking oil, H_2O	0.85-2	600	i
Pimenidou et al. 2010 [239]	NA	-	PcB	waste cooking oil, H_2O	0.85-2	600-700	i
Proell et al. 2010 [240]	NAN, NAM	-	CFzB	NG	-	750-900	i, j
Ryden et al. 2010 [57]	FZrMg, FZrCe, FZrCa, NAM	FG	FzB	CH_4	0.09-0.25	800-950	a, d
Ryden et al. 2010 [241]	Ilmenite, NA, NAM	FG DI	FzB CFzB	CH_4 H_2O NG	0.09-0.125 0.125-0.18	780-950	g, j
Shen et al. 2010 [242]	NA	CP	TGA CFzB	CO H_2 H_2S N_2	0.1-0.3	850-930	j, l
Shen et al. 2010 [82]	NA	CP	CFzB	Coal N_2 H_2O	0.1-0.3	900-985	j, l
Siriwardane et al. 2010 [243]	C	-	TGA	Coal CO CO_2 H_2 He CH_4	0.005-0.595	25-1000	a, k
Solunke and Veser 2010 [244]	FBHA	SG-based	FxB	H_2 CO_2 CO He	-	500-800	i
Sun et al. 2010 [245]	F	-	TGA	Coal N_2	<0.075	25-950	k
Tian et al. 2010 [246]	$CaSO_4$	-	TGA	H_2 CO N_2 CO_2	-	800	e,l
Xiao et al. 2010 [70]	Iron ore	-	FxB	Coal H_2O N_2	0.09-0.125	970	e, k
Xiao et al. 2010 [72]	Iron ore	-	FxB	Coal H_2O N_2	0.09-0.125	970	e, k
Zheng et al. 2010 [247]	$CaSO_4$	-	FzB	Coal H_2O CO_2	0.3-0.5	850-980	k, l
Zhu et al. 2010 [248]	Fe_2O_3-CeO_2	CP	FxB	CH_4 Ar	0.4-0.841	450-900	i
Abad et al. 2011 [249]	ilmenite	-	TGA	H_2 CO CH_4 H_2O CO_2	0.15-0.3	800-950	b, f
Gu et al. 2011 [250]	Iron ore	-	CFzB	Biomass, coal, N_2, H_2O	0.1-0.3	720-980	j, k
Keller et al. 2011 [251]	Iron oxide scales, ilmenite	-	FzB	Char CO H_2 H_2O N_2	-	970	k
Mendiara et al. 2011[252]	NAM, NAN, MZrMg, FTi	FG	TGA FxB	C_7H_8 N_2	0.18-0.212	600-800	c, i
Mendiara et al. 2011 [253]	NAM, NAN, MZrMg, FTi	FG	TGA FxB	CH_4 H_2O C_7H_8	0.18-0.212	600-800	c, i
Muller et al. 2011 [254]	F	MM	FxB	Coal	0.425-0.600	800-850	i,k
Mihai et al. 2011 [255]	$LaFeO_3$, perovskite	Solution combustion	FxB	CH_4 Ar	0.075-0.15	780-900	i
Noorman et al. 2011 [87]	CA, $CaTi_{0.125}Mn_{0.875}O_3$	-	PcB TGA	CH_4 N_2 H_2O	2-4	500-800	e, c
Ortiz et al. 2011 [76]	Iron-based waste product	-	CFzB TGA	CH_4 H_2 CO CO_2 H_2O N_2	0.1-0.3	830-950	f, i, j
Ryden et al. 2011 [256]	$CaTi_{0.125}Mn_{0.875}O_3$	spray pyrolysis	CFzB	NG	0.09-0.212	620-970	c, f, j, m
Saha et al. 2011 [257]	N	-	TGA	Coal,CO2,N2	0.1-0.15	950	h, k
Solunke and Veser 2011 [258]	CBHA	SG-based	FxB	H_2 CO CO_2 He H_2S	-	600-900	l
Shulman et al. 2011 [259]	MnO_2/MgO, MnO_2/MgO-$Ca(OH)_2$,	FG	FzB	CH_4	0.125-0.18	810-950	m

	Mn_3O_4/MgO, MnO_2/MgO-TiO_2						
Wen et al. 2011 [260]	iron nanoparticles	-	TGA	Only oxidation	0.0001	25-700	b

a effect of particle size on reduction/oxidation
b study on kinetics
c study of carbon deposition
d Synergetic Combination
e effect of pressure
f the solid inventory and circulation rate
g de-fluidization study
h attrition and life time estimation
i Chemical looping reforming
j prototype
k study on solid fuel
l study on sulfur
m Chemical looping with oxygen uncoupling

Oxygen Carrier Acronyms

C	copper oxide, CuO
CA	CuO/Al_2O_3
CBe	CuO/bentonite
CBHA	CuO/barium-hexaaluminate
Co	cobalt oxide, CoO
CoA	CoO/Al_2O_3
CoTi	CoO/TiO_2
CoYSZ	CoO/YSZ
CSe	CuO/sepiolite
CSi	CuO/SiO_2
CTi	CuO/TiO_2
CZr	CuO/ZrO_2
F	iron oxide, Fe_2O_3
FA	Fe_2O_3/Al_2O_3
FABe	Fe_2O_3/Al_2O_3 with bentonite
FAK	Fe_2O_3/Al_2O_3 with Kaolin as additive
FAS	Fe_2O_3/Al_2O_3 with Starch as additive
FBe	Fe_2O_3/bentonite
FBHA	Fe_2O_3/barium-hexaaluminate
FSe	Fe_2O_3/sepiolite
FSi	Fe_2O_3/SiO_2
FTi	Fe_2O_3/TiO_2
FYSZ	Fe_2O_3/YSZ
FZr	Fe_2O_3/ZrO_2
FZrCa	Fe_2O_3/Ca-ZrO_2
FZrCe	Fe_2O_3/Ce-ZrO_2
FZrMg	Fe_2O_3/Mg-ZrO_2
M	manganese oxide, Mn_3O_4
MA	Mn_3O_4/Al_2O_3
MAMg	$Mn_3O_4/MgAl_2O_4$
MAMn	$Mn_3O_4/MnAl_2O_4$
MSe	Mn_3O_4/sepiolite
MSi	Mn_3O_4/SiO_2
MTi	Mn_3O_4/TiO_2
MZr	Mn_3O_4/ZrO_2
MZrCa	Mn_3O_4/Ca-ZrO_2
MZrCe	Mn_3O_4/Ce-ZrO_2
MZrMg	Mn_3O_4/Mg-ZrO_2
N	nickel oxide, NiO
NA	NiO/Al_2O_3
NAN	$NiO/NiAl_2O_4$
NANBe	$NiO/NiAl_2O_4$ with bentonite
NBe	NiO/bentonite
NBHA	NiO/barium-hexaaluminate
NCoYSZ	NiO/CoO-YSZ
NMg	NiO/MgO
NSe	NiO/sepiolite
NSi	NiO/SiO_2
NTi	NiO/TiO_2
NZr	NiO/ZrO_2
NYSZ	NiO/YSZ
YSZ	yttria-stabilized zirconia

Appendix B

Summary of chemical-looping prototypes

Ref	Type	Period (h)	Power (kW)	Fuel	OC	Prepare	Loss rate (wt%/h)	Lifetime (h)
[90]	I	107	10	Natural gas	Ni, Fe	-	0.0023	40000
[154]	I	100	10	CH_4	$NiO/NiAl_2O_4$	FG	-	-
[176]	I	160	10	Natural gas	$NiO/NiAl_2O_4$	spin-flash	0.022	4500
[205]	I	1016	10	Natural gas	$NiO/(Ni,Mg)Al_2O_4$	SD	0.003	33000
[95]	II	200	10	CH_4	CuO/Al_2O_3	DI	0.04	2400
[164]	II	100	10	CH_4	CuO/Al_2O_3	DI	0.04	2400
[189]	II	40	0.5	CH_4, C_2H_6, C_3H_8	NiO/Al_2O_3	DI	-	-
[91]	II	100	0.5-0.85	CH_4	$NiO/NiAl_2O_4$	DI	0.01	10000
[192]	II [e]	50	0.9	CH_4	NiO/Al_2O_3	DI	-	-
[193]	II	50	-	CO,H_2	NiO/Al_2O_3	DI	-	-
[194]	II	40	0.5	syngas	CuO/Al_2O_3	DI	0.02	5000
[195]	II	35	0.5	CH_4	NiO/Al_2O_3	DI	-	-
[224]	II	22	0.5-0.78	CH_4	CuO/Al_2O_3	DI	-	-
[225]	II	30	0.5	CH_4, C_2H_6, C_3H_8	CuO/Al_2O_3	DI	-	-
[76]	II [e]	121	0.5	PSA off gas	Fe_2O_3 [d]	-	-	-
[40]	III	130	0.1-0.3	Natural gas /syngas	$Mn_3O_4/Mg\text{-}ZrO_2$	FG	0.038	2600
[93]	III	<10	0.3	Natural gas	$NiO/MgAl_2O_4$	FG	0.027	3700
[33]	III	150	0.3	Natural gas	$NiO/MgAl_2O_4$	FG	0.027	3700
[157]	III [e]	41	-	Natural gas	$NiO/MgAl_2O_4$	FG	-	-
[161]	III	60	0.1-0.3	Natural gas /syngas	Fe_2O_3/Al_2O_3	FG	No detected	-
[178]	III [e]	160	-	Natural gas	NiO/Al_2O_3,$MgAl_2O_4$	FG, DI	-	-
[209]	III	40	-	Natural gas	$NiO/Mg\text{-}ZrO_2$	FG	-	-
[92]	III	84	0.3	Natural gas	$NiO/(Ni,Mg)Al_2O_4$	SD	-	-
[241]	III	83	-	Natural gas	Ilmenite, NiO	-	-	-
[256]	III	70	-	Natural gas	$CaMn_{0.875}Ti_{0.125}O_3$	spray pyrolysis	-	-
[261]	IV	-	120	Natural gas	$NiO/NiAl_2O_4$	FG	-	-
[201]	IV	-	140	Natural gas	$NiO/NiAl_2O_4$, $NiMg_2O_4$	-	-	-
[97]	IV	-	120	Natural gas,C_3H_8	$NiO/NiAl_2O_4$, $NiMg_2O_4$	SD	-	-
[60]	IV	-	65-145	Natural gas /syngas	Ilmenite, NiO	-	-	-
[240]	IV [e]	<20	140	Natural gas	$NiO/(Ni,Mg)Al_2O_4$	SD	-	-
[61]	V	22	10	Coal[a]	ilmenite	-	-	-
[62]	V	11	10	Coke[c]	ilmenite	-	0.01-0.03	3000-9500
[63]	V	26	10	Coke[c]	ilmenite	-	-	-
[64]	V	100	10	Coke[c]&coal[a]	ilmenite	-	-	-
[233]	V	-	10	Coke[c]&coal[a]	ilmenite	-	-	-
[98]	VI	100	10	Coal[b]	NiO/Al_2O_3	CP	-	-
[210]	VI	30	-	Coal[b]	NiO/Al_2O_3	I	-	-
[211]	VI	30	10	biomass(sawdust)	Fe_2O_3	MM	-	-
[82]	VI	30	1	Coal [b]	NiO/Al_2O_3	CP	-	-
[242]	VI	-	1	CO, H_2	NiO/Al_2O_3	CP	-	-
[250]	VI	-	1	Coal [b] and sawdust	Iron ore	-	-	-

[a] South African coal [b] Shenhua bituminous coal [c] petroleum coke [d] iron waster from aluminum production [e] chemical-looping reforming

Appendix C

Process and cyclic analysis of CLC for power generation

Reference	Cycle	Fuel	OC	η_{th} (%)	η_{CO2} (%)	Findings and Conclusions
Ishida et al [15]	Humid-air cycle[1)]	CH_4	F	50.2	100	Saturation of methane with water recovers low-level thermal energy by evaporating steam in saturator by exhaust gas. 90% water can be condensed because gas is not diluted with air.
Ishida and Jin [16]	Humid-air cycle	CH_4	N	55.1	100	Air is saturated with steam. Multistage intercooling is used to reduce the compression work thus higher efficiency than [15]. No corrosion in the air flue gas exists due to no impurities from the fuel.
Anheden and Svedberg [107]	Brayton, CC	CH_4, syngas	N, F	44.2[2)]	100	Exhaust from AR is used to heat FR. Detailed exergy analysis demonstrates that the destruction of fuel exergy upon combustion is decreased compared to conventional combustion.
Jin and Ishida [110]	Humid-air cycle	H_2	N	63.5	100	Ideal calculation without consideration of pressure loss, heat loss, solid particle transport and heat transfer gives the estimation of the maximum efficiency (63.5%) that can be achieved with the T_{ox} of 1200°C.
Brandvoll and Bolland [111]	Humid-air cycle	CH_4	NYSZ	55.9	100	T_{ox} has the most significant impact on the overall efficiency. If work of CO_2 compression to 100 bar is included, 54% efficiency is obtained.
Naqvi et al [102]	CC	NG	NAN	49.7[3)]	100	A CLC Rankine cycle is also evaluated with efficiency of 40.1% and T_{ox} of 850°C.
Hong and Jin [114]	Solar hybrid CC	Solar, CH_4	N	57.5	100	Ideal calculation without consideration of pressure loss. Solar energy is used to heat reduction. The solar thermal energy input is 10% of total. The solar-hybrid design takes advantages of the essential characteristics of CLC, upgrading low level energy from reduction towards high level energy from oxidation.
Wolf et al [104]	CC	CH_4	F FA NAN	52.6[3)]	100	The efficiency penalty of fan power is less than 1.5% such that the performances of Ni-based, and Fe-based OCs are similar. The T_{ox} is critical and if less than 1000, CLC is not competitive with post-combustion capture.
Consonni et al [105]	CC	NG	F / inert	47.9[3)]	100	A lower efficiency than [293] with similar design is due to lower T_{ox}(1050°C) compared to 1200°C in [293]. Supplementary firing increases efficiency to 52% but only 50% η_{CO2}. High T_{ox} is critical to the competitivity of CLC.
Hong et al [115]	Solar hybrid CC	Solar, CH_4	N	57.0[2)]	100	Similar design but more realistic calculation as in [203]. The solar thermal energy input is 18.6% of total.
Kvamsdal et al [6]	CC	NG	N	51.3[3)]	100	Based on [102]. CLC offers the second highest efficiency with 100% CO_2 capture (Figure 1-2).
Naqvi et al [103]	CC	NG	NAN	52.2[3)]	100	Part-load analysis by altering the air, or fuel flowrate shows the efficiency drops by 2.6% when reducing the load down to 60%. This off-design efficiency is better than conventional combined cycle.
Naqvi et al [106]	Multistage CC	NG	NAN	53.5[3)]	100	Single-stage reheating enhances the efficiency by 1% compared with CLC CC of 51.9%. Double-stage reheating only increases the efficiency by 0.1% from single stage reheat.
Xiang and Wang [262]	CC	Coal	NAN	44.4[3)]	90	Supplemental firing. Pipe-type coal gasifier is inside CLC AR and takes heat from AR. T_{AR} is key parameter; higher value leads to increase of system efficiency and decrease of CO_2 efficiency.
Jin et al [109]	Intercooled CC	Methanol	F	59.5	70	Supplemental firing. Heat from intercooling, exhaust gas is recovered by evaporation and reforming fuel, and preheating air, respectively. The efficiency increases with TIT, and first increases then decreases with PR.
Rezvani et al [263]	IGCC	Bituminous coal	NA	34.5[3)]	100	Single CLC using gasified syngas has a lower efficiency than IGCC with CO_2 capture. Two stage reheat CLC has better efficiency but cost is higher.
Zhang et al [112]	Intercooled CC	Methanol	F	56.8	100	Heat from intercooling is used to preheat fuel. Similar conclusion is obtained as in [109]
Hong et al [113]	Solar hybrid CC	Solar, methanol	F	58.9	55	Supplemental firing decomposed syngas. Solar energy is used to drive endothermic methanol reduction at 150°C. The total efficiency and solar-to-electric efficiency are enhanced using CLC.
Cormos [264]	IGCC	Coal	F	38.9[3)]	99.5	Higher efficiency than post-, pre-combustion capture.
Kobayashi and Fan [265]	BDCL	Biomass	F	38.1	99	Biomass has low energy density, high moisture content, highly distributed-resource and thus less efficient and more cost intensive. Small scale power generation for biomass is less efficient and hydrogen production appears to be an alternative option. CLC offers higher efficiency and lower cost than IGCC w/ CCS for biomass.

1) fuel is saturated with steam rather than air 2) calculated from exergetic efficiency 3) the CO_2 compression work is included.

Appendix D

The oxygen carrier conversion rate described by the unreacted shrinking-core model (USCM) is controlled by three resistances, as shown in Figure D-1 [128]: (i) external diffusion resistance through the gas film, (ii) internal diffusion through the porous layer or (iii) the chemical reaction kinetics. As the oxygen carrier reacts with the fuel (or oxygen), a layer of the fully reduced (or fully oxidized) solid product is formed around an unreacted core inside the particle, although the radius of the oxygen carrier particle remains almost constant during the redox reactions. The thickness of the product layer increases with time, producing a shrinking core of unreacted solid. Within the core of solid reactant, the solid phase concentration remains unchanged from its initial value. Thus, there is a sharp interface between the layer of solid product and the unreacted core. Figure D-1 shows the schematic drawing of shrinking-core model. Note that the unreacted shrinking-core model is different from the shrinking-core model, which also accounts for the particle size shrinking as occurs in the coal oxidation.

For the solid-gas reaction in Eq. (2.9), the unreacted shrinking-core model for spherical particles models the change of the unreacted core r_c as:

$$-\frac{dr_c}{dt} = \frac{vC_A / \rho_{B.m}}{\frac{r_c^2}{R^2 h_m} + \frac{(R-r_c)r_c}{RD_a} + \frac{1}{kC_A^{n-1}}} \tag{D.1}$$

where v is the stoichiometric coefficient, R is the radius (m) of particle, D_a is the effective diffusivity (m^2/s) of gas A through the ash layer. h_m represents the gas film mass transfer coefficient (m/s). k represents reaction constant in Eq. (2.11), and $\rho_{B,m}$ represents the mole density (mol/m^3) of solid.

The three terms in the denominator of Eq. (D.1) represent the resistance by the external diffusion, the internal diffusion, and the chemical reaction, respectively. Table D-1 summarizes the solutions of Eq. (D.1) with respect to each of these three resistances. Two cases are included, i.e. a flat plate and a sphere [128]. For the flat plate case, the active metal oxide is converted in the direction perpendicular to the surface of the plate. The USCM for the flat plate geometry is used in ref. [125] since the active metal oxide in each grain within spherical particles is exposed to the same ambient gas concentrations and hence it reacts in the same way as that in the flat plate unreacted shrinking-core model.

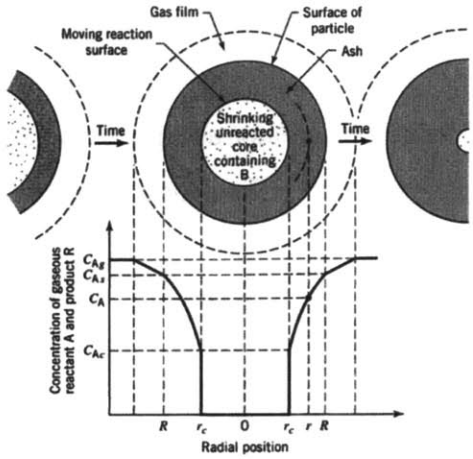

Figure D-1 A schematic drawing of shrinking-core model. [128]

The conversion time τ in Table D-1 describes the time needed for conversion under each resistance. A longer conversion time (τ) means a higher mass transfer resistance. The sum of τ's is the time needed for conversion under all three resistances [128]. Thus in order to apply the mechanism in ref. [125] to the rotary reactor design, it is necessary to assure that the internal mass transfer resistances for the spherical particle and the flat plate layer are comparable, both of which are small compared to the chemical reaction.

By matching the conversion times for internal diffusion between the flat plate (Eq. (D.3)) and the sphere (Eq. (D.4)), we can obtain the same results as in Section 4.3.3:

$$\delta_{oc} \sim \frac{d_p}{2\sqrt{3}} \tag{D.2}$$

Table D.1 Conversion-time expressions for flat plate and sphere shape unreacted shrinking-core model [128]

	External diffusion	**Internal diffusion**	**Reaction controls**
Flat plate $X = 1 - \frac{z_c}{L}$ L=half thickness	$\frac{t}{\tau} = X_B$ $\tau = \frac{\rho_{B,m} L}{v k_g C_A}$	$\frac{t}{\tau} = X_B^2$ $\tau = \frac{\rho_{B,m} L^2}{2 v D_a C_A}$ (D.3)	$\frac{t}{\tau} = X_B$ $\tau = \frac{\rho_{B,m} L}{v k C_A}$
Sphere $X_B = 1 - \left(\frac{r_c}{R}\right)^3$	$\frac{t}{\tau} = X_B$ $\tau = \frac{\rho_{B,m} R}{3 v k_g C_A}$	$\frac{t}{\tau} = 1 - 3(1 - X_B)^{2/3} + 2(1 - X_B)$ $\tau = \frac{\rho_{B,m} R^2}{6 v D_a C_A}$ (D.4)	$\frac{t}{\tau} = 1 - (1 - X_B)^{1/3}$ $\tau = \frac{\rho_{B,m} R}{v k C_A}$

Note that for flat plate, the unreacted shrinking-core model describes the plate with both surfaces being exposed to gas. Thus, from symmetry, half of the plate should be the same with the porous OC layer case in the current design, i.e., $L=\delta_{oc}$.

Appendix E

1. Nonreactive flow

Cold air enters the channel and leaves the reactor at high temperature. The solid phase is already fully oxidized and it is maintained at 1073K. Thus for a steady flow, Eqs. (4.6) and (4.7) can be simplified into:

$$u_b C_b = u_{b,0} C_{b,0} \tag{E.1}$$

$$u_b C_b c_{p,b} \frac{\partial T_g}{\partial z} = \frac{P_c}{A_p} h_{gs} \left(T_{s,0} - T_g \right) \tag{E.2}$$

where $u_{b,0}$ is the inlet velocity and $C_{b,0}$ is the inlet gas concentration. $T_{s,0}$ is the constant solid temperature. $c_{p,b}$ is specific heat capacity and it is assumed to be constant with temperature. Therefore,

$$\frac{T_{s,0} - T_g}{T_{s,0} - T_{g,0}} = \exp\left(-\frac{P_c h_{gs} z}{A_p c_{p,b} C_{b,0} u_{b,0}} \right) \tag{E.3}$$

2. Isothermal oxidation flow

Both solid and gas phase are kept at 1073K. The oxygen carrier on the surface is fully reduced. Therefore, based on the kinetics (Eq. (4.12)), the flow is expected to be steady until oxygen carrier is fully oxidized. Since the temperature is constant, the bulk concentration (C_b) is constant. Thus, the species transport equations for O_2 and N_2 are simplified into:

$$\frac{\partial \left[u_b \left(1 - X_{O_2} \right) \right]}{\partial z} = 0 \tag{E.4}$$

$$\frac{\partial \left(u_b X_{O_2} \right)}{\partial z} = -\frac{P_c}{A_p} \frac{h_{m,O_2} \varepsilon_{Cu} k_{Cu} \delta_{oc}}{h_{m,O_2} + \varepsilon_{Cu} k_{Cu} \delta_{oc}} X_{O_2} \tag{E.5}$$

where X_{O2}, $h_{m,O2}$ are the molar fraction and the mass transfer coefficient of O_2. ε_{Cu} and k_{Cu} are the volume fraction and the Arrhenius reaction rate constant for copper oxidation. Substitute Eq. (E.4) into Eq. (E.5),

$$\frac{1}{1 - X_{O_2}} + \ln\left(\frac{X_{O_2}}{1 - X_{O_2}} \right) - \frac{1}{1 - X_{O_2,0}} - \ln\left(\frac{X_{O_2,0}}{1 - X_{O_2,0}} \right) = -\frac{P_c h_{m,O_2} \varepsilon_{Cu} \delta_{oc} k_{Cu} z}{A_p \left[u_{b,0} \left(1 - X_{O_2,0} \right) \right] \left(h_{m,O_2} + \varepsilon_{Cu} \delta_{oc} k_{Cu} \right)} \tag{E.6}$$

where $X_{O2,0}$ is the molar fraction of O_2 at the channel inlet.

Appendix F

For an open flow system interacting only with the environment at T_o (298K), the first law and the second law of thermodynamics state that (neglecting kinetic and potential energy):

$$\frac{dE}{dt} = \dot{Q} - \dot{W} + \sum_{in} \dot{m}_i h_i - \sum_{out} m_i h_i \tag{F.1}$$

$$\frac{dS}{dt} = \frac{\dot{Q}}{T_o} + \sum_{in} \dot{m}_i s_i - \sum_{out} \dot{m}_i s_i + \dot{S}_g \tag{F.2}$$

where E and S are the total internal energy and total entropy of the system. $\dot{Q}$ and $\dot{W}$ are the heat transfer and work transfer with the environment. $\dot{m}_i$, h_i, and s_i are the mass flow rate, specific enthalpy and entropy of stream i. $\dot{S}_g$ is the entropy generation. Substitute Eq. (F.2) into Eq. (F.1) and integrate in one cycle, we can obtain:

$$\dot{W} = \sum_{in} \dot{m}_i (h_i - T_o s_i) - \sum_{out} \dot{m}_i (h_i - T_o s_i) - T_o \dot{S}_g \tag{F.3}$$

Therefore in the cyclic the maximum work transfer rate is obtained when the process is reversible, i.e. $\dot{S}_g = 0$. The term $(h_i - T_o s_i)$ is called the flow exergy function and it is denoted as ξ_i.

For $\dot{W}_{\max,in}$, inlet streams are the fuel, the air and the steam. The outlet stream is the product from complete combustion of all feed streams at the ambient temperature (Figure F-1(a)):

$$\dot{W}_{\max,in} = \dot{m}_{fuel}\xi_{fuel} + \dot{m}_{air}\xi_{air} + \dot{m}_{steam}\xi_{steam} - \dot{m}_{ambient}\xi_{ambient} \tag{F.4}$$

For $\dot{W}_{\max,out}$, the inlet streams are the two flue streams from fuel and air zones. The outlet stream is the mixture of these streams at the ambient temperature (Figure F-1(b)). Note that the unburned CH_4 from the fuel zone also exists in the ambient stream.

$$\dot{W}_{\max,out} = \dot{m}_{fuel\,zone}\xi_{fuel\,zone} + \dot{m}_{air\,zone}\xi_{air\,zone} - \dot{m}_{ambient}\xi_{ambient} \tag{F.4}$$

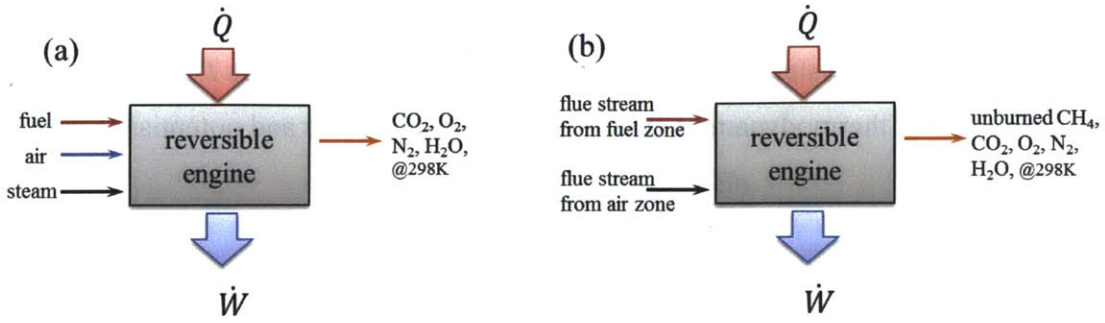

Figure F-1 Illustration of the maximum work transfer from (a) the inlet streams and (b) the outlet streams

For direct combustion, the maximum work from the flue stream is calculated according to Figure F-2. The inlet stream temperature is obtained from constant pressure adiabatic combustion assuming complete fuel conversion. The maximum work is calculated as:

$$\dot{W}_{\max,steam} = \dot{m}_{flue}\xi_{flue} - \dot{m}_{ambient}\xi_{ambient} \tag{F.5}$$

$$\dot{W}_{\max,no\ steam} = \dot{m}_{flue}\xi_{flue} + \dot{m}_{steam}\xi_{steam} - \dot{m}_{ambient}\xi_{ambient} \tag{F.6}$$

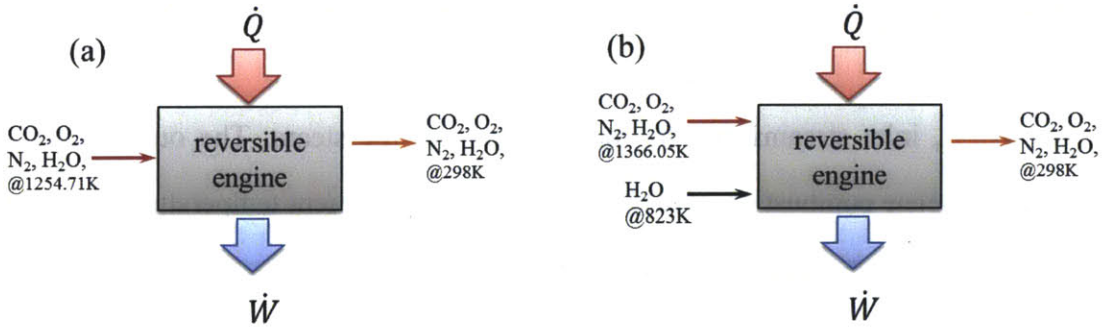

Figure F-2 Illustration of the maximum work transfer in direct combustion (a) with and (b) without steam mixing

The second law efficiency can be calculated as:

$$\eta_{II} = \frac{\dot{W}_{\max,out}}{\dot{W}_{\max,in}} \qquad \text{for rotary design} \tag{F.7}$$

$$\eta_{II} = \frac{\dot{W}_{\max,steam}}{\dot{W}_{\max,in}} \qquad \text{for direct combustion with steam} \tag{F.8}$$

$$\eta_{II} = \frac{\dot{W}_{\max,no\ steam}}{\dot{W}_{\max,in}} \qquad \text{for direct combustion without steam} \tag{F.9}$$